Università degli Studi di Padova

University of Padova
Department of Information Engineering

Ph.D. School in Information Engineering
Information Science and Technology
XXVI series

Ph.D. Thesis

Analysis and application of nonlinear amplification effects in single-mode optical fibers

Fabrizio Chiarello

School Director
Chiar.mo Prof. Matteo Bertocco

Supervisor
Dott. Luca Palmieri

Course Coordinator
Prof. Carlo Ferrari

January 2014

To anyone who can see the world
through the eyes of a child.

Acknowledgements

This thesis is the summary of three years of study, research and work spent toward the degree of Philosophiæ Doctor.

It's not an easy task to look backward over these three years to try to enumerate all the people that have contributed, directly or indirectly, to advance me toward the target. Even more difficult is to give them all an appropriate space on this page. I can only do the my best.

First of all, I would like to thank my supervisor *Dr. Luca Palmieri*, to whom I am deeply grateful for his invaluable support, guidance, and mentoring during these three years. He patiently lead me to think coherently and scientifically, spurring me to improve my experimental and theoretical skills. I thank *Prof. Marco Santagiustina* who also definitely dispensed me invaluable advice on topics unknown to me. I wish also to thank the other, current and past, members of the ''Photonics and Electromagnetics Group'', starting with the head *Prof. Andrea Galtarossa*, for providing me the opportunity to join and to stay in the group. With equal weights and measures, and in all the permutations, I thank the set {*Dr. Luca Schenato*, *Dr. Leonora Ursini*, *Dr. Elena Autizi*} for the competence, discussions, suggestions, patience and friendship; and a special mention goes to *Dr. Sourabh Roy* for helpful discussions.

I'm very grateful to *Prof. Magnus Karlsson* for hosting me for six beautiful months at the ''Photonics Laboratory'' of the Department of Microtecnology and Nanoscience of the Chalmers University of Technology in Göteborg (Sweden). I would like to thank the head of the group, Prof. Peter Andrekson, and all the members, in particular Dr. Aleš Kumpera, Clemens Krückel and Abel Lorences Riesgo.

I thank Davide Zordan, Marco Mezzavilla, Dr. Paolo Baracca, Daniele Munaretto and Matteo Canale for invaluable technical and playful discussions.

Thanks to Simone Piccirilli, Dr. Roberto Corvaja, Dr. Alberto Ferrario, Dr. Daniele Fontanari and Dr. Silvia Mittenpergher for making my living in Padova more enjoyable.

I thank my parents for their support.

Finally, I would like to dedicate this thesis to Valentina, for her ''*nonlinear and stochastic*'' patience during these last months, and to Emma, Enea and Isaac for definitely seeing the world through the eyes of a child.

Padova, Tuesday 28th January, 2014

Fabrizio

Abstract

This thesis focuses on all-optical signal generation and processing through nonlinear amplification phenomena in single-mode fibers.

Three different nonlinear fiber optical oscillators are investigated and experimentally demonstrated. A continuous-wave pump for fiber Raman amplifiers, developed with the goal of achieving high degree of polarization, tunability and suppression of stimulated Brillouin scattering, is presented, discussed and used to achieve nonlinear polarization attraction. A fast and widely tunable fiber optical oscillator based on stimulated Raman scattering and on broad- and narrow-band fiber optical parametric amplification, and exploiting the time-dispersion-tuning technique, is demonstrated and characterized. Each nonlinear effect dominates in a different spectral region, so that the fiber optical oscillator achieves a tuning range of 160 nm. Through the same time-dispersion-tuning method, a fast tunable optical frequency comb, based on cascaded four-wave mixing, is obtained by using a single pump, avoiding the limitations in spectral purity and frequency and phase stability given by double pump systems.

Finally, the control of the state of polarization and of the degree of polarization through nonlinear polarization attraction in counter-propagating fiber Raman amplifiers in standard, randomly birefringent, single-mode fibers is studied, analyzed and characterized. The analysis, including the effects of pump depletion, nonlinear polarization rotation and orthogonal Raman gain, shows that counter-propagating fiber Raman amplifiers are effective in attracting the signal toward a predetermined state of polarization settled by the pump input state of polarization. Moreover, the importance of the role of pump depletion in achieving signal repolarization in fibers with moderately-high polarization-mode dispersion is discussed. The performances and the limits of repolarization efficiency are determined, leading to a quantitative relationship between the degree of polarization and the gain of the fiber Raman amplifier, which is then confirmed to represent an upper bound on the maximum achievable degree of polarization.

Sommario

Questa tesi è focalizzata sulla generazione e sull'elaborazione completamente ottiche di segnali attraverso fenomeni di amplificazione non lineare in fibre ottiche a singolo modo.

Tre diversi oscillatori non lineari in fibra ottica sono investigati e dimostrati sperimentalmente. Una pompa ad onda continua per amplificatori Raman in fibra, sviluppata con l'obiettivo di ottenere un alto grado di polarizzazione, sintonizzabilità e soppressione dell'effetto Brillouin, è presentata, discussa e utilizzata al fine di ottenere attrazione di polarizzazione non lineare. Un oscillatore in fibra ottica con sintonia veloce su un'ampia banda basato sugli effetti di amplificazione Raman e di amplificazione parametrica a banda stretta e a banda larga, che sfrutta la tecnica di sintonia mediante dispersione temporale (*time-dispersion tuning*), è dimostrato e caratterizzato. Ciascuno degli effetti non lineari domina in una diversa regione spettrale, cosicché l'oscillatore raggiunge un intervallo di sintonia di 160 nm. Attraverso lo stesso metodo di sintonia mediante dispersione temporale, un *comb* ottico in fibra con sintonia veloce, basato sull'effetto di miscelazione a quattro onde a cascata, è ottenuto usando una singola pompa, evitando così i limiti di purezza spettrale e di stabilità di frequenza e di fase dei sistemi a doppia pompa.

Infine, il controllo dello stato e del grado di polarizzazione, attraverso l'attrazione di polarizzazione non lineare in amplificatori Raman in fibra ottica standard con birifrangenza aleatoria, è studiato, analizzato e caratterizzato. L'analisi, che include gli effetti di svuotamento della pompa, della rotazione non lineare di polarizzazione e di guadagno Raman ortogonale, mostra che gli amplificatori Raman contro-propaganti sono efficaci nell'attrarre il segnale verso uno stato di polarizzazione predeterminato e imposto dallo stato di polarizzazione di ingresso della pompa. Viene inoltre discussa l'importanza del ruolo dello svuotamento della pompa nell'ottenere la ripolarizzazione del segnale in fibre con dispersione dei modi di polarizzazione moderatamente alta. Le prestazioni e i limiti dell'efficienza di ripolarizzazione vengono determinati portando ad una relazione quantitativa tra il grado di polarizzazione e il guadagno dell'amplificatore Raman, relazione che rappresenta un limite superiore sul massimo grado di polarizzazione raggiungibile.

Contents

List of Figures

List of Acronyms

ASE	amplified spontaneous emission.
BBFOPA	broad-band fiber optical parametric amplification.
BPF	band pass filter.
BVP	boundary value problem.
CFWM	cascaded four-wave mixing.
CW	continuous-wave.
DCF	dispersion-compensating fiber.
DGD	differential group delay.
DOP	degree of polarization.
DSF	dispersion-shifted fiber.
DWDM	dense wavelength-division-multiplexing.
ECL	external cavity laser.
EDF	erbium-doped fiber.
EDFA	erbium-doped fiber amplifier.
EOM	electro-optic modulator.
EPG	electrical pulse generator.
FOPA	fiber optical parametric amplification.
FOPO	fiber optical parametric oscillator.
FPC	fiber polarization controller.
FRA	fiber Raman amplifier.
FSR	free spectral range.
FUT	fiber under test.
FWM	four-wave mixing.
GVD	group velocity dispersion.
HNLF	highly nonlinear fiber.
IVP	initial value problem.

LP	linear polarizer.
NBFOPA	narrow-band fiber optical parametric amplification.
NPA	nonlinear polarization attraction.
NPR	nonlinear polarization rotation.
NZDSF	non-zero dispersion-shifted fiber.
OCi	optical circulator.
OCo	optical coupler.
ODE	ordinary differential equation.
OFC	optical frequency comb.
OFDM	orthogonal frequency division multiplexing.
OI	optical isolator.
OSA	optical spectrum analyzer.
PDG	polarization-dependent gain.
PDL	polarization-dependent loss.
PMD	polarization-mode dispersion.
PMDc	PMD coefficient.
PRBS	pseudo-random binary sequence.
PS-FOPA	phase-sensitive fiber optical parametric amplification.
QWP	quarter-wave plate.
RIN	relative intensity noise.
RK	Runge-Kutta.
RK4	fourth-order Runge-Kutta.
RMM	random modulus model.
RMS	root mean square.
RP	Raman polarizer.
SBS	stimulated Brillouin scattering.
SMF	single-mode fiber.
SOP	state of polarization.
SPM	self-phase modulation.
SRS	stimulated Raman scattering.
TDF	thulium-doped fiber.
TDT	time-dispersion-tuning.
VOA	variable optical attenuator.
WDM	wavelength-division-multiplexing.
XPM	cross-phase modulation.

ZDW zero-dispersion wavelength.

Chapter 1

Introduction

$$a^2 + b^2 = c^2$$

Pythagoras
6th century BCE – 5th century BCE

Since their advent[1] in the 70s, optical fibers have been progressively introduced in our daily life becoming one of the most significant achievement of the modern era. Optical fibers constitute the backbone of the world communication infrastructure, and their ability to efficiently guide light have spurred their use also in different fields such as medical sciences, industry and structural health monitoring. Moreover, in recent years considerable research efforts have been focusing on the nonlinear interactions between optical fields propagating in optical fibers. Spawned by the third-order susceptibility, commonly known as the $\chi^{(3)}$-nonlinearity, the nonlinear effects give rise to elastic, such as four-wave mixing (FWM) and fiber optical parametric amplification (FOPA), and inelastic scattering phenomena, such as stimulated Brillouin scattering (SBS) and stimulated Raman scattering (SRS). The energy exchange between different signals mediated by the $\chi^{(3)}$-nonlinearity is apt to be used as a nonlinear amplification mechanism, and its time scale on the order of the femtosecond enables the development of new classes of all-optical devices for virtually instantaneous signal generation and processing.

This thesis focuses on all-optical signal generation and processing through nonlinear amplification phenomena in single-mode fibers (SMFs), and is divided into two major topics. The first part of the thesis is devoted to nonlinear fiber optical oscillators, and three different optical sources are discussed and experimentally demonstrated: a continuous-wave (CW), highly polarized, tunable pump for application in fiber Raman amplifiers (FRAs); a widely tunable fiber optical oscillator based on SRS and FOPA; and a fast tunable optical frequency comb (OFC) realized exploiting cascaded four-wave mixing (CFWM). The second part is dedicated to nonlinear polarization attraction (NPA) in counter-propagating FRAs for the control of the state of polarization (SOP) of signals: purely Raman-based nonlinear repolarization is studied and experimentally demonstrated, and the limits of repolarization efficiency are determined.

[1]The research in optical fibers started in 1966 with the study of the loss mechanisms of glasses by Kao and Hockham [1], and with the realization of low-loss optical fibers in the following years [2], [3]. The work of Charles K. Kao was worth of the Nobel Prize, awarded in 2009.

1.1 Nonlinear fiber optical oscillators

The first part of the thesis is devoted to all-fiber lasers, which, over the past two decades, have been the subject of a considerable amount of research owing to the several potential advantages they present with respect to bulk lasers, among which the following main ones are worth being mentioned:

- the lack of critical components such as mirrors, crystals or prisms, which makes them very attractive due to the low complexity and high ruggedness;
- the fiber-based gain media, which enable inherently single-mode operations, high coupling efficiency and superior beam quality especially for high average powers;
- the unavailability of good bulk crystals or glasses for unusual spectral regions, particularly the near infrared, where lasing can be efficiently achieved with fiber-based systems;
- the achievable high-speed and broad-range of tuning, permitted by the larger bandwidth of fibers.

Fiber-lasers are conveniently used in industry and in medical sciences, where high power and high beam quality is demanded, *e.g.* for micro-welding and micro-cutting. On the other hand, in applications like optical coherence tomography [4], spectroscopy, distributed remote sensing [5], and dense wavelength-division-multiplexing [6], characteristics as high-speed and wide-range wavelength tuning are mandatory requirements. If conventional lasers have fundamental limitations on the range and speed of tuning due to the presence of mechanically controlled optical filters and gratings, all-fiber lasers can overcome such limitations.

Furthermore, OFCs represent another key application in communication [7], signal processing [8], metrology [9], [10] and spectroscopy [10], [11] that has been gathering conspicuous attentions. Some of the limits of conventional OFC generators, such as the fixed frequency spacing of monolithic cavities or the slowness in tuning realized through thermal effects [12] or mechanical stages [13], can be overcome in optical fibers, for instance through CFWM, achieving better and faster OFCs tunability. However, OFCs realized in CFWM resonators are generally achieved via double pump systems [14], [15], with limitations in spectral purity and frequency and phase stability [16] that need to be addressed.

1.2 Nonlinear polarization attraction in fiber Raman amplifiers

The second part of the thesis investigates nonlinear polarization attraction (NPA) in counter-propagating FRAs for the control of the SOP.

Polarization is an important degree of freedom of light which is being increasingly exploited in the fields of optical communications and sensing systems, among others. Over the past few years, all-optical processing of polarization has been the subject of considerable research efforts, giving rise to new devices able, for example, to perform polarization

modulation and regeneration, or to control the SOP and the degree of polarization (DOP). For instance, controlling the DOP permits to attain signal depolarization or repolarization.

Signal repolarization can be obtained by using classical bulk polarizers, which operate by projecting the SOPs over a predetermined direction. However, such projection process poses physical limitations on the achievable efficiency. Over the past few years, NPA has been proposed as an effective all-optical method to control the SOP. Fundamentally, NPA is a process in which the SOP is attracted, rather than projected, to a predetermined direction, therefore increasing the limits on the efficiency.

The first all-optical repolarizer, demonstrated in 2000 by Heebner *et al.* [17] and which was based on the photo-refractive effect, had severe limitations due to the low response time of the mediating material. Only recently, nonlinear amplification processes in SMFs have been successfully exploited to obtain NPA[P.2], [18]–[45], [C.2], [P.3]. Such processes have response time in the order of femtoseconds, enabling virtually instantaneous control of the SOP.

Among the others, the nonlinear Raman amplification process has been very recently demonstrated as an effective method to obtain both amplification and NPA in standard telecommunications SMFs [P.2], [18]–[30], [C.2], [P.3]. One of the main advantages of the SRS process is certainly its amplification band of more than 7 THz [25], together with the possibility of shifting such wide spectral region by only controlling the wavelength of the pump [46], enabling therefore the use of NPA in unconventional bands. Another major benefit of SRS is the possibility of being used in existing links.

If on one hand, it has been very recently demonstrated the possibility to apply Raman-based NPA to realize signal repolarization in integrated silicon devices and in wavelength-division-multiplexing systems, or to enhance the performances of FRAs, on the other hand the performances and the limits of SRS-based NPA have not been yet fully acquainted and need to be addressed.

1.3 Outline of the thesis

This thesis is structured as follows.

Chapter 2 provides a brief overview about the origin of nonlinear phenomena in optical fibers. The focus is given to the amplification properties of FOPA and of SRS, whose scalar theories are concisely discussed.

Chapter 3 presents the topic of all-fiber optical sources through nonlinear amplification processes, and three different optical sources are demonstrated and discussed. The first source is a highly polarized and tunable CW pump for application in FRAs, aimed at preventing SBS depletion. Then, a widely tunable fiber optical oscillator based on FOPA and stimulated Raman scattering is described and characterized. The tuning, enabled through the time-dispersion-tuning (TDT) technique, spans a range of 160 nm and has an estimated sweep speed of 0.4 nm μs^{-1}. Finally, through the same technique a fast tunable optical frequency comb is realized exploiting cascaded four-wave mixing in the broad-band fiber optical parametric amplification regime.

In Chapter 4 the topic of NPA in counter-propagating FRAs in standard, randomly birefringent, SMFs is presented. After a short review of a vector model for SRS, a full-scale numerical analysis and statistical evaluations of NPA in counter-propagating FRAs in randomly birefringent SMFs are presented. The analysis includes the effects of pump

depletion, nonlinear polarization rotation (NPR) and orthogonal Raman gain, and it shows that counter-propagating FRAs are effective in attracting the signal toward a predetermined SOP settled by the pump input SOP, and that pump depletion plays an important role in achieving signal repolarization in fibers with moderately-high polarization-mode dispersion (PMD). Remarkably, it is predicted the existence of a quantitative relationship between the gain and the maximum DOP achieved by the signal in the amplifier. Finally, such relationship, which approximates both the performances and the limitations of the attraction efficiency, is experimentally validated, confirming that it represents an upper-bound on the maximum achievable DOP.

Finally, the closing chapter, Chapter 5, recapitulates the main findings of the thesis, and discusses potential applications and future research activities.

1.4 List of publications

The thesis is based on the following papers published in international peer-reviewed journals and conference proceedings:

[P.1] **F. Chiarello**, L. Palmieri, A. Galtarossa, and M. Santagiustina, "Widely time-dispersion-tuned fiber optical oscillator and frequency comb based on multiple nonlinear processes", *Optics Letters*, vol. 38, no. 22, pp. 4621–4624, Nov. 2013. DOI: 10.1364/OL.38.004621

[C.1] **F. Chiarello**, L. Palmieri, A. Galtarossa, and M. Santagiustina, "Nonlinear multi-process fiber laser widely tunable through time-dispersion tuning (invited)", in *Fotonica 2013, 15° Convegno Nazionale delle Tecnologie Fotoniche*, (May 21–23, 2013), Milano, Italy, 2013, p. C4.1

[P.2] **F. Chiarello**, L. Palmieri, M. Santagiustina, R. Gamatham, and A. Galtarossa, "Experimental characterization of the counter-propagating Raman polarization attraction", *Optics Express*, vol. 20, no. 23, pp. 26 050–26 055, Nov. 2012. DOI: 10.1364/OE.20.026050

[P.3] **F. Chiarello**, L. Ursini, L. Palmieri, and M. Santagiustina, "Polarization attraction in counterpropagating fiber Raman amplifiers", *Photonics Technology Letters*, vol. 23, no. 20, pp. 1457–1459, Oct. 15, 2011. DOI: 10.1109/LPT.2011.2163061

[C.2] **F. Chiarello**, L. Ursini, L. Palmieri, M. Santagiustina, A. W. R. Leitch, and M. Guglielmucci, "Polarization attraction in counter-propagating fiber Raman amplifiers", in *Fotonica 2011, 13° Convegno Nazionale delle Tecnologie Fotoniche*, (May 9–11, 2011), Genova, Italy, 2011, p. C4.3

The following are other publications which are out of the scope of this thesis.

[C.3] M. Santagiustina, L. Ursini, A. Galtarossa, **F. Chiarello**, L. Palmieri, C. G. Someda, L. Thévenaz, and A. Leitch, "Microwave photonic notch filter based on dynamic Brillouin gratings generated by PRBS signals", in *Fotonica 2012, 14° Convegno Nazionale delle Tecnologie Fotoniche*, (May 15–17, 2012), Firenze, Italy, 2012, B3.4

[C.4] L. Schenato, G. Marcato, A. Pasuto, L. Palmieri, **F. Chiarello**, A. Galtarossa, G. Gruca, T. van de Watering, and D. Iannuzzi, "Experimental analysis of fiber optic sensor for detection of precursory acoustic signals in rockfall events", in *Fotonica 2012, 14° Convegno Nazionale delle Tecnologie Fotoniche*, (May 15–17, 2012), Firenze, Italy, 2012, B6.5

[C.5] M. Santagiustina, L. Ursini, L. Palmieri, **F. Chiarello**, and M. Bosiljevac, "Dynamic Brillouin gratings permanently induced by chaotic signals for sensing applications", in *Fotonica 2011, 13° Convegno Nazionale delle Tecnologie Fotoniche*, (May 9–11, 2011), Genova, Italy, 2011, B6.6

[C.6] **F. Chiarello**, M. Santagiustina, and L. Ursini, "Securing free space optics communications through optical chaos", in *Access Networks and In-house Communications*, (Jun. 12–14, 2011), Toronto, Canada: OSA, 2011, ATuC5

[P.4] **F. Chiarello**, L. Ursini, and M. Santagiustina, "Securing wireless infrared communications through optical chaos", *Photonics Technology Letters*, vol. 23, no. 9, pp. 564–566, May 1, 2011. DOI: 10.1109/LPT.2011.2114334

[C.7] L. Ursini, **F. Chiarello**, M. Santagiustina, and L. Schenato, "Comunicazioni sicure in spazio libero su portante ottica caotica", in *Fotonica 2010, 12° Convegno Nazionale delle Tecnologie Fotoniche*, (May 25–27, 2010), Pisa, Italy, 2010, P1.5

1.5 Acknowledgements

The following authorities and projects are acknowledged for financial support:

- the National Inter-University Consortium for Telecommunications (CNIT);
- the University of Padova, project ''Near Infrared Nonlinear Fiber Oscillators'' (NINFO);
- the Italian Ministry of Instruction, University and Research (MIUR), project ''Linear and nonlinear polarization sensitive effects in single mode birefringent optical fibers'' (POLARIZON).

Chapter 2

Nonlinear amplification processes in optical fibers

$$K_0 - K_1 = \frac{L}{V^2}\frac{v^2}{2}$$

Albert Einstein
1879 – 1955

Nonlinear optics phenomena arise from the saturation of the medium in response to strong electromagnetic fields. Consequently, nonlinear effects on optical waves can manifest in any type of media, provided that the energy is sufficiently high. Even the vacuum is predicted to become nonlinear for electromagnetic fields with power above the Schwinger limit [47].

In optical fibers, nonlinear effects are enhanced by the relatively small area in which the field is confined. In telecommunication, nonlinearities are detrimental as they pose serious limits on the utilization of the optical fiber to convey information. However, nonlinearities can be used to realize new classes of all-optical devices able to generate and manipulate light.

Of the broad range of nonlinear effects in optical fibers, this thesis focus on the amplification properties of fiber optical parametric amplification (FOPA) and of stimulated Raman scattering (SRS). FOPA and SRS are used in Chapter 3 to realize all-fiber oscillators, whereas in Chapter 4 SRS is used to control the polarization of light. This chapter provides a brief overview of those two amplification processes. Section 2.1 provides a short introduction on the origin of the nonlinear phenomena in optical fibers. The scalar theories of SRS and FOPA are briefly reviewed in Section 2.2 and Section 2.3, respectively.

More in-depth and comprehensive treatises of optical fields in nonlinear media can be found in book such as Sauter [48] or Boyd [49], whereas an exhaustive analysis and discussion of nonlinearities in optical fibers can be found in Agrawal [50]. Regarding the two specific processes used in this thesis, Marhic [51] deeply covers the theory and applications of FOPAs, whereas Headley and Agrawal [52] provides a broad coverage of SRS.

2.1 Origin of nonlinearities in optical fibers

The propagation of the electromagnetic field inside a medium other than vacuum is described by the Maxwell equations through the following constitutive relation between the electric displacement $\boldsymbol{D}$ and the electric field $\boldsymbol{E}$ [48]:

$$\boldsymbol{D} = \varepsilon_0 \boldsymbol{E} + \boldsymbol{P}\,, \tag{2.1}$$

where ε_0 is the electric permittivity of the vacuum and $\boldsymbol{P}$ is the polarization vector. In general $\boldsymbol{P}$ is a nonlinear function of $\boldsymbol{E}$ and it can be expanded as [50]:

$$\boldsymbol{P}(\boldsymbol{E}) = \varepsilon_0\big(\chi^{(1)}\boldsymbol{E} + \chi^{(2)}\boldsymbol{E}^2 + \chi^{(3)}\boldsymbol{E}^3 + \dots\big)\,, \tag{2.2}$$

where $\chi^{(i)}$ is the i-th order susceptibility which is in general a tensor of rank $i+1$. For silica optical fibers $\chi^{(2)}$ is zero because of the symmetry of the SiO_2 molecule; it can however manifest in asymmetric crystals like lithium-niobate ($LiNbO_3$). Silica optical fibers present the third-order susceptibility $\chi^{(3)}$, also commonly called the $\chi^{(3)}$-nonlinearity.

The $\chi^{(3)}$-nonlinearity gives rise to nonlinear phenomena such as the Kerr effect, stimulated Brillouin scattering (SBS) and SRS.

SBS and SRS involve scattering of photons with the molecular structure of the fiber, resulting in loss of energy due to the creation of phonons (optical phonons[1] in the case of SRS and acoustic phonons in the case of SBS). From a practical point of view, both SBS and SRS manifest as spontaneous processes in consequence of a pump wave with power above a certain threshold given by [53]:

$$P_{\text{th}} \approx C\frac{kA_{\text{eff}}}{gL_{\text{eff}}}\,, \tag{2.3}$$

where g is the gain coefficient of the process and where A_{eff} and L_{eff} are, respectively, the effective area[2] and the effective length[3]. The coefficient C depends on the particular process and on the particular configuration: for SBS in silica fibers $C = 21$ [53], whereas for SRS it can be $C = 16$ or $C = 20$ depending if the co-propagating or the counter-propagating configuration is considered [53]. The coefficient k lays in the range $1 \le k \le 2$ and accounts for the polarization properties. Under proper conditions, SBS and SRS became stimulated processes when another wave, called Stokes wave, is present. In such case energy is transferred from the pump to the Stokes wave, eventually resulting in its amplification.

[1] The term ''optical'' refer to the frequency of the electromagnetic wave necessary to excite the vibrations.

[2] The effective area is defined as [50]:

$$A_{\text{eff}} = \frac{\left(\iint_{-\infty}^{\infty}|F(x,y)|^2\,\mathrm{d}x\,\mathrm{d}y\right)^2}{\iint_{-\infty}^{+\infty}|F(x,y)|^4\,\mathrm{d}x\,\mathrm{d}y}\,, \tag{2.4}$$

where F is the modal distribution of the field. If a Gaussian profile for the mode is assumed, then $A_{\text{eff}} \approx \pi w^2$ with w being the waist of the beam [50].

[3] The effective length L_{eff} is defined as [50]:

$$L_{\text{eff}} = \frac{1}{P_0^{\text{in}}}\int_0^L P_0(z)\,\mathrm{d}z \approx \frac{1-\mathrm{e}^{-\alpha_p L}}{\alpha_p}\,, \tag{2.5}$$

where P_0 is the pump power and P_0^{in} is its value at the input of the fiber. The approximation holds for the scalar case in the undepleted pump approximation.

Instead, processes like self-phase modulation (SPM), cross-phase modulation (XPM) or four-wave mixing (FWM) are loss-less and originate from the Kerr effect, *i.e.* from the dependence of the refractive index on the intensity of the electromagnetic field:

$$n(\omega, I) = n_0(\omega) + n_2(\omega) I \,. \tag{2.6}$$

In Eq. (2.6), n_0 is the linear refractive index which in general is frequency dependent giving rise to chromatic dispersion. The nonlinear refractive index n_2 is related to the real part of $\chi^{(3)}$ and a commonly used value is 2.6×10^{-20} m^2 W^{-1} [50]. The nonlinear part of Eq. (2.6) depends on the optical intensity I of the waves propagating in the fiber, and its effects are better described by the nonlinear coefficient γ [54]:

$$\gamma = \frac{2\pi n_2}{\lambda A_{\text{eff}}} \,, \tag{2.7}$$

where λ is the wavelength.

For standard single-mode fibers (SMFs) at $\lambda = 1550$ nm, the nonlinear coefficient typically lays in the range from 1 W^{-1} km^{-1} to 3 W^{-1} km^{-1}. In fact by using the common value of $A_{\text{eff}} = 80\,\mu$m^2 Eq. (2.7) yields $\gamma \approx 1.3$ W^{-1} km^{-1}.

Highly nonlinear fibers (HNLFs), which have a reduced effective area A_{eff}, have a larger nonlinear coefficient ranging from $\gamma \approx 10$ W^{-1} km^{-1} to $\gamma \approx 20$ W^{-1} km^{-1}. HNLFs permit to enhance nonlinear effects enabling the use of shorter fibers with respect to standard ones. Using shorter fibers can have advantages such as a reduced impact of polarization-mode dispersion (PMD).

2.2 Stimulated Raman scattering

Stimulated Raman scattering (SRS) is a nonlinear process in which a pump wave at frequency ω_p and with power P_p transfers energy to a Stokes wave with power P_s at the downshifted frequency $\omega_s = \omega_p - \Delta\Omega$, where $\Delta\Omega$ is the Raman frequency shift. The difference in energy between the pump and Stokes photons is dissipated by the molecular vibrations through optical phonons. Moreover, energy transfer can happen both in the forward (co-propagating) and in the backward (counter-propagating) directions.

The properties of the medium determines both the frequency shift and the profile of the Raman gain. Fig. 2.1 shows the Raman gain spectrum for silica fibers. The amorphous structure of silica fibers render the gain very broad. In fact, for silica fibers, the peak of the Raman gain is downshifted by about $\Omega_{\text{R}} = 2\pi f_{\text{R}}$, where $f_{\text{R}} = 13.2$ THz. For a pump at $\lambda_p = 1550$ nm the corresponding shift of the peak is about 105 nm, providing a bandwidth of about 50 nm [56].

The evolution of the powers of the pump P_p and of the Stokes signal P_s along the fiber can be described by the following two coupled equations [50]:

$$\frac{\mathrm{d}P_s}{\mathrm{d}z} = -\alpha_s P_s + g_{\text{R}} P_p P_s \,, \tag{2.8a}$$

$$\xi \frac{\mathrm{d}P_p}{\mathrm{d}z} = -\alpha_p P_p - \frac{\omega_p}{\omega_s} g_{\text{R}} P_s P_p \,, \tag{2.8b}$$

where α_s and α_p are the attenuation coefficients at the frequencies of the signal and of the pump, respectively, and where g_{R} is the value of the Raman gain coefficient at the

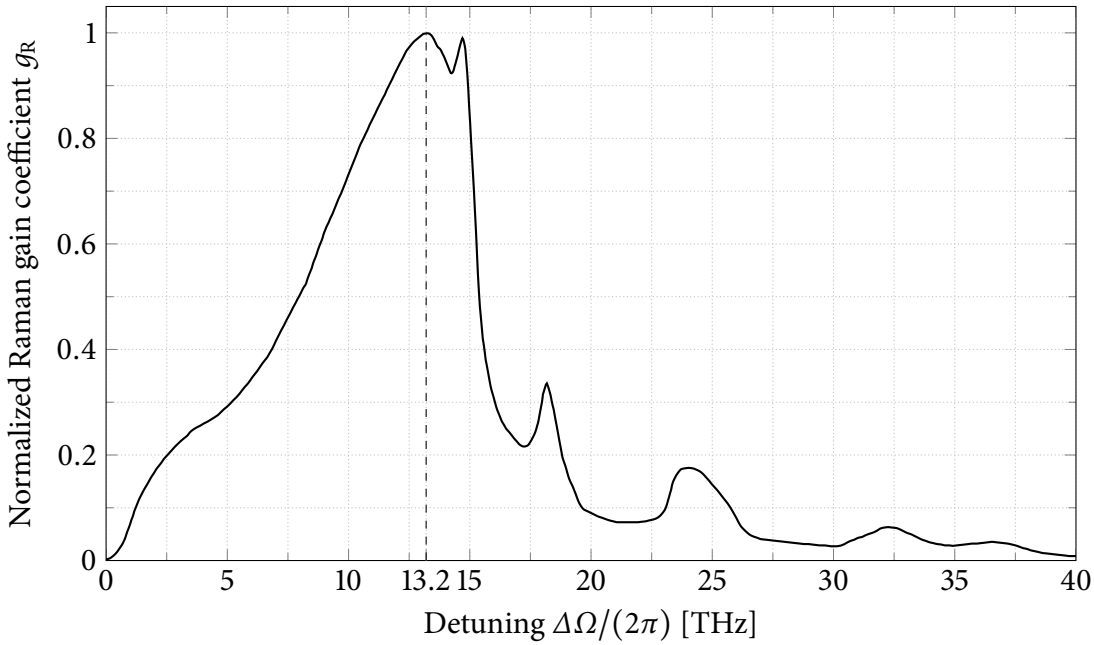

Figure 2.1: Normalized Raman gain coefficient g_R of silica fibers as a function of the pump-signal detuning $\Delta\Omega/(2\pi)$. The frequency shift of the peak is about 13.2 THz. Reprinted from [55] © 1984 OSA.

frequency of the signal ω_s. The scaling term ω_p/ω_s accounts for the different energies of photons at the frequency of the signal and of the pump; as already noted, the remaining energy $\hbar(\omega_p - \omega_s)$ is absorbed by the medium. In co-propagating configuration $\xi = 1$, whereas $\xi = -1$ if pump and signal are counter-propagating.

As delineated in Section 2.1, the establishment of SRS is characterized by a threshold power P_{th} given approximately by [50], [53]:

$$P_{\text{th}} \approx C\frac{kA_{\text{eff}}}{g_R L_{\text{eff}}}, \tag{2.9}$$

where, for silica fibers, $C = 16$ in co-propagating configurations, whereas $C = 20$ in counter-propagating schemes [53].

The coefficient k accounts for the polarization properties of the pump and of the Stokes signal and it is in the range $1 \leq k \leq 2$. In particular, $k = 1$ for co-polarized pump and signal, whereas $k = 2$ if their state of polarizations (SOPs) are decorrelated. Note that Eqs. 2.8 do not account for the SOPs of the signal and pump. A more complete model accounting for the vector properties of SRS will be presented in Section 4.2.

The threshold of Eq. (2.9) gives a rough estimate of the pump power required in order to have equal output pump and signal powers. By neglecting fiber losses ($\alpha_s = \alpha_p = 0$) and pump depletion ($P_s \ll P_p$), it can be shown that the evolution of the signal P_s grows exponentially and it can be described by [50]:

$$\frac{\mathrm{d}P_s}{\mathrm{d}z} = g_R P_s P_p, \tag{2.10}$$

which can be readily integrated yielding:

$$P_s^{\text{out}} = P_s^{\text{in}}\, \mathrm{e}^{g_R P_p L}. \tag{2.11}$$

where L is the fiber length and where $P_s^{\text{out}} = P_s(L)$ and $P_s^{\text{in}} = P_s(0)$ are the output and the input signal powers, respectively.

Therefore, the signal gain G can be estimated as

$$G = \frac{P_s^{\text{out}}}{P_s^{\text{in}}} = \mathrm{e}^{g_{\text{R}} P_p L} \,. \tag{2.12}$$

With the assumptions made above, Eq. (2.12) is valid for both the co- and the counter-propagating cases.

SRS can be stimulated if a signal P_s^{in} is present at the input of the fiber. However, SRS can also grow from spontaneous emission, *i.e.* from quantum fluctuations.

SRS can occur in any type of fiber, and its response time is in the order of the femtosecond. Moreover, another peculiar advantage of SRS is that it can occur at any wavelength by properly positioning the pump wavelength. In fact, the gain coefficient g_{R} scales with the inverse of the pump wavelength [46], [57]:

$$g_{\text{R}} \propto \frac{1}{\lambda_p} \,, \tag{2.13}$$

and its peak value is about one half of the nonlinear coefficient γ [57]–[59]:

$$g_{\text{R}}(\Omega_{\text{R}}) \approx \frac{\gamma}{2} \,. \tag{2.14}$$

2.3 Parametric amplification in optical fibers

Fiber optical parametric amplification (FOPA) uses FWM to provide amplification. In FWM, four waves[4] interact through the Kerr effect.

In FOPA applications, two strong pump waves at frequencies ω_{p1} and ω_{p2} provide amplification to a Stokes wave at ω_s and to an anti-Stokes wave at ω_a, provided that the following condition for photons energy conservation is satisfied [50], [51]:

$$\omega_{p1} + \omega_{p2} = \omega_s + \omega_a \,, \tag{2.15}$$

i.e. the energy of two photons from the two pumps is converted to two new photons, one for the Stokes and one for the anti-Stokes.

The equations describing two pump FOPA, in the scalar case, neglecting the losses, SRS and higher order dispersion, are given by [51]:

$$\frac{\mathrm{d}A_{p1}}{\mathrm{d}z} = \mathrm{i}\,\gamma P_{p1} A_{p1} + 2\,\mathrm{i}\,\gamma\big(P_{p2} + P_s + P_a\big)A_{p1} + 2\,\mathrm{i}\,\gamma A_s A_a A_{p2}^* \,\mathrm{e}^{\mathrm{i}\,\Delta\beta z} \,, \tag{2.16a}$$

$$\frac{\mathrm{d}A_{p2}}{\mathrm{d}z} = \mathrm{i}\,\gamma P_{p2} A_{p2} + 2\,\mathrm{i}\,\gamma\big(P_{p1} + P_s + P_a\big)A_{p2} + 2\,\mathrm{i}\,\gamma A_s A_a A_{p1}^* \,\mathrm{e}^{\mathrm{i}\,\Delta\beta z} \,, \tag{2.16b}$$

$$\frac{\mathrm{d}A_s}{\mathrm{d}z} = \mathrm{i}\,\gamma P_s A_s + 2\,\mathrm{i}\,\gamma\big(P_{p1} + P_{p2} + P_a\big)A_s + 2\,\mathrm{i}\,\gamma A_{p1} A_{p2} A_a^* \,\mathrm{e}^{-\mathrm{i}\,\Delta\beta z} \,, \tag{2.16c}$$

$$\frac{\mathrm{d}A_a}{\mathrm{d}z} = \mathrm{i}\,\gamma P_a A_a + 2\,\mathrm{i}\,\gamma\big(P_{p1} + P_{p2} + P_s\big)A_a + 2\,\mathrm{i}\,\gamma A_{p1} A_{p2} A_s^* \,\mathrm{e}^{-\mathrm{i}\,\Delta\beta z} \,, \tag{2.16d}$$

[4] In fact, despite the name, FWM interactions can involve more than four waves, and new signals at different wavelengths can be generated, some of which can be degenerate.

where A_i are the slowly varying envelopes of the waves $i \in \{p1, p2, s, a\}$, the star * represents conjugation, $P_i = |A_i|^2$ is the power of the wave i and

$$\Delta\beta = \beta_s + \beta_a - \beta_{p1} - \beta_{p2} \tag{2.17}$$

is the linear phase mismatch[5], with $\beta_i = \beta(\omega_i)$ being the propagation constant of the wave i.

FOPA can also be achieved through degenerate-FWM, in which the two pumps are at the same frequency $\omega_{p1} = \omega_{p2} = \omega_p$. As before, two photons of the pump are converted to two new photons to provide amplification to a Stokes wave at $\omega_s < \omega_p$ and to an anti-Stokes wave at $\omega_a > \omega_p$. In this case, the energy conservation relation becomes

$$2\omega_p = \omega_s + \omega_a\,, \tag{2.18}$$

and the equations describing the phenomenon are given by [51], [60]–[62]:

$$\frac{\mathrm{d}A_p}{\mathrm{d}z} = \mathrm{i}\,\gamma P_p A_p + 2\,\mathrm{i}\,\gamma(P_s + P_a)A_p + 2\,\mathrm{i}\,\gamma A_s A_a A_p^* \,\mathrm{e}^{\mathrm{i}\,\Delta\beta z}\,, \tag{2.19a}$$

$$\frac{\mathrm{d}A_s}{\mathrm{d}z} = \mathrm{i}\,\gamma P_s A_s + 2\,\mathrm{i}\,\gamma\big(P_p + P_a\big)A_s + \mathrm{i}\,\gamma A_p^2 A_a^* \,\mathrm{e}^{-\mathrm{i}\,\Delta\beta z}\,, \tag{2.19b}$$

$$\frac{\mathrm{d}A_a}{\mathrm{d}z} = \mathrm{i}\,\gamma P_a A_a + 2\,\mathrm{i}\,\gamma\big(P_p + P_s\big)A_a + \mathrm{i}\,\gamma A_p^2 A_s^* \,\mathrm{e}^{-\mathrm{i}\,\Delta\beta z}\,, \tag{2.19c}$$

where the linear phase mismatch is

$$\Delta\beta = \beta_s + \beta_a - 2\beta_p\,. \tag{2.20}$$

In the undepleted pump approximation the following parametric gain coefficient g can be derived from Eqs. 2.19 [50], [51]:

$$g = \sqrt{\big(\gamma P_p\big)^2 - \left(\frac{\kappa}{2}\right)^2}\,, \tag{2.21}$$

where

$$\kappa = \Delta\beta + 2\gamma P_p \tag{2.22}$$

is the nonlinear phase mismatch. As it can be seen, real and positive gain g can be achieved for

$$-4\gamma P_p < \Delta\beta < 0\,. \tag{2.23}$$

Perfect nonlinear phase matching is defined as:

$$\kappa = \Delta\beta + 2\gamma P_p = 0\,, \tag{2.24}$$

in which case Eq. (2.21) is maximized yielding

$$g_{\mathrm{MAX}} = \gamma P_p\,. \tag{2.25}$$

[5]Here it has been assumed a time dependence of $\mathrm{e}^{\mathrm{i}\,\omega t}$. By assuming, instead, a time dependence of $\mathrm{e}^{-\mathrm{i}\,\omega t}$ the signs of Eq. (2.17) are reversed.

If only the pump and the Stokes signal are present[6] at the input of a fiber of length L, the Stokes gain G can be expressed as [50], [51]:

$$G = \frac{P_s(L)}{P_s(0)} = 1 + \left(\gamma P_p \frac{\sinh(gL)}{g}\right)^2 , \tag{2.26}$$

which, in the case $gL \gg 1$, can be well approximated by:

$$G \approx \frac{1}{4} e^{2\gamma P_p L} . \tag{2.27}$$

During the interaction, part of the energy from the pump is transferred to the Stokes, and part is used to generate a new signal at the anti-Stokes frequency, which at the output of the fiber has a power given by

$$P_a(L) = P_s(0)(G_s - 1) , \tag{2.28}$$

and a phase related to that of the Stokes signal.

As a note, if both the Stokes and the anti-Stokes are present at the input of the fiber, their gain depends on their relative phase. In this case the process is called phase-sensitive fiber optical parametric amplification (PS-FOPA) [63].

2.3.1 Broad-band fiber optical parametric amplification

As written before, in FOPA, maximum gain is achieved for perfect nonlinear phase matching, given by Eq. (2.24):

$$\Delta\beta = -2\gamma P_p . \tag{2.29}$$

If the pump is set near the zero-dispersion wavelength (ZDW)[7] so that $\beta_p \approx \beta_0$, the propagation constant β can be approximated around the pump frequency ω_p by its second order Taylor expansion:

$$\beta(\omega) \approx \beta_{0,p} + \beta_{1,p}\Delta\omega + \frac{1}{2}\beta_{2,p}\Delta\omega^2 , \tag{2.31}$$

where $\Delta\omega = \omega_i - \omega_p$ and

$$\beta_{j,p} = \left.\frac{d^j\beta(\omega)}{d\omega^j}\right|_{\omega=\omega_p} . \tag{2.32}$$

The index $i \in \{s, a\}$ refer to the Stokes and the anti-Stokes, respectively. By using this expansion, the linear phase mismatch of Eq. (2.20) becomes

$$\Delta\beta = \beta_{2,p}\Delta\omega^2 , \tag{2.33}$$

[6]The same holds true if only the anti-Stokes is present together with the pump.

[7]The ZDW is the wavelength $\lambda_0 = 2\pi c/\omega_0$ for which

$$\beta_2 = \left.\frac{d^2\beta(\omega)}{d\omega^2}\right|_{\omega=\omega_0} = 0 . \tag{2.30}$$

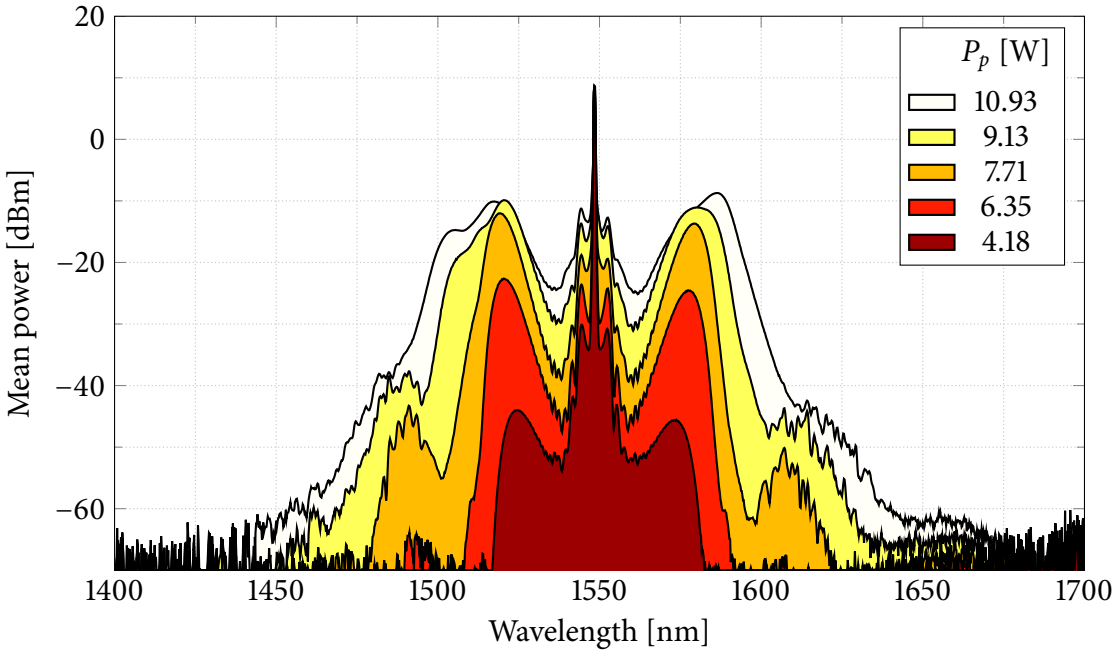

Figure 2.2: Amplified spontaneous emission of a 500 m long DSF for different pump powers. The spectra are obtained by pumping in the anomalous dispersion regime at λ_p = 1548.50 nm.

and therefore perfect nonlinear phase matching can be achieved for

$$\beta_{2,p}\Delta\omega^2 = -2\gamma P_p\,, \tag{2.34}$$

which is satisfied for

$$\beta_{2,p} < 0\,. \tag{2.35}$$

This last condition individuates the anomalous dispersion regime ($\beta_{2,p} < 0$) of the fiber as the region in which to set the pump in order to achieve phase matching and therefore maximum gain.

Fig. 2.2 and Fig. 2.3 show different amplified spontaneous emission (ASE) spectra obtained by pumping in the anomalous dispersion regime. The fiber is a dispersion-shifted fiber (DSF) G.653 with $\gamma \approx 2\,\mathrm{W^{-1}\,km^{-1}}$ and ZDW $\lambda_0 \approx 1548\,\mathrm{nm}$. This regime is called broad-band fiber optical parametric amplification (BBFOPA) [64], [65], and, as it can be seen, gain is found for signal wavelengths around the pump wavelength [65].

In particular, if the pump is exactly set at λ_0, the width $\delta\lambda$ of the gain region can be expresses as [64]:

$$\delta\lambda = 2\sqrt[4]{\frac{3\gamma P_p}{|\beta_4|}}\,, \tag{2.36}$$

where β_4 is the fourth-order coefficient of β. Actually, $\delta\lambda$ is the maximum achievable gain width. As it can be seen in Fig. 2.3, as the pump is moved from the ZDW into the anomalous dispersion regime, the width of the gain region gets reduced.

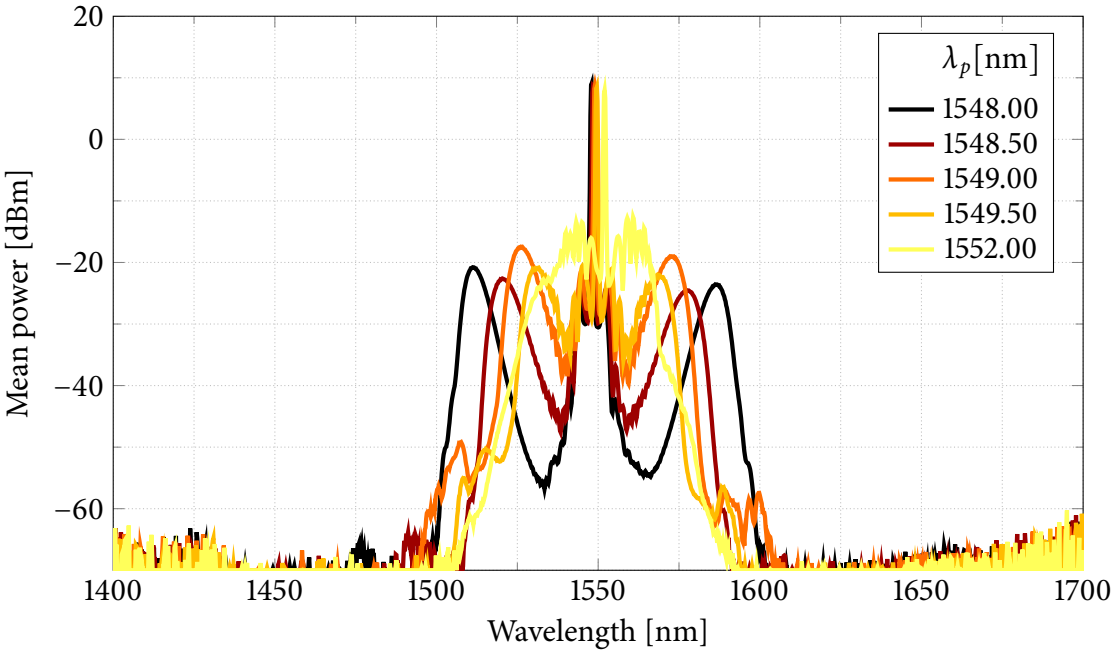

Figure 2.3: Amplified spontaneous emission of a 500 m long DSF for different pump wavelengths in the anomalous dispersion regime. The pump power is $P_p = 6.35\,\mathrm{W}$.

2.3.2 Narrow-band fiber optical parametric amplification

Phase matching is possible also in the normal dispersion regime ($\beta_{2,p} > 0$). As before, by considering the 4$^{\text{th}}$-order expansion of β around ω_p:

$$\beta(\omega) \approx \beta_{0,p} + \beta_{1,p}\Delta\omega + \frac{1}{2}\beta_{2,p}\Delta\omega^2 + \frac{1}{6}\beta_{3,p}\Delta\omega^3 + \frac{1}{24}\beta_{4,p}\Delta\omega^4\,, \tag{2.37}$$

the nonlinear phase matching condition becomes

$$\beta_{2,p}\Delta\omega^2 + \frac{1}{12}\beta_{4,p}\Delta\omega^4 = -2\gamma P_p\,, \tag{2.38}$$

and therefore perfect phase matching can be still be attained provided that

$$\beta_{4,p} < 0\,. \tag{2.39}$$

Fig. 2.4 and Fig. 2.5 show different ASE spectra obtained by pumping in the normal dispersion regime. The fiber is a DSF (G.653) with $\gamma \approx 2\,\mathrm{W^{-1}\,km^{-1}}$ and ZDW $\lambda_0 \approx 1548\,\mathrm{nm}$. In analogy with BBFOPA, this regime is called narrow-band fiber optical parametric amplification (NBFOPA) [64], [66], and is characterized by two narrow gain regions well detuned from the pump [64], [66], [67].

The bandwidth $\delta\lambda$ of the two gain regions can be approximately given by [64]:

$$\delta\lambda \approx \frac{24\gamma P_p \lambda_0^8}{(2\pi c)^4}\left|\beta_4(\Delta\lambda)^3\right|^{-1}\,, \tag{2.40}$$

where $\Delta\lambda$ is the wavelength separation of the gain region from the pump.

With appropriate fiber characteristics the gain regions can be extended well above 2000 nm and below 1300 nm [68], [69]. The presence of different peaks in the gain regions, clearly visible in Fig. 2.5, can be attributed to the variations of the ZDW along the fiber [70].

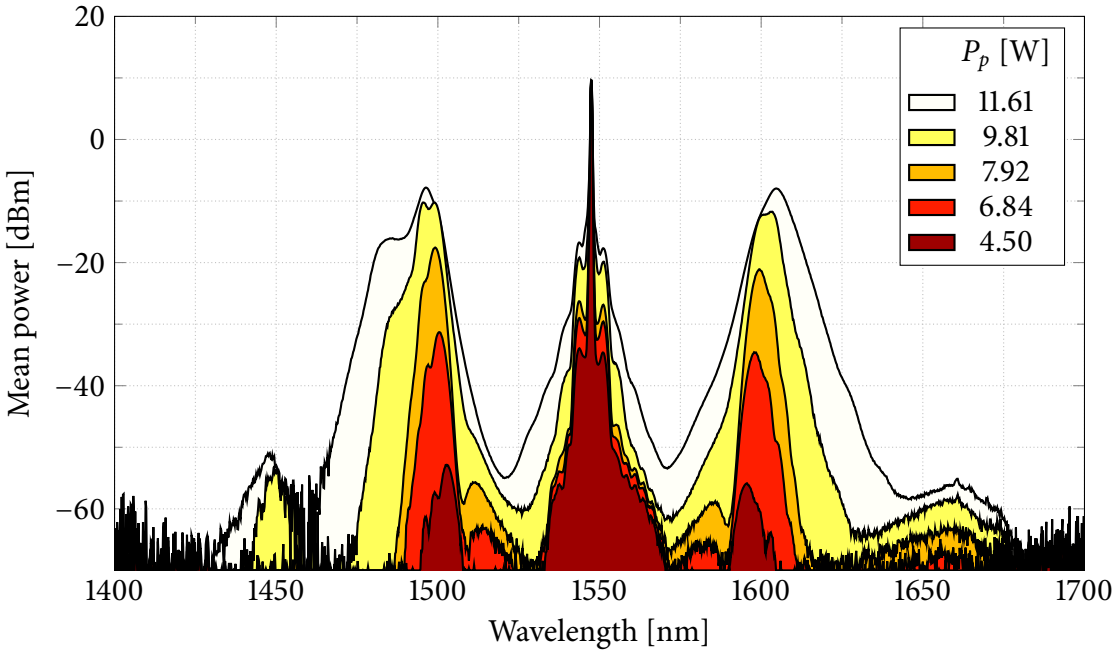

Figure 2.4: Amplified spontaneous emission of a 500 m long DSF for different pump powers. The spectra are obtained by pumping in the normal dispersion regime at λ_p = 1547.50 nm.

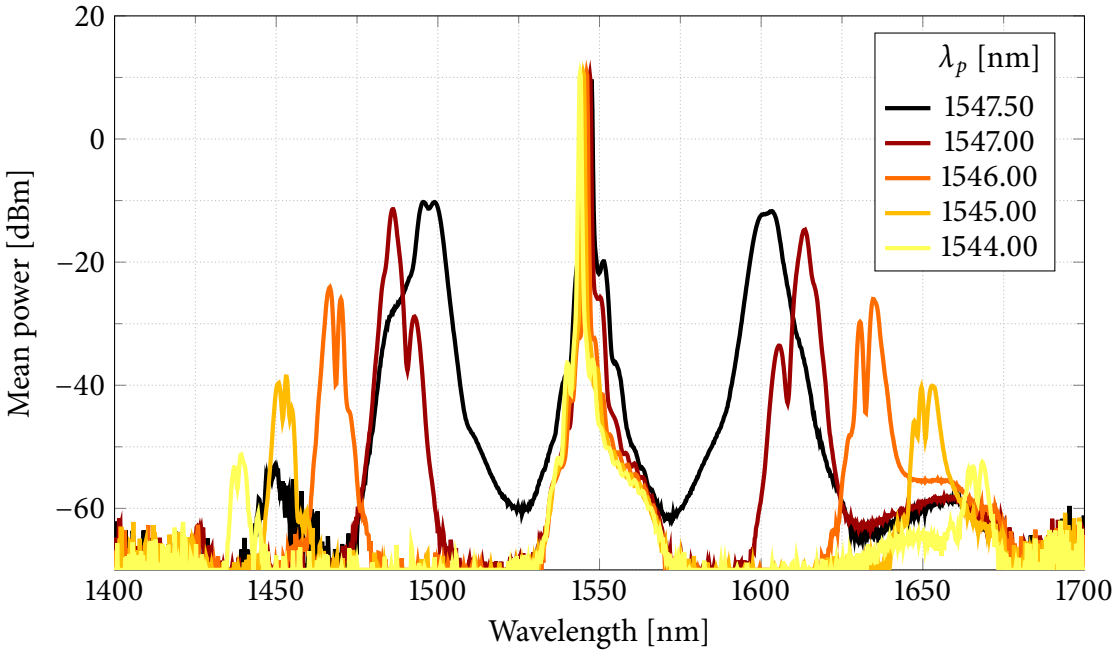

Figure 2.5: Amplified spontaneous emission of a 500 m long DSF for different pump wavelengths in the normal dispersion regime. The pump power is P_p = 9.81 W.

Chapter 3

Nonlinear fiber optical oscillators

$$\varepsilon = h\nu$$

Max Karl Ernst Ludwig Planck
1858 – 1947

This chapter presents the topic of all-fiber optical sources based on nonlinear amplification processes. Over the past two decades, all-fiber lasers have been the subject of a considerable amount of research owing to the several potential advantages they present with respect to bulk lasers. The lack of critical components such as mirrors, crystals or prisms makes all-fiber lasers very attractive due to the lower complexity and higher ruggedness; moreover, being fiber-based, they can have high coupling efficiency and beam quality, and inherently single spatial mode operations.

In the following Section 3.1 a continuous-wave (CW) pump for fiber Raman amplifiers (FRAs)-based nonlinear polarization attractions (NPAs) is presented. The pump has been developed with the goal of achieving high degree of polarization (DOP), tunability and stimulated Brillouin scattering (SBS) suppression. Then, in Section 3.2 the time-dispersion-tuning (TDT) technique is briefly reviewed. TDT is applied to realize a widely tunable fiber optical oscillator, presented in Section 3.3. The oscillator is based on three nonlinear processes, namely stimulated Raman scattering (SRS), broad- and narrow-band fiber optical parametric amplification (FOPA), and it results tunable over 160 nm. Finally, in Section 3.4 the use of TDT in a fast tunable optical frequency comb (OFC) based on cascaded four-wave mixing (CFWM) is described.

3.1 Continuous wave pump for fiber Raman amplifiers

In long-haul FRAs applications, in order to reduce the effects related to the polarization-dependent gain (PDG) of the SRS process, it is a common practice to use a depolarized pump [71]–[80], *e.g.* by scrambling its state of polarization (SOP) or by multiplexing orthogonal pumps. Nevertheless, the PDG is the key feature to analyze the gain and polarization properties of NPA in counter-propagating FRAs, thus there is the need of a fully polarized and CW Raman pump.

The main drawback of using a highly polarized CW pump is associated to its depletion induced by the SBS effect [81], which, being two orders of magnitude more efficient than SRS, limits the maximum usable pump power to few tens of milliwatt, and it is generally detrimental [82], [83]. The aim of this section is therefore the development of a polarized CW pump with high power to be used to realize NPA in FRAs.

3.1.1 Stimulated Brillouin scattering

SBS is a nonlinear process in which, similarly to SRS, a pump wave at frequency ω_p and with power P_p transfers energy to a counter-propagating Stokes wave with power P_{SBS} at the downshifted frequency $\omega_s = \omega_p - \Omega_{\mathrm{B}}$, where Ω_{B} is the Brillouin frequency shift. In silica fibers, the frequency shift $f_{\mathrm{B}} = \Omega_{\mathrm{B}}/(2\pi)$ typically varies in the range from 9 GHz to 12 GHz [50]. The physical process enabling the energy transfer is however different from that occurring for SRS.

SBS is induced by the process of electrostriction, through which the pump, if sufficiently intense, generates a co-propagating acoustic wave which travels at the speed of sound v_A in the fiber ($v_A \approx 6\,\mathrm{km\,s^{-1}}$ for silica fibers [50]). The refractive index n is therefore modulated by the pressure exerted by the acoustic wave and acts as a moving grating, causing Bragg diffraction of the pump. The downshift of the Stokes wave frequency by the amount Ω_{B} is given by the Doppler effect of the grating moving at speed v_A, and it can be written as

$$\Omega_{\mathrm{B}} = 2\pi f_{\mathrm{B}} = 2\pi \frac{2 n_p v_A}{\lambda_p}\,, \tag{3.1}$$

where $\lambda_p = 2\pi c/\omega_p$ is the wavelength of the pump (c is the speed of light in vacuum), and $n_p = n(\omega_p)$.

As delineated in Chapter 2, the establishment of SBS is characterized by a threshold power P_{th} given approximately by [50], [53], [84]:

$$P_{\mathrm{th}} \approx C \frac{k A_{\mathrm{eff}}}{g_{\mathrm{B}}(f_{\mathrm{B}}) L_{\mathrm{eff}}} \left(1 + \frac{\Delta f_p}{\Delta f_{\mathrm{B}}}\right), \tag{3.2}$$

where $C = 21$ for silica fibers [53] and $1 \leq k \leq 2$ accounts for the polarization properties of the pump and of the Stokes signal [85]. In particular, $k = 1$ for co-polarized pump and signal, whereas $k = 2$ if their SOPs are decorrelated. $g_{\mathrm{B}}(\Omega_{\mathrm{B}})$ is the value of the Brillouin coefficient at the Brillouin frequency shift Ω_{B} from the pump, whereas Δf_p and Δf_{B} are, respectively, the linewidth of the pump and of the Brillouin gain. The linewidth of the gain spectrum is related to the lifetime of the acoustic phonon, and, in silica fibers, Δf_{B} typically varies in the range from 10 MHz to 100 MHz [50]. L_{eff} and A_{eff} are, respectively, the effective length and the effective area. The Brillouin gain and the pump spectral profiles can be assumed to have a Lorentzian shape. In this case the effective area can be approximated by [86]

$$A_{\mathrm{eff}} \approx 2\pi W^2\,, \tag{3.3}$$

where W is the mode field radius.

When the pump input power P_p^{in} exceeds the threshold P_{th}, the evolution of the backscattered signal P_{SBS} due to SBS starts to grow exponentially and can be described by [50]:

$$\frac{\mathrm{d}P_{\mathrm{SBS}}}{\mathrm{d}z} = g_{\mathrm{B}} P_{\mathrm{SBS}} P_p\,, \tag{3.4}$$

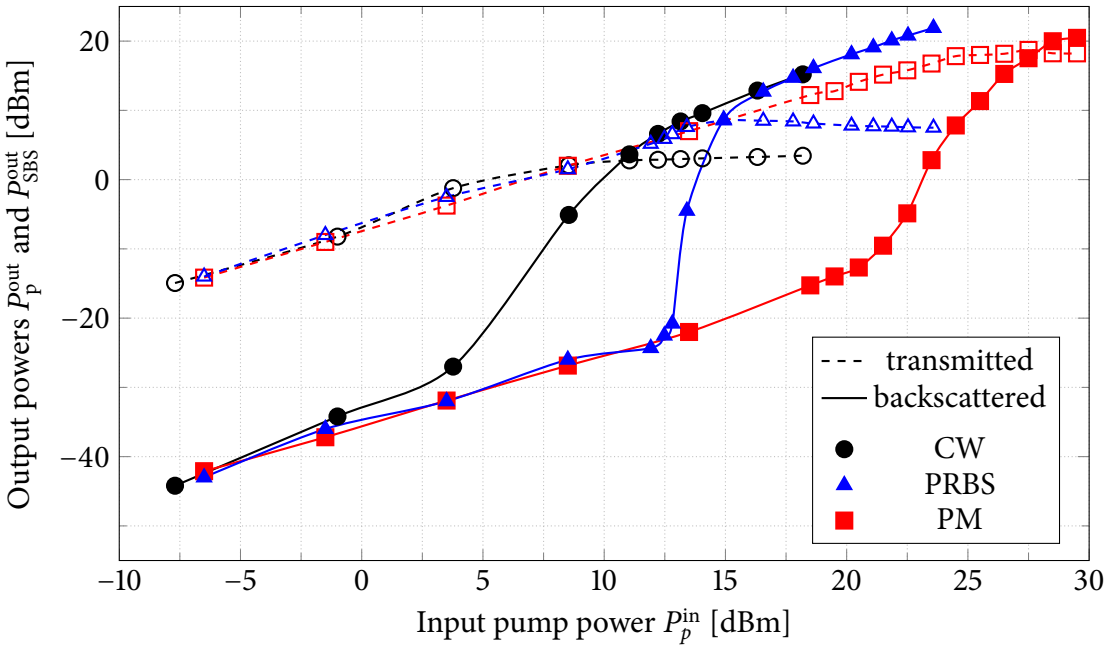

Figure 3.1: Measured transmitted P_p^{out} (dashed curves) and backscattered P_{SBS}^{out} (solid curves) powers as functions of the input power, for a 25 km long G.655 NZDSF. Circles refer to a CW laser source. Triangles refer to the same source being intensity-modulated by 10 Gbit s^{-1} pseudo-random binary sequence (PRBS) patterns, whereas squared refer to the same source being phase-modulated by a single sinusoidal tone (the frequency of the tone is chosen to maximize the threshold).

where fiber losses, pump depletion and polarization effects have been neglected, resulting in

$$P_{SBS}^{out} = P_{SBS}^{in} e^{g_B P_p L} . \tag{3.5}$$

SBS can be stimulated if a counter-propagating signal P_{SBS}^{in} is present in the fiber. However, SBS can also grow from spontaneous emission (quantum fluctuations), in which case it became a stimulated process from noise.

3.1.2 Suppression of stimulated Brillouin scattering

Suppressing the SBS effect means increasing its threshold P_{th} defined in Eq. (3.2), which can be achieved by controlling the parameters defined there.

The threshold can be doubled by scrambling the SOP of the pump and consequently lowering its DOP, in which case $k = 2$. However, as explained above, one of the requirement is to have unitary DOP, *i.e.* $k = 1$.

Another common practice to increase the threshold is by broadening the spectrum of the pump, *i.e.* by increasing its linewidth Δf_p. This can be attained for example by internal or external modulation of the pump [82], [83]. In particular, phase modulation has proven to be effective [87]–[90] in communications applications because it permits to maintain the intensity unaltered, limiting relative intensity noise (RIN) transfers.

Fig. 3.1 shows the measured transmitted P_p^{out} (dashed curves) and backscattered P_{SBS}^{out} (solid curves) powers as functions of the input pump power, for a 25 km long non-zero

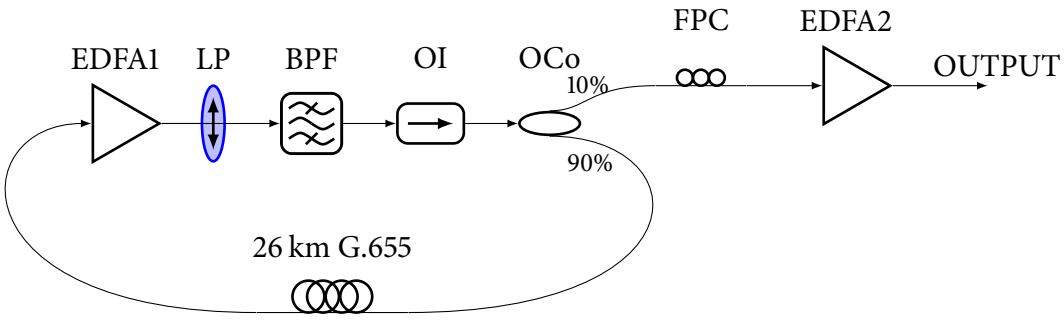

Figure 3.2: Experimental setup of the CW fiber ring laser. EDFA: erbium-doped fiber amplifier; LP: linear polarizer; BPF: band pass filter; OI: optical isolator; OCo: optical coupler; FPC: fiber polarization controller.

dispersion-shifted fiber (NZDSF) G.655 fiber. For low input powers, both the transmitted and the backscattered powers grow linearly with length. The backscattered power is dominated by Rayleigh scattering [91], [92], which is typically about 40 dB lower than the input power. Conversely, in this low power regime the transmitted power is only affected by the loss of the fibers.

As it can be seen, for a CW pump (circles) at input power P_p^{in} of about 5 dBm, the backscattered power $P_{\text{SBS}}^{\text{out}}$ starts to grow exponentially, eventually outreaching the transmitted power P_p^{out} for $P_p^{\text{in}} > 11$ dBm. By intensity-modulating the laser with a 10 Gbit s^{-1} PRBS pattern (triangles) an improvement of the threshold of few decibels is obtained. Even higher improvement is attained by only modulating the phase of the source with a single tone (squares). However, even in this case, the SBS starts to manifest for input power of about 20 dBm.

Other techniques rely on the break of the exponential grow of the backscattered wave. This can be obtained by inserting isolators along the fiber [93], or by varying the Brillouin frequency shift Ω_{B} [86], [94], [95] or the effective area A_{eff}. Such variations can be obtained by varying the core radius [96]–[98] and the doping concentration [99]–[101], or by applying temperature [88], [97], [102]–[105] or strain [100], [104], [106], [107] gradients.

For reasons of practical opportunity, however, in our setup we preferred to use standard fibers; therefore SBS suppression has been pursued by modulating the pump. Furthermore, in order to further increase the SBS threshold, a multi-frequency fiber ring laser has been implemented.

Fig. 3.2 shows the experimental setup of the ring laser. The oscillation in the ring is triggered by the amplified spontaneous emission (ASE) generated by the erbium-doped fiber amplifier (EDFA1). The ASE, after being polarized by a linear polarizer (LP), passes through a tunable band pass filter (BPF) with bandwidth of about 0.9 nm, equivalent to about 112.5 GHz at 1550 nm. The filtered ASE is then feed back in the loop by a optical coupler (OCo) and amplified again by the EDFA1. The 26 km-long G.655 fiber is used to lengthen the cavity. The optical isolator (OI) forces unidirectionality and protects from possible backscattering from the fiber.

By only considering the EDFA1 closed on itself and assuming 25 m of erbium-doped fiber (EDF), the resulting free spectral range (FSR) is approximately given by

$$\Delta\nu = \frac{c}{n_g L} \approx 8\,\text{GHz}\,, \tag{3.6}$$

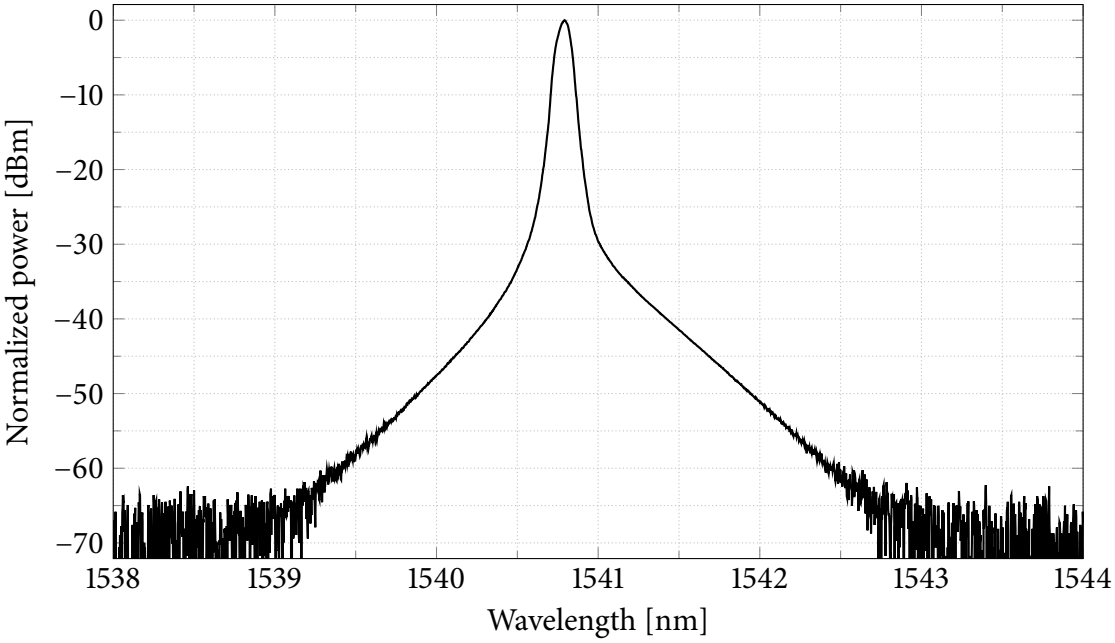

Figure 3.3: Spectrum generated by the CW fiber ring laser.

where c is the speed of light in vacuum and n_g is the group index. The effect of the 26 km-long fiber is to reduce the FSR by about a factor of 10^3, resulting in $\Delta\nu \approx 8$ MHz. In ideal conditions, by considering the width of the BPF, a total of about 1.5×10^5 lines would be oscillating. However, even if the spectrum of the gain of the EDFA1 can be considered flat in the band of the BPF, the latter is not flat. Therefore, there is competition between the different oscillating modes, resulting in the spectrum shown in Fig. 3.3 measured by an optical spectrum analyzer (OSA). The linewidth at −10 dB from the peak is about 0.15 nm, corresponding to $\Delta f_{p,-10\,\mathrm{dB}} \approx 20$ GHz. The fiber polarization controller (FPC) and the EDFA2 are used, respectively, to control the output SOP and power. The laser, through the BPF, can be tuned over all the amplification band of the EDFAs, *i.e.* from 1535 nm to 1565 nm.

Finally, Fig. 3.4 shows the gain G obtained by using the above described ring laser as a pump in a counter-propagating FRA. The fiber used for the FRA is a 25 km long G.655 NZDSF, and the gain is defined as

$$G = \frac{S_0^{\mathrm{out}}}{S_0^{\mathrm{in}}}\,, \tag{3.7}$$

where S_0 is the power of the signal undergoing Raman amplification.

As it can be seen, the ring laser outperforms the phase-modulated pump, which was subjected to strong SBS depletion as shown in Fig. 3.1. The saturation of the gain happening for pump power above 33 dBm can be attributed to depletion due to SRS, as it will be explained in Chapter 4.

3.2 The time-dispersion-tuning technique

Time-dispersion-tuning (TDT) is a technique apt to enable wide and fast wavelength-tuning [108]–[113].

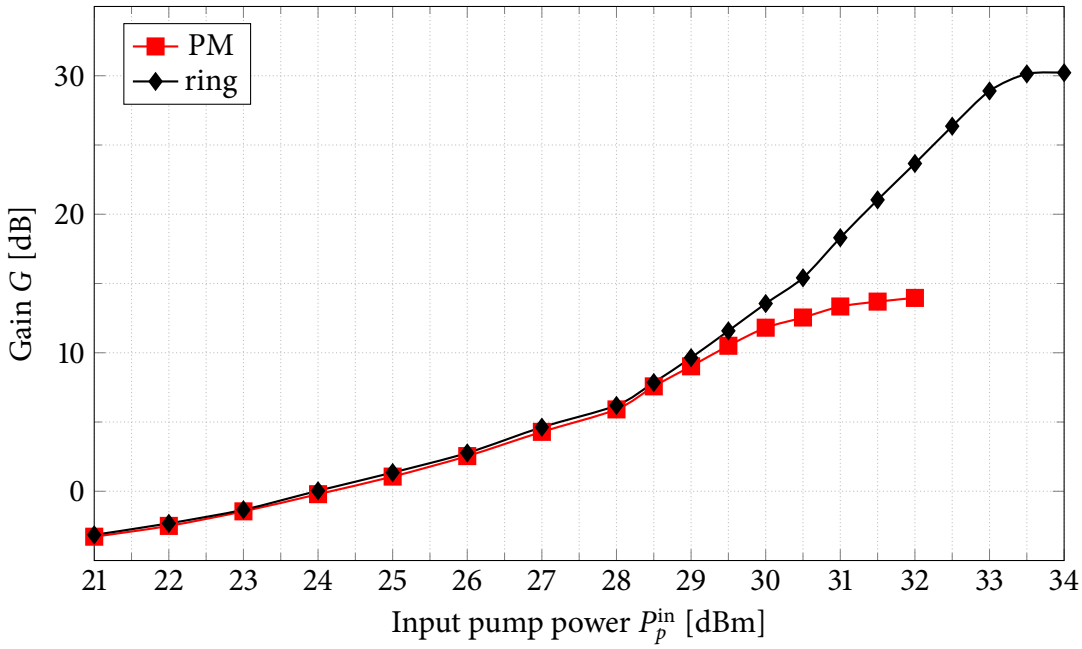

Figure 3.4: Measured signal gain G in a counter-propagating FRA. The fiber is a 25 km long G.655 NZDSF. Results using a phase-modulated pump (red squares) and the CW fiber ring laser (black circles) are compared.

TDT can be applied to a fiber loop laser into which a pulsed pump injects a train of pulses with repetition frequency f at the optical frequency ω_p. Each pump pulse generates inside the loop a new signal pulse at the optical frequency ω, which depend on the particular amplification process occurring in the loop. The propagation constant of the signal can be approximated by its second order Taylor expansion around the pump frequency ω_p:

$$\beta(\omega) \approx \beta_0 + \beta_1 \Delta\omega + \frac{1}{2}\beta_2 \Delta\omega^2 , \tag{3.8}$$

where $\Delta\omega = \omega - \omega_p$ and

$$\beta_j = \left. \frac{\mathrm{d}^j \beta(\omega)}{\mathrm{d}\omega^j} \right|_{\omega=\omega_p} . \tag{3.9}$$

In particular the second order coefficient β_2 is the group velocity dispersion (GVD) parameter taking into account for the chromatic dispersion. Due to chromatic dispersion, each frequency components of the signal pulse travel at the respective group velocity $v_g(\omega)$:

$$v_g(\omega) = \frac{1}{\beta_1(\omega)} , \tag{3.10}$$

which, by using the above expansion, can be rewritten as:

$$\frac{1}{v_g(\omega)} = \beta_1 + \beta_2 \Delta\omega = \frac{1}{v_g(\omega_p)} + \beta_2 \Delta\omega . \tag{3.11}$$

After a propagation of length L, the relative delay $\Delta\tau = \tau(\omega) - \tau(\omega_p)$ accumulated by components separated by $\Delta\omega$ can be calculated as

$$\Delta\tau = L\left(\frac{1}{v_g(\omega)} - \frac{1}{v_g(\omega_p)} \right) = \beta_2 L \Delta\omega = D_c L \Delta\lambda , \tag{3.12}$$

where, in the last equality, $\Delta\lambda$ is the wavelength separation and

$$D_c = -\frac{2\pi c}{\lambda^2}\beta_2 \tag{3.13}$$

is the chromatic dispersion coefficient. Typically the chromatic dispersion coefficient D_c is also accompanied by the dispersion slope coefficient S_0, defined as

$$S_0 = \left.\frac{\mathrm{d}D_c(\lambda)}{\mathrm{d}\lambda}\right|_{\lambda=\lambda_0}, \tag{3.14}$$

where λ_0 is the zero-dispersion wavelength (ZDW) of the fiber, *i.e.* S_0 is the first order coefficient of the Taylor expansion of $D_c(\lambda_0) \approx S_0\Delta\lambda$.

In a fiber loop, TDT exploits such wavelength dependence of the signal group velocity to synchronize only a narrow band of the feed back signal with a new incoming pump pulse. In fact, the synchronization condition requires that the signal pulse time of flight in the loop must equal an integer multiple N of the pulse repetition period:

$$\frac{L}{v_g(\omega)} = \frac{N}{f}. \tag{3.15}$$

The laser tuning slope, as a function of the pump repetition rate, can be calculated by defining f_p to be the pump repetition frequency necessary for self-synchronization:

$$f_p = N\frac{v_g(\omega_p)}{L}, \tag{3.16}$$

i.e. f_p is the repetition frequency for which the wavelength of the pump pulses traveling in the loop is synchronized with the incoming pulses from the pump. If the pump repetition rate is shifted by $\Delta f = f - f_p$ the optical frequency synchronized with a new pump pulse shifts by an amount $\Delta\Omega = \omega_p - \omega$ that can be approximated by

$$\Delta\Omega \simeq \frac{\Delta f}{\beta_2(\omega_p) f_p v_g(\omega_p)}, \tag{3.17}$$

where it has been assumed $\Delta f \ll f_p$. An equivalent formula [113] can be obtained for the corresponding wavelength shift:

$$\Delta\lambda \simeq S_\lambda \Delta f = \frac{-\Delta f}{D_c(\lambda_p) f_p v_g(\omega_p)}. \tag{3.18}$$

It is worth to note that TDT can be used in conjunction with any gain process. In [108] SRS was exploited in a non-dispersive loop, and TDT was implemented by mechanically controlling the length of the loop. However, the achieved tuning was slow due to the slow mechanical stages.

On the contrary, with the technique described above, tuning rates of 4 nm μs^{-1} can be obtained [112]–[114]. For instance, in [113], [114] broad-band fiber optical parametric amplification (BBFOPA) was exploited and tunability over 100 nm was achieved by modifying the pump pulse repetition rate f.

In particular, TDT completely removes the need of mechanically tunable devices if the pump pulse repetition frequency f is changed to adjust synchronization, therefore making the system extremely fast to tune. Moreover, by properly controlling the dispersion properties of the loop, the tuning slope can be modified.

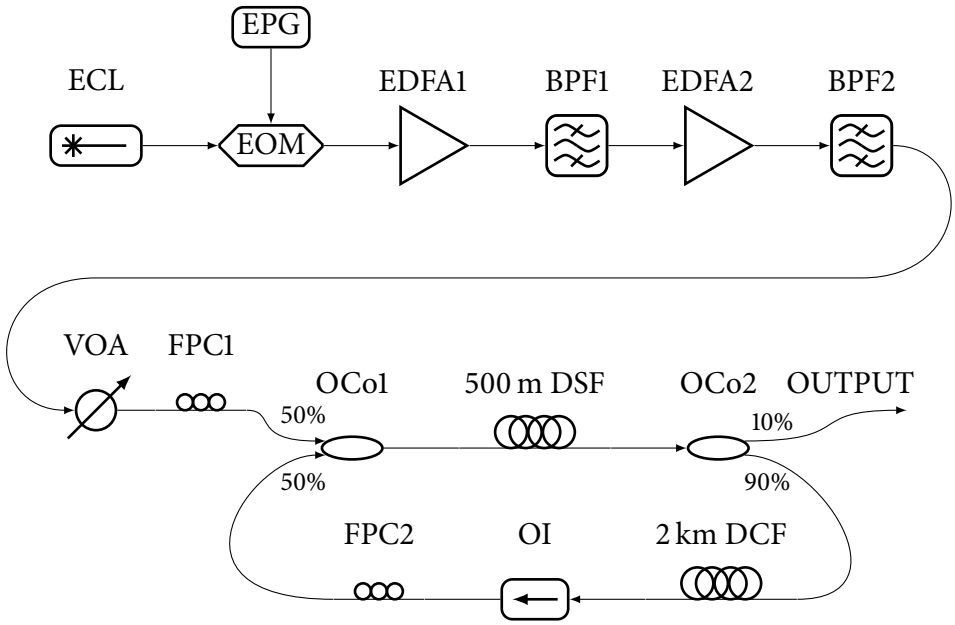

Figure 3.5: Experimental setup of the widely tunable fiber laser. ECL: external cavity laser; EOM: electro-optic modulator; EPG: electrical pulse generator; EDFA: erbium-doped fiber amplifier; BPF: band pass filter; VOA: variable optical attenuator; FPC: fiber polarization controller; OCo: optical coupler; OI: optical isolator. Reprinted from [P.1] © 2013 OSA.

3.3 Widely tunable oscillator based on multiple processes

In this section, based on the publications [P.1] and [C.1], a widely tunable all-fiber oscillator is presented and experimentally characterized. The optical oscillator is based on three different nonlinear amplification processes: stimulated Raman scattering, narrow- and broad-band FOPA. Each process dominates in a different wavelength range, and through the TDT technique wide wavelength tuning spanning 160 nm is achieved. When FOPA is used, the oscillator also takes the name of fiber optical parametric oscillator (FOPO).

Conventional lasers have fundamental limitations on the range and speed of tuning due to the presence of mechanically controlled optical filters and gratings. For example widely tunable lasers, such as the external cavity lasers (ECLs), have a low sweep rate while the tuning range of fast tunable lasers[1] is usually narrow. In this respect, all-fiber lasers can overcome such limitations.

Moreover, high-speed and wide-range wavelength tuning are mandatory requirements for applications in optical coherence tomography [4], distributed remote sensing [5], chromatic dispersion measurement [115] and in dense wavelength-division-multiplexing optical telecommunication networks [6]. The needs of such fast, compact and high performance devices have been spurring research into all-fiber lasers.

3.3.1 Experimental setup

The laser is constituted by an optical pulse generator which injects a train of high peak power pulses in a highly dispersive fiber ring. The experimental setup is shown in Fig. 3.5. The pulsed pump, at the top, generates a train of optical pulses with a duration of 1 ns and a repetition rate f_p of about 2.31 MHz. Such train is carved from the CW beam emitted by the ECL through an electro-optic modulator (EOM), driven by an electrical pulse generator (EPG). The pulses are then amplified by EDFAs operating in strong saturation, so that the output pulse peak power can be of a few tens of watts [116], [117]. The BPFs have a 3 dB bandwidth of 3.5 nm and are centered at the pump wavelength to reduce the ASE noise from the EDFAs. Finally, the variable optical attenuator (VOA) controls the pump power level and the FPC1 fixes the pump SOP entering the loop through the 50/50 OCo1.

The loop, shown at the bottom, comprises a nonlinear fiber, in which the nonlinear amplification processes take place, and a dispersion-compensating fiber (DCF), which provide the high dispersion required for the TDT.

The nonlinear fiber is a spool of 500 m of dispersion-shifted fiber (DSF). The average ZDW is around $\lambda_0 \approx 1548$ nm and the chromatic dispersion slope, defined in Eq. (3.14), is $S_0 = 0.05\,\mathrm{ps\,nm^{-2}\,km^{-1}}$. The measured nonlinear coefficients is $\gamma \simeq 2\,\mathrm{W^{-1}\,km^{-1}}$, whereas the measured Raman gain coefficient is $g_\mathrm{R} \simeq 1.2\,\mathrm{W^{-1}\,km^{-1}}$, which agrees quite well with the prediction [57]–[59] of Eq. (2.14). The SBS is not an issue here due to the short length of the fiber and relatively large bandwidth of the pulses. Upon comparison of the SBS threshold for the 26 km fiber presented in Section 3.1.2, here the threshold can be roughly estimated to be more than 30 dB higher.

Beyond the amplification stage given by the DSF, 10% of the power is directed to the output, while the remaining 90% is fed back into the loop through a 2 km long DCF. The DCF has a chromatic dispersion coefficient at $\lambda = 1550$ nm of $D_c = -103\,\mathrm{ps/nm/km}$ and a chromatic dispersion slope of $S_0 = -0.2024\,\mathrm{ps\,nm^{-2}\,km^{-1}}$. Finally, the FPC2 controls the alignment of the SOP of the circulating signal with respect to that of the input pump.

The total losses of the loop at $\lambda = 1550$ nm are about $\alpha_\mathrm{loop} = 8.6$ dB, whereas the single-pass gain of the loop can be expressed as:

$$G_\mathrm{loop}(\lambda) = \frac{1}{L}\int_0^L G(z,\lambda)\,\mathrm{d}z\,, \tag{3.19}$$

where $G(z,\lambda)$ depends on the particular amplification process and therefore on the wavelength. In particular, the dependence on the wavelength is also imposed by the TDT synchronization. The oscillation condition can then be written as:

$$G_\mathrm{loop} = \alpha_\mathrm{loop}\,. \tag{3.20}$$

3.3.2 Amplification regions

Fig. 3.6 shows the open-loop ASE from the DSF pumped by 10 W input peak power pulses (corresponding to 26 mW average power), for two different pump wavelengths $\lambda_{p1} = 1548.50$ nm (solid curve) and $\lambda_{p2} = 1547.50$ nm (dashed curve).

[1]Currently, fast tunable lasers can have a sweep rate on the order of few $\mathrm{nm\,ms^{-1}}$ over a band of few tens of nanometers.

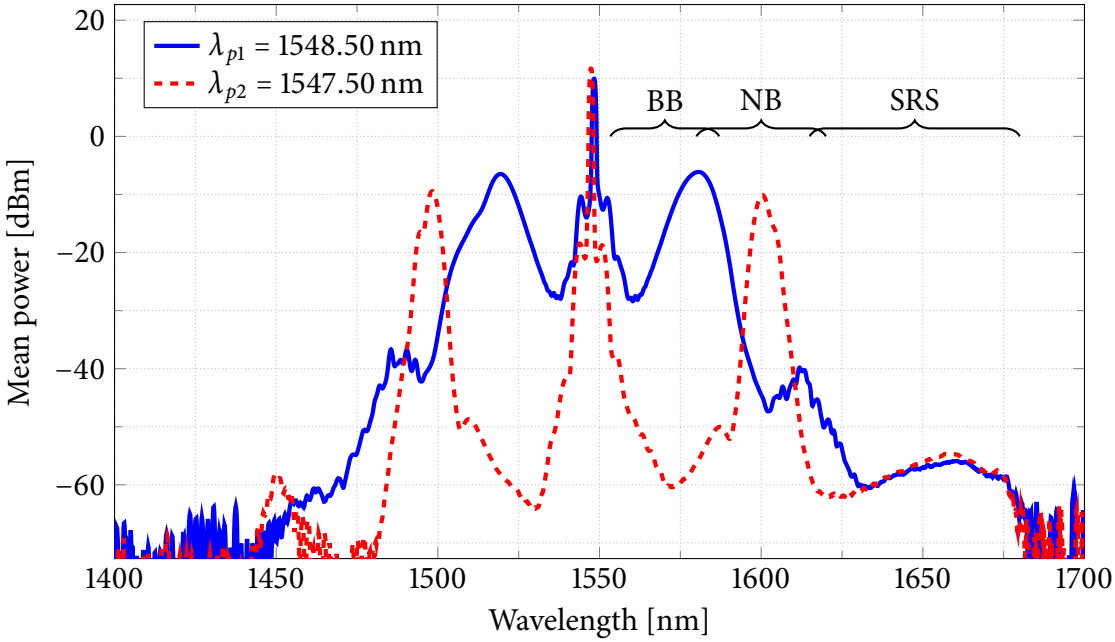

Figure 3.6: Amplified spontaneous emission of a 500 m long DSF obtained by pumping with 10 W of peak power in the anomalous dispersion regime at λ_{p1} = 1548.50 nm (blue solid curve) and in the normal dispersion regime at λ_{p2} = 1547.50 nm (blue dashed curve). Reprinted from [P.1] © 2013 OSA.

The latter pump wavelength (λ_{p2}) lays in the normal dispersion regime and gives rise to narrow-band fiber optical parametric amplification (NBFOPA) [64], [66], while the former wavelength (λ_{p1}) is in the anomalous dispersion regime in which BBFOPA appears [65]. The pumping wavelengths have been selected to enable an almost continuous transition between the three different regimes, *i.e.* depending on the particular process selected, the pump wavelength is set above or below the ZDW.

As explained in Section 2.3.2, in the NBFOPA regime (dashed curve in Fig. 3.6), due to phase matching conditions, there are two narrow gain regions well detuned from the pump [64], [66], which, in principle, with appropriate fiber characteristics, could be extended well above 2000 nm and below 1300 nm [68], [69]. The presence of two local maxima in the gain spectrum (λ = 1587 nm for the Stokes and its respective symmetric peak for the anti-Stokes) can be attributed to the variations of the ZDW along the fiber [70]. However, these peaks are 30 dB lower than the maximum.

On the contrary, BBFOPA regime is found for signal wavelengths around the pump wavelength [65], as seen in Section 2.3.1.

In both regimes the spontaneous emission due to SRS is observable in the wavelength range from 1625 nm up to 1675 nm. In fact, the gain peak of SRS is upshifted with respect to the pump wavelength of about 105 nm, and has a bandwidth of about 50 nm [56]. In the NBFOPA regime, the peak at about 1450 nm can be attributed to four-wave mixing (FWM) between the pump and the Raman ASE.

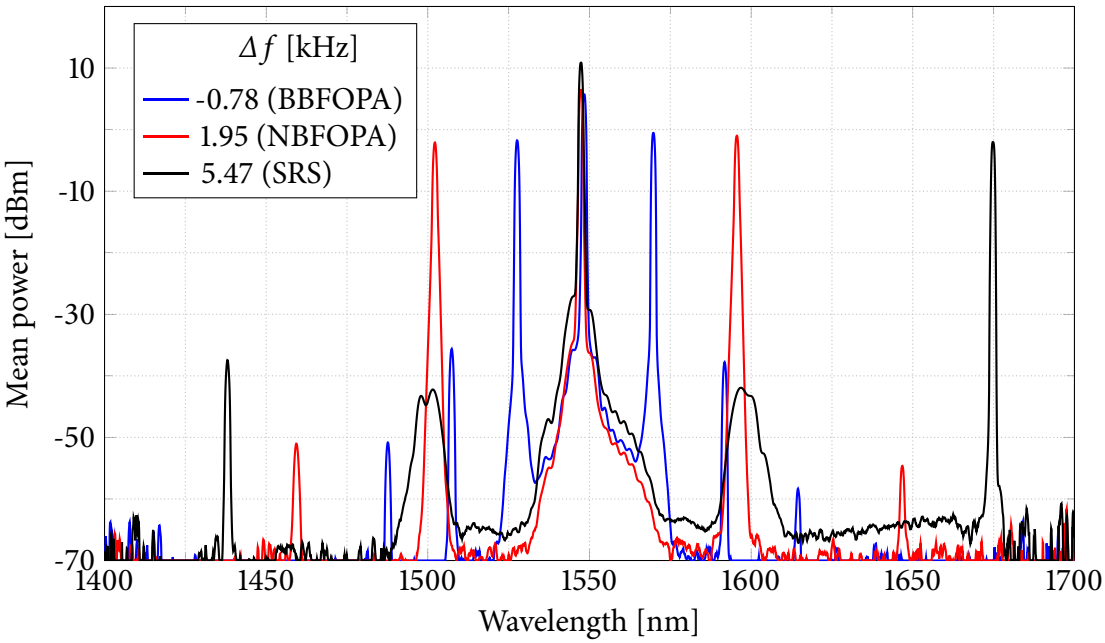

Figure 3.7: Spectra of the widely tunable fiber laser in the three different amplification regimes. The pump pulse repetition rate is $f_p = 2.3079\,\text{MHz}$.

3.3.3 Tuning and efficiency

As explained in Section 3.2, TDT enables to lock the oscillator to a predetermined wavelength. In this way each different nonlinear amplification process can be selected, therefore enhancing the tuning range but maintaining a good spectral purity.

Fig. 3.7 shows the spectra obtained by synchronizing the signal on particular wavelengths through the TDT technique. The pump pulse repetition rate is $f_p = 2.3079\,\text{MHz}$. The blue curve is obtained in the BBFOPA regime by shifting the repetition rate by $\Delta f = -0.78\,\text{kHz}$, whereas the red curve is obtained in the NBFOPA regime for $\Delta f = 1.95\,\text{kHz}$. The black curve, instead, is given by SRS amplification for $\Delta f = 5.47\,\text{kHz}$. For the BBFOPA and NBFOPA regimes the Stokes and the anti-Stokes waves have the same output power, whereas for SRS the Stokes wave is more intense because of the asymmetry of the Raman gain [118]–[120]. Moreover, in SRS regime a residual NBFOPA emission around 1500 nm and 1600 nm can be observed, because of its high efficiency. However, due to TDT, any unwanted emission is very weak (about 40 dB lower). In both the NBFOPA and the BBFOPA a higher harmonic peak is observed as a result of CFWM. This effect will be enhanced in Section 3.4 to realize a fast tunable OFC.

The tuning characteristic of the fiber laser is shown in Fig. 3.8, and, as it can be seen, the tuning range is about 160 nm. When the signal wavelength synchronized with the new incoming pump pulse was set beyond 1680 nm the laser went below threshold due to the fading of SRS.

The regime dominated by BBFOPA is indicated by the blue plus markers while that dominated by the SRS is indicated by red circle markers. The smooth transition between the two regimes, with an overlap ranging from 1580 nm to 1588 nm, is obtained through the NBFOPA.

The slope of the fitting (dashed) line is $S_\lambda = 22.65\,\text{nm}\,\text{kHz}^{-1}$; assuming a group in-

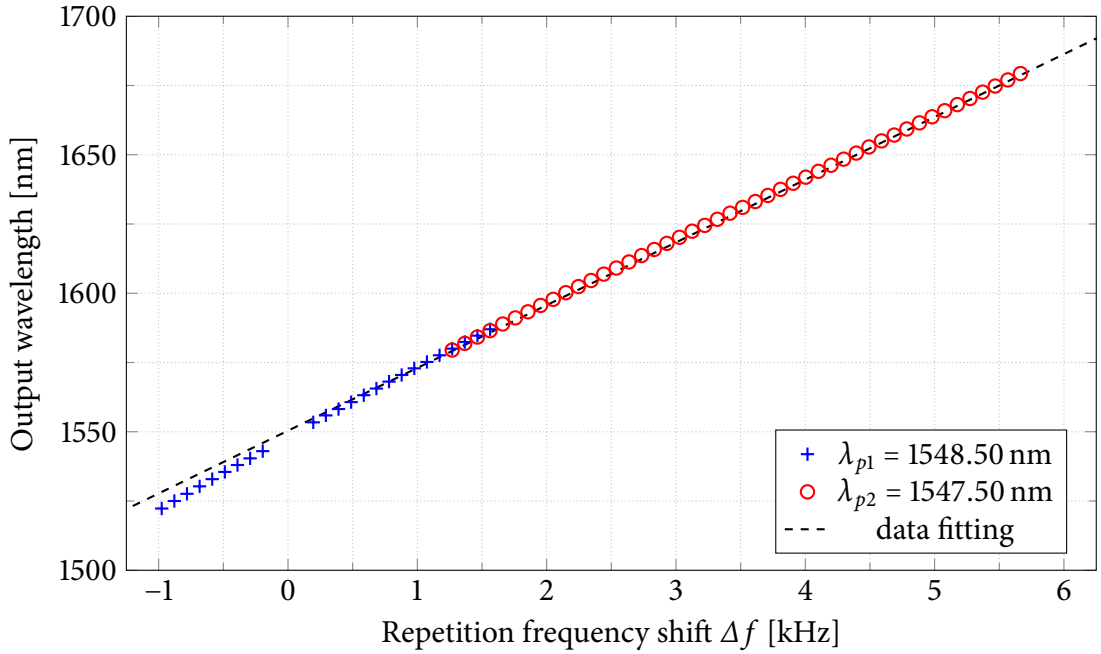

Figure 3.8: Tuning characteristic of the widely tunable fiber laser as a function of the shift $\Delta f = f - f_p$ of the pump pulse repetition rate ($f_p = 2.3079\,\mathrm{MHz}$). The blue plus markers refer to pumping in the anomalous dispersion regime, whereas red circle markers refer to pumping in the normal dispersion regime. Reprinted from [P.1] © 2013 OSA.

dex $n_g = 1.46$, the theoretical formula of Eq. (3.18) yields $S_\lambda = 23.43\,\mathrm{nm\,kHz^{-1}}$, which is in good agreement with experimental data. The slight deviation from the theoretical slope for $-1 \le \Delta f \le 0$ might be attributed to higher order dispersion effects.

The sweep velocity is set by the time delay in the cavity. In fact any change in the lasing wavelength becomes effective after the pulses have circulated enough times in the cavity in order to satisfy Eq. (3.20). In [113] a sweep rate of 40 kHz has been achieved with a cavity long 350 m. Here, the cavity is 2.5 km long, and therefore the sweep rate can be estimated to be about 5.6 kHz. However, the tuning range is larger than that achieved in [113].

The limiting factor in the sweep rate is the cavity length. This could be improved by using a shorter gain fiber, such as a highly nonlinear fiber (HNLF). HNLFs can have a larger nonlinear coefficient, *e.g.* $\gamma \approx 20\,\mathrm{W^{-1}\,km^{-1}}$, permitting to reduce the length of the fiber and consequently to increase the rate by a factor of 10. Similarly, the DCF could be shortened by increasing its dispersion properties.

The conversion efficiency of the fiber laser, defined as:

$$\eta = \frac{P^{\mathrm{out}}_{s,\mathrm{avg}}}{P^{\mathrm{in}}_{p,\mathrm{avg}}}\,, \tag{3.21}$$

where $P^{\mathrm{out}}_{s,\mathrm{avg}}$ is the average power of the oscillating signal and $P^{\mathrm{in}}_{p,\mathrm{avg}}$ is the average input power of the pump, is shown in Fig. 3.9. The average efficiency is about $\eta = 5\%$ and the laser threshold mean power ranged from about 2.5 mW to about 15 mW. The maximum efficiency is $\eta = 16\%$, obtained in the BBFOPA regime. The variations of the efficiency in this regime are compatible to those of the ASE shown in Fig. 3.6. For the NBFOPA, the maximum efficiency is about $\eta = 8\%$. The transition from the NBFOPA to the SRS regime

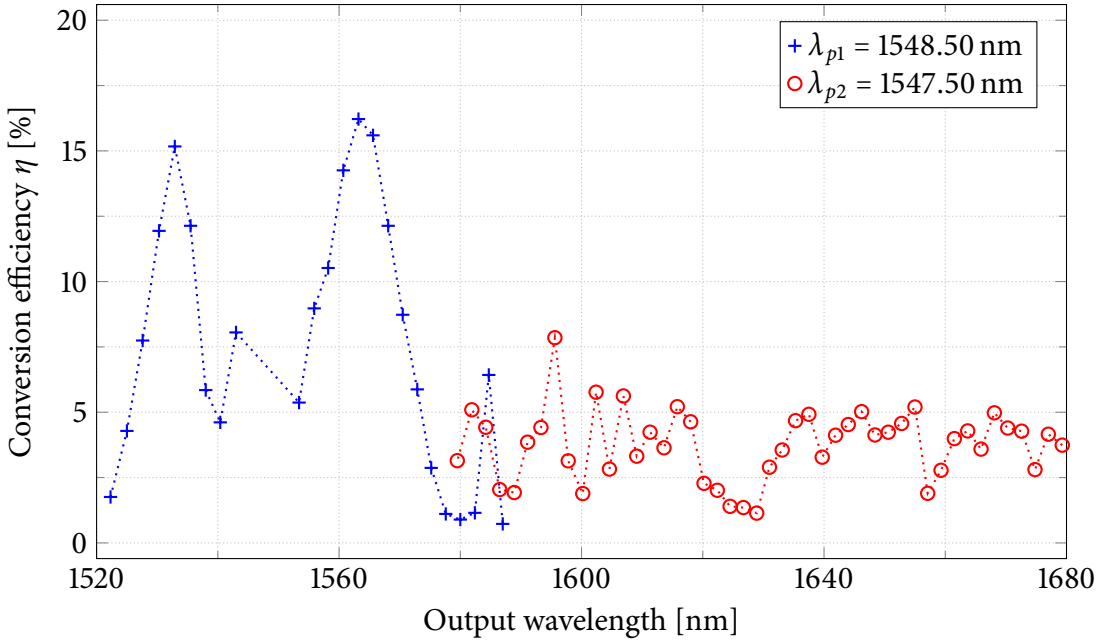

Figure 3.9: Efficiency of the widely tunable fiber laser as a function of the output wavelength. The blue plus markers refer to pumping in the anomalous dispersion regime, whereas red circle markers refer to pumping in the normal dispersion regime. Reprinted from [P.1] © 2013 OSA.

can be identified by a drop of the efficiency at about 1625 nm. The SRS regime results in lower efficiency due to the smaller gain coefficient (see Eq. (2.14)).

As it can be seen, the efficiency is not flat because it depends on the spectral efficiency of the particular regime. If constant output power is required, then an automatic feedback control could be implemented for example. However, such control would set a limitation in the sweep velocity. On the other hand, in many applications flat output is not an issue [4]. For instance, in measurements based on insertion losses or on back-reflections, typically what is measured is the relative difference with respect to a referenced spectrum.

Finally, Fig. 3.10 shows the spectra of Fig. 3.7 and for some other oscillation wavelengths reported in Fig. 3.8. The dashed line is the tuning characteristic. The residual NBFOPA emission around 1500 nm and 1600 nm is clearly observable in four traces (Δf = 2.83 kHz, 3.71 kHz, 4.58 kHz and 5.46 kHz), and no residual SRS emission is clearly visible. TDT in conjunction with NBFOPA was partially exploited in [68]; however, tuning was realized by modifying the pump wavelength and a thulium-doped fiber (TDF) had to be used to eliminate unwanted SRS radiation [68], [69]. Here, on the contrary, TDT enables to suppress unwanted oscillations down to −40 dB with respect to the tuned spectral line. In all the measures the signal linewidth is below 0.05 nm (limited by the resolution of the OSA).

As already noted in Fig. 3.7, higher harmonic peaks due to CFWM are observed in three traces (for Δf = −0.78 kHz, 1.17 kHz and 1.95 kHz). This effect will be enhanced in the following Section 3.4 to realize a fast tunable OFC.

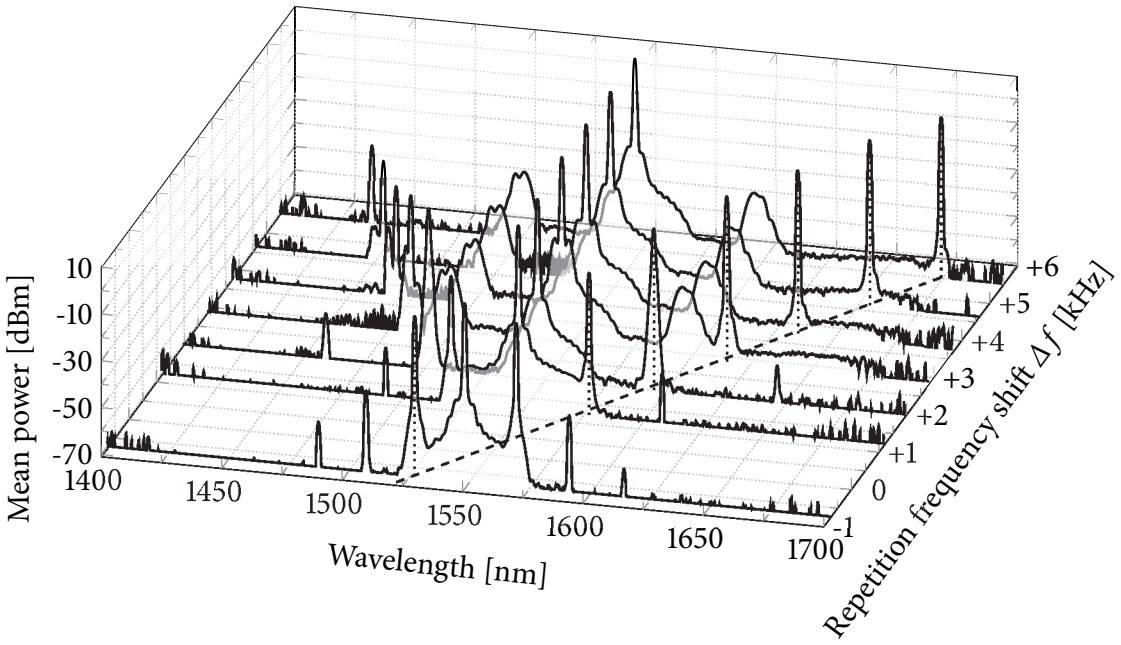

Figure 3.10: Spectra of the widely tunable fiber laser. The dashed line is the tuning characteristic presented in Fig. 3.8. For the sake of comprehension the traces have been truncated to −70 dBm. Reprinted from [P.1] © 2013 OSA.

3.4 Generation of fast tunable optical frequency combs

In Section 3.3 a widely tunable all-fiber oscillator has been presented. The oscillator, through TDT is able to generate oscillations on different regimes, in particular using the BBFOPA process. Moreover, it has also been shown that in the BBFOPA regime a CFWM process can appear. This section, based on the publication [P.1], shows that the same TDT technique used in Section 3.3 can be successfully applied to achieve tunable optical frequency combs (OFCs) through CFWM.

3.4.1 Optical frequency combs

Ideally, OFCs are optical sources whose spectrum $F(f)$ is a series of delta functions that can be described by

$$F(f) = A_0 \sum_{k=-\infty}^{+\infty} \delta(f - k\Delta f - f_0) \tag{3.22}$$

where Δf is the comb tooth spacing, A_0 is an arbitrary amplitude and $f_0 < \Delta f$ is a constant offset. In particular, in the time domain it corresponds to a periodic signal with period $\Delta T = 1/\Delta f$.

Recently, OFCs have been gathering conspicuous attention because they are key components in several applications in communication [7], signal processing [8], metrology [9], [10] and spectroscopy [10], [11]. The key characteristics of an OFC can include [121], [122]:

- frequency separation,
- power equalization,

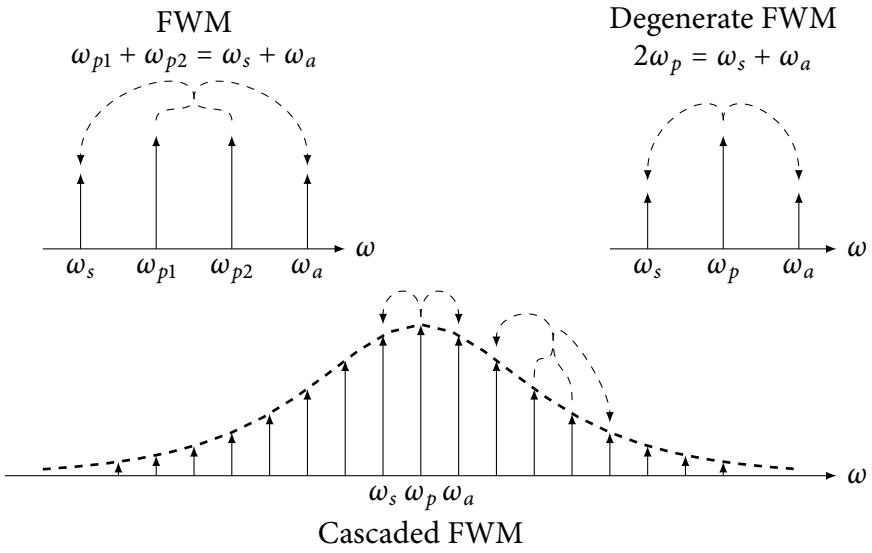

Figure 3.11: Cascaded four-wave mixing for OFC generation.

- spectral purity,
- phase locking and orthogonality (needed for some coherent applications like orthogonal frequency division multiplexing),
- tunability across a given spectral region,
- long term stability,
- and locking to an absolute frequency reference.

Currently, no OFC provides all these characteristics simultaneously [122].

The most straightforward OFCs are bulk mode-locked lasers [123] which are extremely accurate devices, though large and cumbersome. More compact solutions that have appeared are monolithic semiconductor mode-locked lasers [124], [125], or optical parametric oscillators based on high Q-factor monolithic resonators [126] like microtoroids [127], [128], silica microspheres [129], silicon [130] or silicon nitride microrings [131], [132]. Monolithic cavities can attain high spectral purity but their main drawback is that the comb frequency spacing is often fixed by the cavity properties. They can, however, be tuned by modifying the cavity through thermal effects [12], but the resulting tuning is slow.

In optical fibers, tunable OFCs can be easily achieved through CFWM [133], [134], which, as depicted in Fig. 3.11, can be viewed as a combination of degenerate and non-degenerate FWM processes. Typically such OFCs are realized either in a single-pass fiber amplifier in which two CW pump waves are injected [14], [15], or through a double stage amplifier exploiting phase-sensitive amplification [135], [136]. Those setups are very simple, but OFC spectral purity is strongly influenced by the pumps frequency and phase stability [16]. In fact, the main advantage of CFWM-based combs (the constant frequency spacing between comb teeth) is lost unless a feedback error signal is used to stabilize both the pump lasers [137].

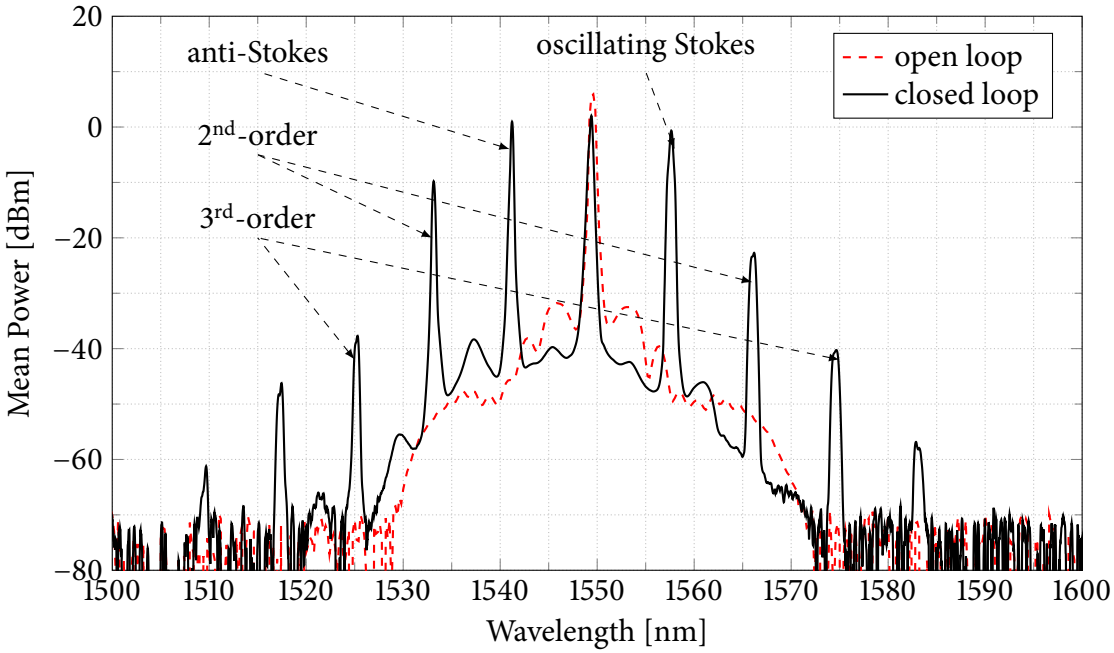

Figure 3.12: CFWM establishment (black solid curve) obtained by pumping in the BBFOPA regime at $\lambda_p = 1549.50$ nm and by setting the resonating wavelength at a distance of 8.25 nm from the pump wavelength. The red dashed curve is the relative ASE spectrum. In both cases the pump peak power is $P_p = 3.29$ W.

Also in Fabry-Pérot resonators [138] SBS limits the spectral purity. The use of doubly pumped ring cavities prevents the growth of Brillouin oscillations [139], but still presents limitations in the frequency stability. To circumvent that problem a singly pumped cavity [13] has been very recently realized, but the comb teeth tuning has been realized by intracavity tunable filters, so limiting the comb reconfiguration time.

3.4.2 Results

As discussed above, OFCs can be obtained through CFWM. Moreover, in the spectra of Fig. 3.10 it has been shown that in the BBFOPA regime a CFWM process can appear.

Fig. 3.12 shows the spectrum (black solid curve) obtained by using the same setup of Section 3.3. The pump is in the BBFOPA regime, at $\lambda_p = 1549.50$ nm, and the synchronously pumped wavelength is selected to be very close to the pump wavelength ($\Delta\lambda = 8.25$ nm). In this case an efficient CFWM occurs and an OFC is obtained.

In particular, here the resonant wavelength is properly synchronized through TDT. Therefore, the OFC is obtained in a singly pumped fiber CFWM resonator. This fact can avoid the limitations in spectral purity and frequency and phase stability given by double pump systems.

The comb teeth linewidth at −3 dB is at most 0.35 nm. The broad linewidth can be attributed to the fluctuations of dispersion parameters of the cavity, *e.g.* variations of the ZDW along the fiber [70]. Moreover, the output pulses are chirped by cross-phase modulation (XPM). The resulting frequency broadening $\delta\omega$ can be roughly estimated by considering Gaussian pulses of duration $T_0 = 1$ ns and by noting that the lines have

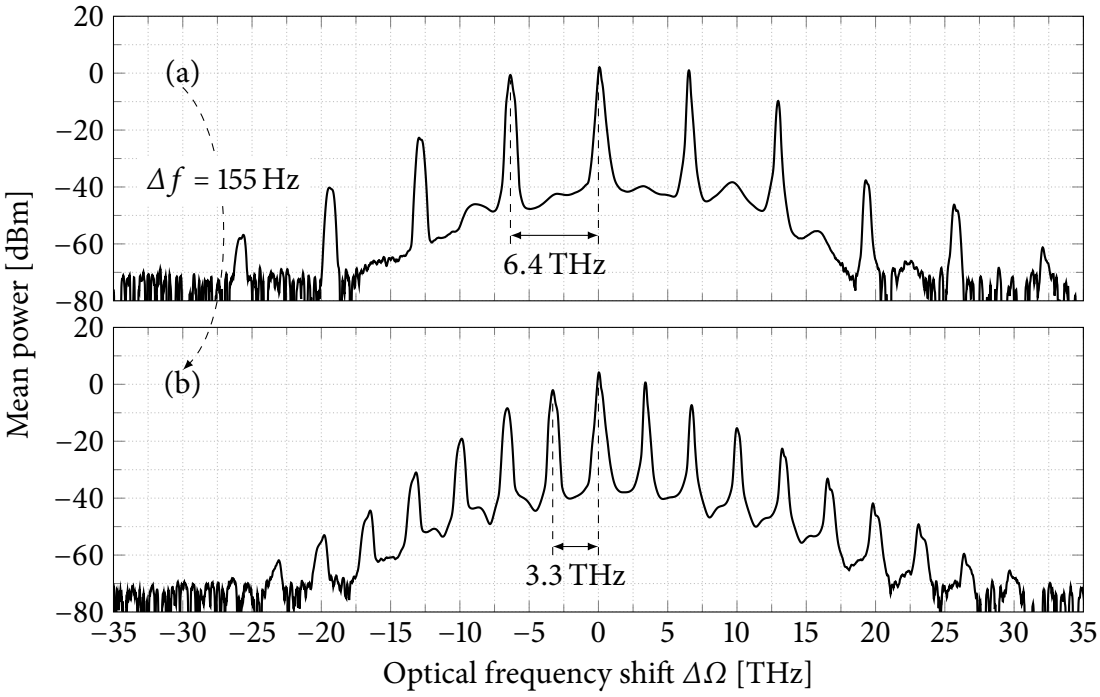

Figure 3.13: Spectra of the tunable OFC for two different synchronously pumped wavelengths. The repetition frequency shift between the two configurations is $\Delta f = 0.135\,\text{kHz}$. The pump is set at $\lambda_p = 1549.50\,\text{nm}$ with 3.29 W peak power. Reprinted from [P.1] © 2013 OSA.

similar power. Therefore the XPM broadening is in the order of two times the self-phase modulation (SPM) broadening [50], yielding approximately:

$$\delta\omega \approx 4\gamma P_p L T_0^{-1} \approx 0.32\,\text{nm}\,, \tag{3.23}$$

which is very close to the observed value.

Remarkably, by modifying the resonating wavelength, tuning of the OFC teeth spacing can be obtained. This is shown in Fig. 3.13, where two different frequency spacing $\Delta\Omega$ and different numbers of Stokes waves have been obtained ((a) $\Delta\Omega = 6.4\,\text{THz}$ and 4 Stokes waves; (b) $\Delta\Omega = 3.3\,\text{THz}$ and 7 Stokes waves).

For the DSF used in the experiments, BBFOPA gain drops significantly for pump-signal frequency detunings smaller than 2.3 THz; so, no OFC formation has been observed below such value. Regarding the OFC properties, though no time characterization could be performed due to the lack of an autocorrelator, the coherence between comb teeth is assured by the CFWM and the fact that a single pump is injected, differently from [15].

The first remarkable property of the obtained OFC is the possibility of very fast tuning. The second is that the obtained high frequency modulation $\Delta\Omega$ is linked directly to a low frequency f electrical signal through

$$\Delta\Omega \simeq \frac{\Delta f}{\beta_2(\omega_p) f_p v_g(\omega_p)}\,. \qquad \text{(Eq. (3.17) revisited.)}$$

Therefore $\Delta\Omega$ can be locked to microwave frequency standards, enabling frequency up-conversion for example.

3.5 Conclusions

In this chapter all-fiber optical sources through nonlinear amplification processes have been presented and characterized.

First, in Section 3.1, a continuous-wave pump has been presented. That pump, aimed to be used in fiber Raman amplifiers, enables to reduce the pump depletion induced by stimulated Brillouin scattering.

Then, a widely tunable fiber optical oscillator has been presented in Section 3.3. Such oscillator, based on three nonlinear processes, namely stimulated Raman scattering, broad-band and narrow-band optical parametric amplification, uses the time-dispersion-tuning technique both for tuning the output wavelength and for suppressing unwanted radiation. The achieved laser is tunable over a range of 160 nm, smoothly passing through the three processes, with only one change in the pump wavelength. Therefore the oscillator wavelength reconfiguration time, for the largest section of the spectrum (about 100 nm), is only set by the achievable speed of change of the pump pulse repetition rate, which can be extremely high. Moreover, the tuning range could be further extended by properly designing fiber dispersion. The efficiency, limited to 16%, and the limits on the sweep velocity have been discussed, together with possible solutions.

Finally, in Section 3.4 through the same technique a fast tunable optical frequency comb has been realized exploiting cascaded four-wave mixing. The optical frequency comb is obtained in a singly pumped fiber CFWM resonator, therefore avoiding some of the limitations in spectral purity and stability given by double pump systems. The most valuable features of the generated comb are that the frequency spacing may be quickly tuned without modifying the teeth bandwidth, which can be a useful property in applications like orthogonal frequency division multiplexing. Furthermore, such optical frequency comb at very high frequency can be locked directly to a microwave frequency standard.

Chapter 4

Nonlinear polarization attraction in fiber Raman amplifiers

$$\boldsymbol{pq} - \boldsymbol{qp} = \frac{h}{2\pi \mathrm{i}}$$

Werner Karl Heisenberg
1901 – 1976

This chapter deals with nonlinear polarization attraction (NPA) in counter-propagating fiber Raman amplifiers (FRAs) in standard, randomly birefringent, single-mode fibers (SMFs). Over the past few years, NPA has been proposed as an effective method to optically control the state of polarization (SOP) of signals. Nonlinear polarization attraction in FRAs is driven by the polarization-dependent nature of the Raman effect, and it enables the attraction of the SOP of a signal toward a SOP set by the pump. In particular, due to the attraction process a depolarized signal experiences an increase of its degree of polarization (DOP).

After a short introduction on the state of the art given in the following Section 4.1, in Section 4.2 a vector model for stimulated Raman scattering (SRS) will be briefly reviewed. Then, in Section 4.3 a full-scale numerical analysis and statistical evaluations of NPA in counter-propagating FRAs in randomly birefringent SMFs are presented. The analysis includes the effects of pump depletion, nonlinear polarization rotation (NPR) and orthogonal Raman gain, and it shows that a counter-propagating FRA is effective in attracting the signal toward a predetermined SOP settled by the pump input SOP. Furthermore, it is shown that pump depletion plays an important role in achieving signal repolarization in fibers with moderately-high polarization-mode dispersion (PMD). Remarkably, it is predicted the existence of a quantitative relationship between the gain and the maximum DOP acquired by the signal in the amplifier. Finally, in Section 4.4, such relationship, which approximates both the performances and the limitations of the attraction efficiency, is experimentally validated, confirming that it represents an upper-bound on the maximum achievable DOP.

4.1 Introduction

Polarization is an important degree of freedom of light which is being increasingly exploited in optical communications and sensing systems, among others. Over the past few years, the all-optical processing of polarization has been the subject of considerable research efforts, giving rise to new devices able, for example, to perform polarization modulation and regeneration, or to control the SOP and the DOP. For instance, controlling the DOP permits to attain signal depolarization or repolarization.

SOP control can be attained by electronically driven waveplates or polarization controllers [140]–[146], but the speed of such systems is limited by the electronic feedback and the mechanical stages. Signal repolarization can be obtained by using classical bulk polarizers, which operate by projecting the SOPs over a predetermined direction. However, the average efficiency of such projection is physically limited to be lower than 50%. In 2000, Heebner *et al.* [17] demonstrated an all-optical repolarizer based on the photo-refractive effect and with efficiency higher than 50% [17]. This is a fundamental example of NPA, a process in which the SOP is attracted, rather than projected, to a predetermined direction, therefore increasing the limits on the efficiency. Since then, NPA has been proposed as an effective all-optical method to control the SOP. However, the photo-refractive effect used in [17] has severe limitations due to the low response time of the mediating material.

Only recently, the nonlinear Raman amplification process has been demonstrated as an effective method to obtain NPA in standard telecommunications SMFs [P.2], [18]–[30], [C.2], [P.3]. NPA in SMFs can be achieved also by exploiting stimulated Brillouin scattering (SBS) [31]–[34] or Kerr nonlinearity [30], [35]–[45], and, depending on the actual configuration, some of the three effects may act together [30], [35]. These processes have response time in the order of femtoseconds, enabling virtually instantaneous control of the SOP.

In FRAs the NPA is driven by the polarization-dependent nature of SRS which causes the component of the signal parallel to the pump to experience higher Raman gain than the orthogonal component. This process cumulates along the fiber and permits the attraction of the SOP of the signal toward a SOP set by the pump. In particular, if the pump is polarized, a depolarized signal experiences an increase of the DOP due to the attraction process, and, therefore, such a device is also called a Raman polarizer (RP) [29], [147].

The main advantage of using FRAs to achieve NPA is, together with the fast response time of SRS, the possibility of achieving simultaneously both amplification and repolarization over a band of more than 7 THz [25]. It has been also very recently demonstrated the possibility to apply Raman-based NPA to realize RPs in integrated silicon devices [27], to obtain repolarization in wavelength-division-multiplexing (WDM) systems [26] or to enhance the performances of FRAs [28].

Under proper circumstances, co-propagating FRAs can achieve high signal repolarization efficiency. However, they suffer of some disadvantages with respect to the counter-propagating configuration, such as the higher relative intensity noise (RIN) transfer between pump and signal [52], [148]; but the main problem arise from the unpredictability of the output SOP [20], [22]. On the contrary, in a counter-propagating scheme the signal output SOP is fully determined by the pump input SOP, thus overcoming such unpredictability [24], [33], [P.3].

The following analysis is therefore focused on FRAs in counter-propagating configuration. Moreover, only the case of continuous-wave (CW) signals is considered, which,

however, provides a good approximation of the steady-state behavior of high bit-rate pulse streams [30].

4.2 Vector model of stimulated Raman scattering

The scalar model of SRS briefly reviewed in Section 2.2 is limited to the case of co-polarized beams, *i.e.* a case in which both the pump and the signal maintain exactly the same SOP during all their interaction. In order to deal with signals with arbitrary SOPs and to study their polarization properties it is therefore necessary to introduce a vector model in which the pump and the signal can have arbitrary and, in general, different SOPs.

By using the model developed by Lin and Agrawal [149], the pump and the signal can be described by fully polarized CW signals, *i.e.* monochromatic waves having unitary DOP. Their arbitrary SOPs are represented by three-components Stokes vectors of the form:

$$\boldsymbol{S} = \begin{pmatrix} S_1 \\ S_2 \\ S_3 \end{pmatrix} = S_0 \hat{\boldsymbol{s}} = S_0 \begin{pmatrix} s_1 \\ s_2 \\ s_3 \end{pmatrix} . \tag{4.1}$$

Therefore this representation slightly simplifies the full four-components representation of the Stokes vectors, which is discussed in Appendix A. In particular, there is no unpolarized component of the beam and the power is simply given by

$$S_0 = \|\boldsymbol{S}\| = \sqrt{S_1^2 + S_2^2 + S_3^2} . \tag{4.2}$$

The interaction of the signal $\boldsymbol{S}$ and of the backward propagating pump $\boldsymbol{P}$ is described by the following two coupled equations [19], [149]:

$$\frac{\mathrm{d}\boldsymbol{S}}{\mathrm{d}z} = -\alpha_s \boldsymbol{S} + \frac{g_\mathrm{R}}{2}\Big[P_0 \boldsymbol{S} + S_0 \boldsymbol{P} + \mu\big(3P_0 \boldsymbol{S} + S_0 \boldsymbol{P} - 2S_0 \boldsymbol{P}_3\big)\Big] + \big(\omega_s \boldsymbol{b} + \boldsymbol{W}_s\big) \times \boldsymbol{S} , \tag{4.3a}$$

$$\frac{\mathrm{d}\boldsymbol{P}}{\mathrm{d}z} = \alpha_p \boldsymbol{P} + \frac{\omega_p}{\omega_s}\frac{g_\mathrm{R}}{2}\Big[S_0 \boldsymbol{P} + P_0 \boldsymbol{S} + \mu\big(3S_0 \boldsymbol{P} + P_0 \boldsymbol{S} - 2P_0 \boldsymbol{S}_3\big)\Big] - \big(\boldsymbol{M}\omega_p \boldsymbol{b} + \boldsymbol{W}_p\big) \times \boldsymbol{P} , \tag{4.3b}$$

where, as previously defined in Eq. (4.2), $P_0 = \|\boldsymbol{P}\|$ and $S_0 = \|\boldsymbol{S}\|$ represent, respectively, the powers of the pump and of the signal. The vectors $\boldsymbol{P}_3$ and $\boldsymbol{S}_3$ are defined as

$$\boldsymbol{P}_3 = P_3 \hat{\boldsymbol{e}}_3 = \begin{pmatrix} 0 \\ 0 \\ P_3 \end{pmatrix} \qquad \text{and} \qquad \boldsymbol{S}_3 = S_3 \hat{\boldsymbol{e}}_3 = \begin{pmatrix} 0 \\ 0 \\ S_3 \end{pmatrix} , \tag{4.4}$$

where $\hat{\boldsymbol{e}}_3 = (0, 0, 1)^T$ is the unit vector representing right-handed circular polarization. The angular frequencies of the pump and of the signal are, respectively, ω_p and ω_s; α_p and α_s are the attenuation coefficients at the respective frequencies.

The coefficient g_R in Eqs. 4.3 is the value of the Raman gain coefficient at the frequency of the signal ω_s. As explained in Section 2.2, for silica fibers the peak of the Raman gain is downshifted from the frequency of the pump ω_p by $\Omega_\mathrm{R} = 2\pi f_\mathrm{R}$, where $f_\mathrm{R} = 13.2\,\mathrm{THz}$. Therefore the corresponding frequency for the signal is $\omega_s = \omega_p - \Omega_\mathrm{R}$. In the pump equation Eq. (4.3b) g_R is scaled by the term ω_p/ω_s which account for the different energies of photons at the frequency of the signal and of the pump; the rest of the energy is absorbed by the medium.

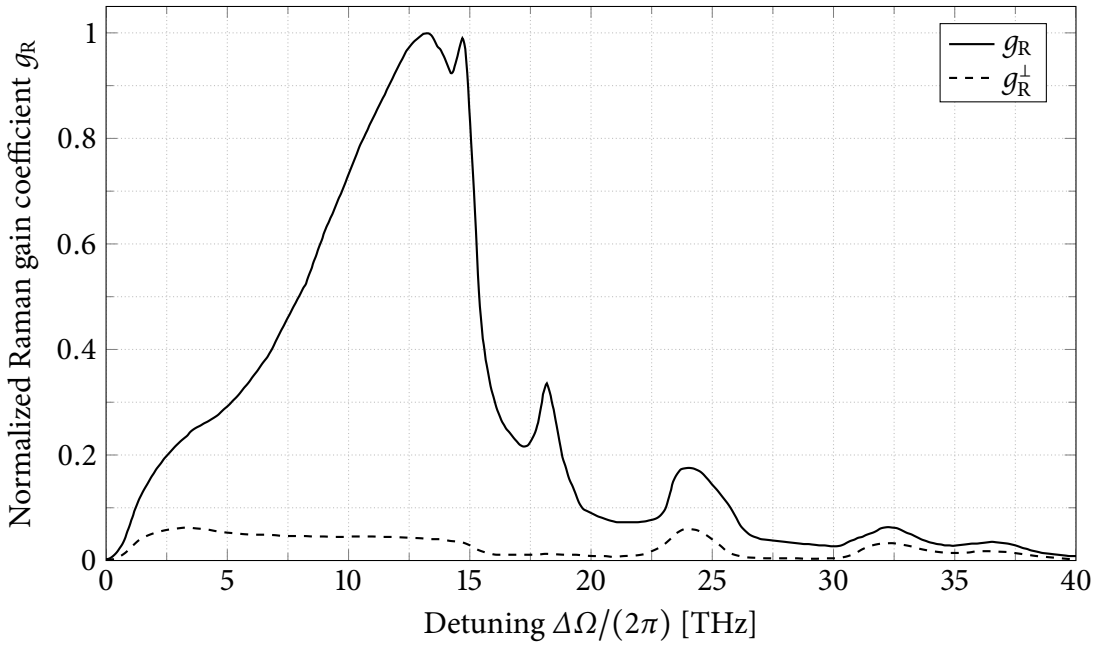

Figure 4.1: Normalized parallel g_R (solid) and orthogonal $g_R^\perp$ (dashed) Raman gain coefficients of silica fibers as a function of the pump-signal detuning $\Delta\Omega/(2\pi)$. The frequency shift of the peak is about 13.2 THz. Reprinted from [50] © 2007 Elsevier.

The scalar model of Section 2.2 is augmented by differentiating between the gain exerted on the parallel and on the orthogonal components of the signal with respect to the pump. Fig. 4.1 shows the parallel g_R and the orthogonal $g_R^\perp$ Raman gain coefficients for silica fibers. As it can be seen, the gain induced on the component of the signal orthogonal to the pump is much smaller than that on the parallel. The coefficient μ in Eqs. 4.3, also called the depolarization ratio, is the ratio between the orthogonal and parallel Raman gain coefficients:

$$\mu = \frac{g_R^\perp}{g_R}. \tag{4.5}$$

For silica fibers, an accepted value of the depolarization ratio of the Raman peak is $\mu = 0.012$ [149], [150]. Near the peak, μ is generally lower than 0.05 [151].

The vectors $\boldsymbol{W}_p$ and $\boldsymbol{W}_s$ in Eqs. 4.3 take into account for the NPR and are given by

$$\boldsymbol{W}_p = \frac{2}{3}\left[\gamma_{pp}\boldsymbol{P}_3 + 2\gamma_{ps}(1+\delta_b)\boldsymbol{S}_3 - \gamma_{ps}(2+\delta_a+\delta_b)\boldsymbol{S}\right], \tag{4.6a}$$

$$\boldsymbol{W}_s = \frac{2}{3}\left[\gamma_{ss}\boldsymbol{S}_3 + 2\gamma_{sp}(1+\delta_b)\boldsymbol{P}_3 - \gamma_{sp}(2+\delta_a+\delta_b)\boldsymbol{P}\right]. \tag{4.6b}$$

The terms comprising γ_{pp} and γ_{ss} are the self-phase modulation (SPM)-induced NPR, whereas those associated with γ_{ps} and γ_{sp} describe the cross-phase modulation (XPM)-induced NPR; the parameters δ_a and δ_b are related to the delayed nonlinear Raman response [149], [152], [153].

The vectors $\omega_p\boldsymbol{b}$ and $\omega_s\boldsymbol{b}$ describe the birefringence of the fiber at the frequency ω_p

and ω_s, respectively; the matrix $\boldsymbol{M}$ in Eq. (4.3b) is given by Galtarossa *et al.* [19]:

$$\boldsymbol{M} = \begin{pmatrix} 1 & 0 & 0 \\ 0 & 1 & 0 \\ 0 & 0 & -1 \end{pmatrix}. \tag{4.7}$$

Actually, $\boldsymbol{M}$ accounts for the fact that $\boldsymbol{P}$ is backward-propagating with respect to the signal [19], which has not been considered in the original model of Lin and Agrawal [149].

Finally, for a fiber of length L, the system of Eqs. 4.3 is constrained by the following two boundary conditions:

$$\boldsymbol{S}(z = 0) = \boldsymbol{S}^{\text{in}}, \tag{4.8a}$$
$$\boldsymbol{P}(z = L) = \boldsymbol{P}^{\text{in}}, \tag{4.8b}$$

where $\boldsymbol{S}^{\text{in}}$ is the Stokes vector of the input signal at $z = 0$ and $\boldsymbol{P}^{\text{in}}$ is the input pump entering at the opposite end of the fiber at $z = L$.

4.3 Analysis and characterization

This section, based on the publications [P.3] and [C.2], reports the analysis obtained by numerically solving the system Eqs. 4.3 and by performing statistical evaluations.

The parameters of the counter-propagating FRAs are defined as follows. The wavelength of the signal is set in the C band at $\lambda_s = 1550\,\text{nm}$. Consequently its angular frequency is $\omega_s = 2\pi c/\lambda_s$ with c being the speed of light in vacuum. The frequency of the pump is $\omega_p = \omega_s + \Omega_{\text{R}}$ by $\Omega_{\text{R}} = 2\pi f_{\text{R}}$, $f_{\text{R}} = 13.2\,\text{THz}$, yielding $\lambda_p = 1451\,\text{nm}$. The attenuation coefficients for the signal and for the pump are, respectively, $\alpha_s = 0.200\,\text{dB km}^{-1}$ and $\alpha_p = 0.273\,\text{dB km}^{-1}$. The Raman gain coefficient at the signal frequency ω_s is $g_{\text{R}} = 0.60\,\text{W}^{-1}\,\text{km}^{-1}$ [19], [22], [33], [P.3], [52], [149], [154] and the depolarization ratio is $\mu = 0.0118$ [19], [22], [33], [P.3], [52], [149], [154].

For the purpose of the present analysis, the parameters δ_a and δ_b in Eqs. 4.6, related to the delayed nonlinear Raman response [149], [152], [153], can be neglected [149], [152]–[156]. Therefore $\delta_a = \delta_b = 0$ and Eqs. 4.6 can be simplified to

$$\boldsymbol{W}_p = \frac{2}{3}\left[\gamma_{pp}\boldsymbol{P}_3 + 2\gamma_{ps}(\boldsymbol{S}_3 - \boldsymbol{S})\right], \tag{4.9a}$$
$$\boldsymbol{W}_s = \frac{2}{3}\left[\gamma_{ss}\boldsymbol{S}_3 + 2\gamma_{sp}(\boldsymbol{P}_3 - \boldsymbol{P})\right], \tag{4.9b}$$

where the coefficients for the SPM- and for the XPM-induced NPR are $\gamma_{pp} = \gamma_{ps} = 1.24\,\text{W}^{-1}\,\text{km}^{-1}$ and $\gamma_{ss} = \gamma_{sp} = 1.06\,\text{W}^{-1}\,\text{km}^{-1}$, respectively.

As described in Appendix D, it can be reasonably assumed that standard SMFs do not present circular birefringence [157]–[161]. Therefore the random linear birefringence can be accounted by the vector

$$\boldsymbol{b} = \begin{pmatrix} b_1 \\ b_2 \\ 0 \end{pmatrix}, \tag{4.10}$$

which can be described by the random modulus model (RMM) [160] (see Appendix D.1). The PMD coefficient (PMDc) D_P at the signal frequency ω_s is given by

$$D_P = \frac{2\sqrt{2}\pi L_C}{\omega_s L_B \sqrt{L}} \left(\mathrm{e}^{-\frac{L}{L_C}} + \frac{L}{L_C} - 1 \right)^{\frac{1}{2}}, \tag{4.11}$$

where L_C and L_B are, respectively, the correlation and the beat lengths.

The nonlinear system of Eqs. 4.3 with the two boundary conditions given by Eqs. 4.8 is solved by a shooting algorithm [162], whereas the numerical integration is performed by a fourth-order Runge-Kutta (RK4) method, with a variable step size in the order of 10 mm and sufficient to follow the local birefringence variations. More details on the RK4 method and on the shooting technique can be found in Appendix E.

For a single fiber birefringence realization, the gain G and the DOP $\mathcal{D}$ of the output signal

$$\boldsymbol{S}^{\mathrm{out}} \stackrel{\mathrm{def}}{=} \boldsymbol{S}(z = L) \tag{4.12}$$

are defined as

$$G = \langle S_0^{\mathrm{out}} \rangle_{\mathrm{sops}} / S_0^{\mathrm{in}}, \tag{4.13a}$$

$$\mathcal{D} = \left\| \langle \boldsymbol{S}^{\mathrm{out}} \rangle_{\mathrm{sops}} \right\| / \langle S_0^{\mathrm{out}} \rangle_{\mathrm{sops}}, \tag{4.13b}$$

where the average $\langle \cdot \rangle_{\mathrm{sops}}$ is taken over 100 signal input random SOPs uniformly distributed on the Poincaré sphere. Eventually, the mean gain $\overline{G}$ and the mean DOP $\overline{\mathcal{D}}$ are estimated as

$$\overline{G} = \langle G \rangle_{\mathrm{fibers}}, \tag{4.14a}$$

$$\overline{\mathcal{D}} = \langle \mathcal{D} \rangle_{\mathrm{fibers}}, \tag{4.14b}$$

where the average $\langle \cdot \rangle_{\mathrm{fibers}}$ is taken over a large statistical ensemble of fiber birefringence realizations.

Fig. 4.2 shows various Poincaré spheres for the signal SOPs evolution along one fiber realization, with length $L = 2\,\mathrm{km}$ and PMDc $D_P = 0.05\,\mathrm{ps\,km^{-1/2}}$. The signal and the pump input powers are, respectively, $S_0^{\mathrm{in}} = 1\,\mathrm{mW}$ and $P_0^{\mathrm{in}} = 8\,\mathrm{W}$, and the pump input SOP is $\hat{\boldsymbol{p}}^{\mathrm{in}} = (1, 0, 0)^T$. Fig. 4.2(a) shows the initial configuration of the signal SOPs entering the fiber, where $\mathcal{D} = 0.01$ indicates a depolarized signal. As the signal propagates toward the input pump at $z = L$, both the gain G and the DOP $\mathcal{D}$ increase, as it can be seen in Fig. 4.2(b)–(f). The reduction of the spread of the SOPs indicates that the SOPs are attracted toward a common point. In fact, as it will be explained later, the SOPs are attracted toward the pump SOP. The pump SOP $\hat{\boldsymbol{p}}(z)$, however, evolves along the fiber due to the random birefringence. Only at $z = 2\,\mathrm{km}$, *i.e.* at the output of the fiber (Fig. 4.2(f)), the signal SOPs are clearly attracted toward the pump input SOP $\hat{\boldsymbol{p}}^{\mathrm{in}} = (1, 0, 0)^T$.

4.3.1 The role of pump depletion

When analyzing FRAs, it is a common, and often justified, practice to assume that the input power of the signal is much lower than that of the pump:

$$S_0^{\mathrm{in}} \ll P_0^{\mathrm{in}}. \tag{4.15}$$

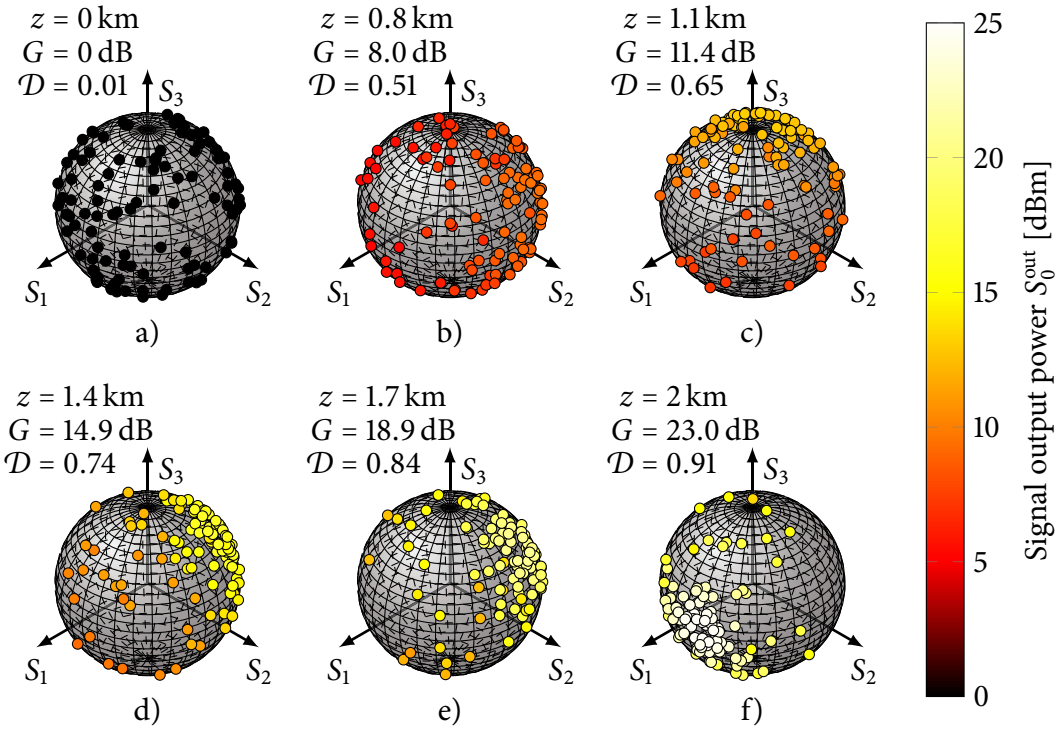

Figure 4.2: Poincaré spheres of the signal SOPs along one fiber realization. The fiber length is $L = 2\,\mathrm{km}$ and the PMDc is $D_P = 0.05\,\mathrm{ps\,km^{-1/2}}$. The signal and pump input power are, respectively, $S_0^{\mathrm{in}} = 1\,\mathrm{mW}$ and $P_0^{\mathrm{in}} = 8\,\mathrm{W}$, and the pump input SOP is $\hat{\boldsymbol{p}}^{\mathrm{in}} = (1, 0, 0)^T$.

This assumption lead to the so-called undepleted pump approximation, *i.e.* the pump is considered to be unaffected by the signal as it propagates along the fiber. The undepleted pump approximation can be applied to the model of Eqs. 4.3 by substituting Eq. (4.3b) with the following equation for the evolution of the pump [19]:

$$\frac{\mathrm{d}\boldsymbol{P}}{\mathrm{d}z} = \alpha_p \boldsymbol{P} - \left(\boldsymbol{M}\omega_p \boldsymbol{b} + \frac{2}{3}\gamma_{pp}\boldsymbol{P}_3 \right) \times \boldsymbol{P}\,, \tag{4.16}$$

where the dependence on the signal $\boldsymbol{S}$ has been dropped. The system of Eq. (4.16) and Eq. (4.3a) can be directly integrated using the RK4 method only.

Fig. 4.3 shows the evolution of the gain G and of the DOP $\mathcal{D}$ along the same fiber realization and with the same pump parameters of Fig. 4.2. Circles, triangles and squares refer, respectively, to a signal input power S_0^{in} of 100 mW, 1 mW and 10 µW. Solid curves refer to the solution obtained solving the complete model of Eqs. 4.3, whereas dashed curves refer to the undepleted pump approximation of Eq. (4.16). In particular, solid curves with triangles refer to the Poincaré spheres of Fig. 4.2. As it can be seen in Fig. 4.3, in the undepleted pump approximation the DOP and the gain do not depend on the signal power due to the decoupling of the pump from the signal Moreover, the complete model performs better in repolarizing the signal even if the gain is lower (circles). For low signal powers (triangles and squares), the behavior of the gain and of the DOP is similar and both increase as the signal propagates toward the input pump. In this case, at the end of the fiber, the gain prediction by the approximated model is about 5 dB lower when compared to the full model, and the output DOP is less than half.

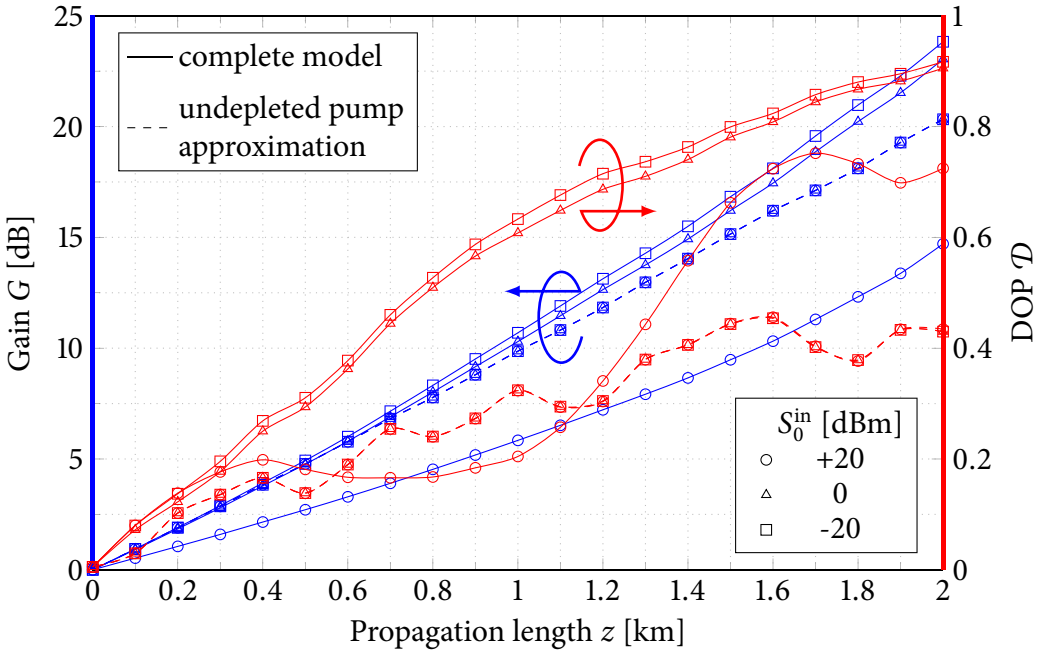

Figure 4.3: Evolution of the gain G and of the DOP $\mathcal{D}$ of the signal along the fiber for one birefringence realization. The fiber length is $L = 2\,\mathrm{km}$ and the PMDc is $D_P = 0.05\,\mathrm{ps\,km^{-1/2}}$. The pump input power is $P_0^{\mathrm{in}} = 8\,\mathrm{W}$, and the pump input SOP is $\hat{\boldsymbol{p}}^{\mathrm{in}} = (1, 0, 0)^T$. Circles, triangles and squares refer, respectively, to a signal input power S_0^{in} of 100 mW, 1 mW and 10 µW. Solid curves refer to the solution obtained solving the complete model of Eqs. 4.3, whereas dashed curves refer to the undepleted pump approximation of Eq. (4.16).

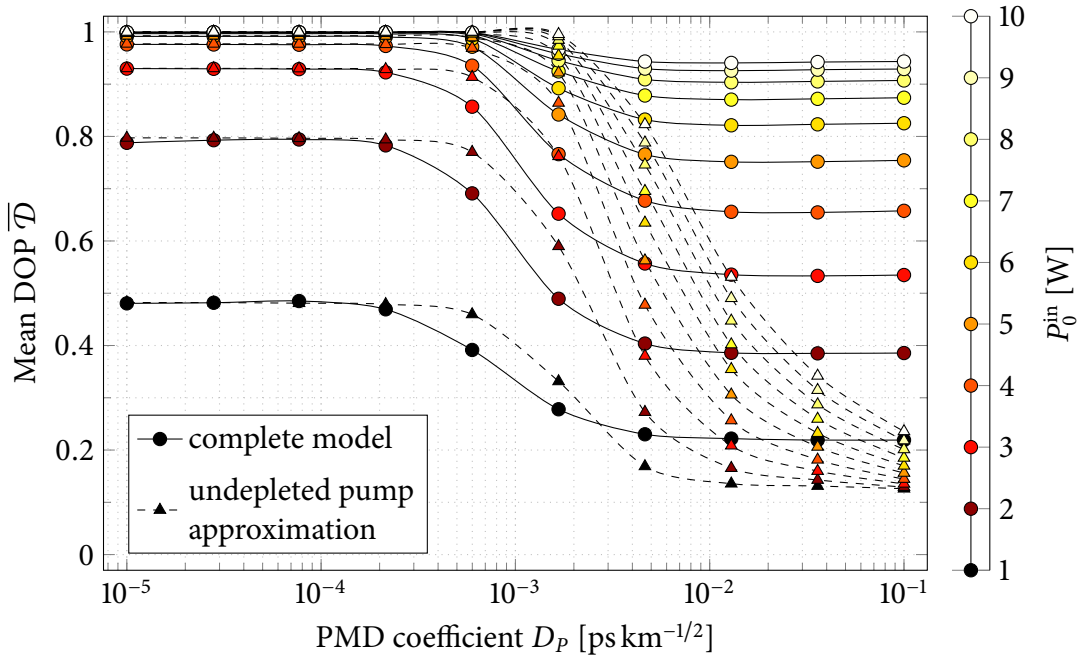

Figure 4.4: Mean signal output DOP as a function of the PMD coefficient D_P. The signal input power is $S_0^{\text{in}} = 1\,\text{mW}$ and the pump input SOP is $\hat{\boldsymbol{p}}^{\text{in}} = (1,0,0)^T$. Different colors encode different pump input power P_0^{in} in the range from 1 W to 10 W. Reprinted from [P.3] © 2011 IEEE.

Therefore, when dealing with polarization, the undepleted pump approximation does not always give correct results. The positive influence of depletion can be explained considering the following term in Eqs. 4.3:

$$\boldsymbol{\rho} = S_0\boldsymbol{P} + P_0\boldsymbol{S} = P_0S_0(\hat{\boldsymbol{p}} + \hat{\boldsymbol{s}}) = \rho_0\hat{\boldsymbol{\rho}}\,, \tag{4.17}$$

which describes parallel Raman gain for the signal $\boldsymbol{S}$ and acts as Raman depletion for the pump $\boldsymbol{P}$. In fact, $\boldsymbol{\rho}$ acts in exactly the same way both on the pump and on the signal polarizations, forcing them to evolve toward the common direction $\hat{\boldsymbol{\rho}}$. For the signal at the output of the fiber it holds $\hat{\boldsymbol{p}}(z=L) = \hat{\boldsymbol{p}}^{\text{in}}$; therefore $\boldsymbol{\rho}(z=L) = P_0S_0(\hat{\boldsymbol{p}}^{\text{in}} + \hat{\boldsymbol{s}}^{\text{out}})$ and $\hat{\boldsymbol{s}}^{\text{out}}$ is forced to converge toward $\hat{\boldsymbol{p}}^{\text{in}}$ as P_0 is maximum at its input, and S_0 is being amplified.

Fig. 4.4 shows the mean DOP of the output signal as a function of the PMDc D_P for a fiber long $L = 2\,\text{km}$. The signal input power is fixed at $S_0^{\text{in}} = 1\,\text{mW}$ whereas the pump input power P_0^{in} is varied from 1 W to 10 W. The pump has a linear input SOP $\hat{\boldsymbol{p}}^{\text{in}} = (1,0,0)^T$. Solid curves with circles refer to the complete model of Eqs. 4.3, whereas dashed curves with triangles refer to the undepleted pump approximation of Eq. (4.16), achieved by neglecting the signal contributions. In the complete model, for a fixed pump power the DOP is almost constant both for the very low ($D_P \leq 10^{-4}\,\text{ps km}^{-1/2}$) and the moderately-high ($D_P \geq 10^{-2}\,\text{ps km}^{-1/2}$) PMD regimes.

For very low PMD, high DOP ($\mathcal{D} > 0.9$) is achieved for pump input powers higher than 3 W. In this region the effect of the birefringence is negligible and the fiber can be considered isotropic. Moreover, in this PMD regime the results are in agreement with those obtained in the undepleted pump approximation.

For increasing PMD, as it will be explained in Section 4.3.2, random birefringence

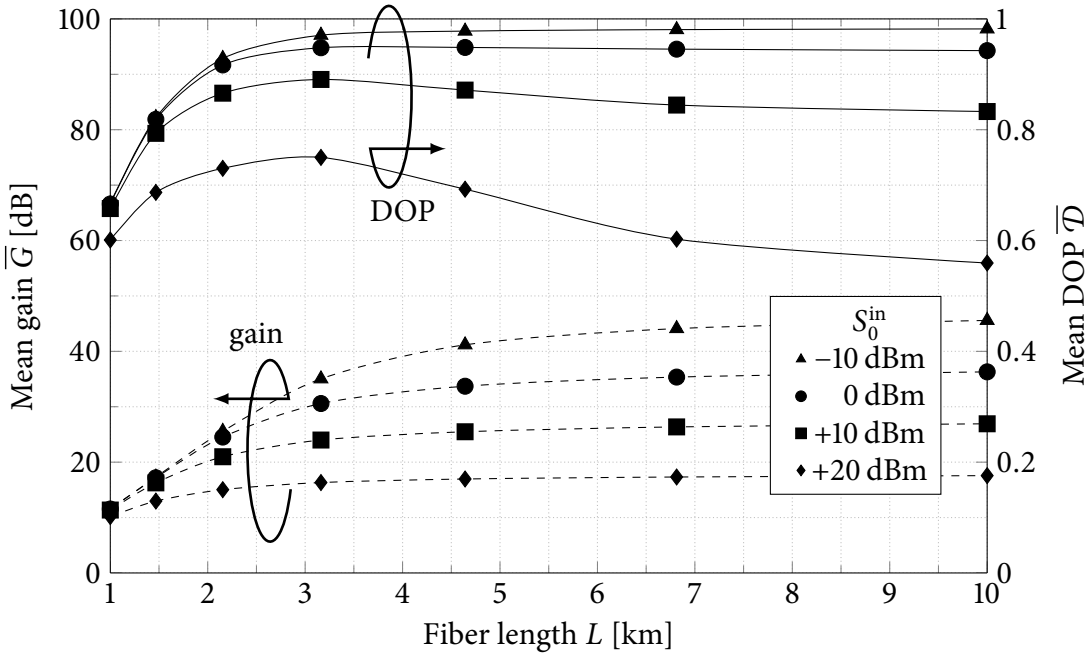

Figure 4.5: Mean signal output DOP $\overline{\mathcal{D}}$ and gain $\overline{G}$ as a function of the fiber length L, with a PMD coefficient $D_P = 0.05\,\text{ps}\,\text{km}^{-1/2}$. The pump input power is $P_0^{\text{in}} = 8\,\text{W}$ with SOP $\hat{\boldsymbol{p}}^{\text{in}} = (1, 0, 0)^T$. Triangles, circles, squares and diamonds refer to signal input power S_0^{in} of 0.1 mW, 1 mW, 10 mW and 100 mW, respectively. Reprinted from [P.3] © 2011 IEEE.

reduces the effective Raman gain [149], lowering the DOP. In the moderately-high PMD regime, however, the results severely differ between the two models. Actually, if the undepleted regime is considered the achievable DOP drastically decreases. This is in agreement with the analysis performed by Kozlov *et al.* [24], [21] made in the undepleted pump approximation. The complete model, instead, gives better results, and $\mathcal{D} > 90\%$ can still be reached for pump power higher than 8 W.

Therefore, it is worthwhile remarking that in the moderately-high PMD regime pump depletion plays a crucial role. Note also that this effect is visible only for moderately-high PMD, because only in this regime Raman attraction is hampered by fiber birefringence. However, for the same reason, in this PMD regime counter-propagating attraction performs better than co-propagating Raman attraction, as it is evident upon comparing Fig. 4.4 with Fig. 1(d) of Ursini *et al.* [22]. Indeed, in co-propagation the term $\boldsymbol{\rho}$ acts on pump and signal with opposite signs (see Eqs. (1) and (2) of Ref. [22]), therefore hampering polarization attraction.

Fig. 4.5 shows the mean signal output DOP $\overline{\mathcal{D}}$ and gain $\overline{G}$ as a function of the fiber length L, for $D_P = 0.05\,\text{ps}\,\text{km}^{-1/2}$ and for four different signal input powers S_0^{in}. The input pump power is $P_0^{\text{in}} = 8\,\text{W}$ with SOP $\hat{\boldsymbol{p}}^{\text{in}} = (1, 0, 0)^T$. For low signal input powers (triangles and circles) the DOP saturates, whereas for higher powers (squares and diamonds), the DOP reaches a maximum and then decreases for increasing fiber length. It may be noted that such a local maximum occurs when the gain $\overline{G}$ is almost compressed to a lower value. In this condition, an increase of the fiber length does not increase significantly Raman amplification and attraction; whereas on the other hand, the increased fiber length L enhances the scrambling effect of PMD, worsening the DOP, as it will be explained

in Section 4.3.2. Clearly the lower the compression value of the gain, the stronger this effect.

4.3.2 Effects of polarization-mode dispersion

As explained above, the vector $\boldsymbol{b}$ account for the random birefringence of the fiber. The effect of PMD can be analyzed by considering the diffusion length L_D, defined as [52]:

$$L_D = \frac{3}{\left(D_P \Delta\Omega\right)^2}\,, \tag{4.18}$$

where $\Delta\Omega = \omega_p + \omega_s$ is the relative frequency between the counter-propagating signal and pump [52], [149], *i.e.* due to the counter-propagation the relative frequency is given by the sum[1] of the optical frequencies of the pump and of the signal.

Actually, Eq. (4.18) describes the distance after which the SOPs of the pump and of the signal become uncorrelated. If the diffusion length is much shorter than the effective length[2] L_{eff} of the fiber,

$$L_D \ll L_{\text{eff}}\,, \tag{4.20}$$

then, due to the high relative velocity, the Raman gain coefficient as seen by the signal is averaged as follows [149], [163]:

$$g_{\text{R}}^{\text{avg}} = \frac{g_{\text{R}} + g_{\text{R}}^{\perp}}{2} \approx \frac{g_{\text{R}}}{2}\,. \tag{4.21}$$

Fig. 4.6 shows the mean gain $\overline{G}$ as a function of the length of the fiber L and for four different signal input powers S_0^{in}. The input pump power is $P_0^{\text{in}} = 8\,\text{W}$ with linear SOP $\hat{\boldsymbol{p}}^{\text{in}} = (1, 0, 0)^T$. The PMDc of the fibers is $D_P = 0.05\,\text{ps}\,\text{km}^{-1/2}$. The corresponding value of the diffusion length given by Eq. (4.18) is $L_D \approx 0.2\,\text{m}$, which satisfies the above condition Eq. (4.20). Therefore the expected Raman coefficient for the signal is given by Eq. (4.21). In Fig. 4.6 solid curves refer to the complete model of Eqs. 4.3, whereas the dashed curves refer to the scalar model developed by Santagiustina [164], which gives exact, although integral, solutions for the gain considering pump depletion[3]. The halved Raman coefficient $g_{\text{R}}^{\text{avg}} = g_{\text{R}}/2$ has been used only for the scalar model.

As it can be seen, the gain given by the scalar model always underestimate the gain obtained by solving the vector model. However, the two models agree quite well for long fibers, where as previously seen, the effect of attraction is hampered by PMD (see Fig. 4.5).

For short fibers, instead, the attraction process reduces the averaging effect of PMD, because the signal SOP $\hat{\boldsymbol{s}}$ evolves with $\hat{\boldsymbol{\rho}}$ and thus $\hat{\boldsymbol{p}}$. Therefore, the effective Raman coefficient as seen by the signal is higher than $g_{\text{R}}^{\text{avg}}$ given in Eq. (4.21).

Moreover, also the results regarding the pump depletion are in agreement between the two models.

[1] If co-propagation is considered, then $\Delta\Omega = \omega_p - \omega_s$.

[2] The effective length L_{eff} of the fiber is defined as [52]:

$$L_{\text{eff}} = \frac{1}{P_0^{\text{in}}} \int_0^L P_0(z)\,\mathrm{d}z \approx \frac{1 - \mathrm{e}^{-\alpha_p L}}{\alpha_p}\,, \tag{4.19}$$

where the approximation is valid for the scalar case in the undepleted pump approximation [52].

[3] Another solution for the gain in counter-propagating FRAs, but without considering pump depletion, can be found in [165]. In the case of co-propagating FRAs, solutions considering pump depletion can be found in [164], [166].

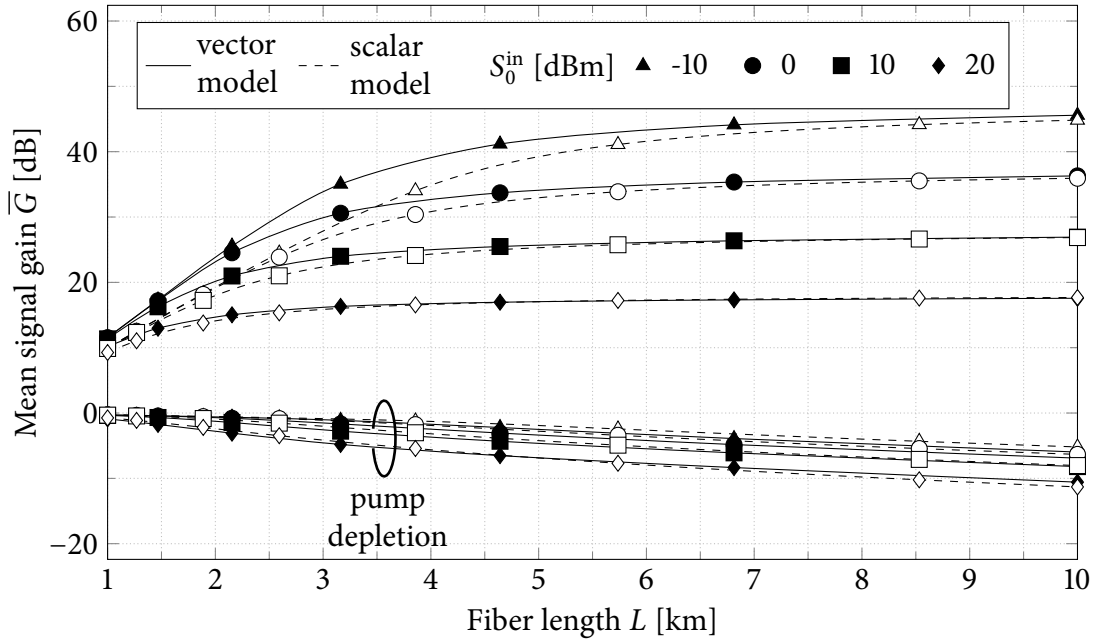

Figure 4.6: Mean signal gain $\overline{G}$ as a function of the fiber length L, with PMD coefficient $D_P = 0.05\,\mathrm{ps\,km^{-1/2}}$. The pump input power is $P_0^{\mathrm{in}} = 8\,\mathrm{W}$ with SOP $\hat{\boldsymbol{p}}^{\mathrm{in}} = (1, 0, 0)^T$. Triangles, circles, squares and diamonds refer, respectively, to signal input power S_0^{in} of 0.1 mW, 1 mW, 10 mW and 100 mW. Solid lines refer to the complete model of Eqs. 4.3, whereas dashed curves refer to the scalar model of [164]. The curves at the bottom refer to the pump depletion.

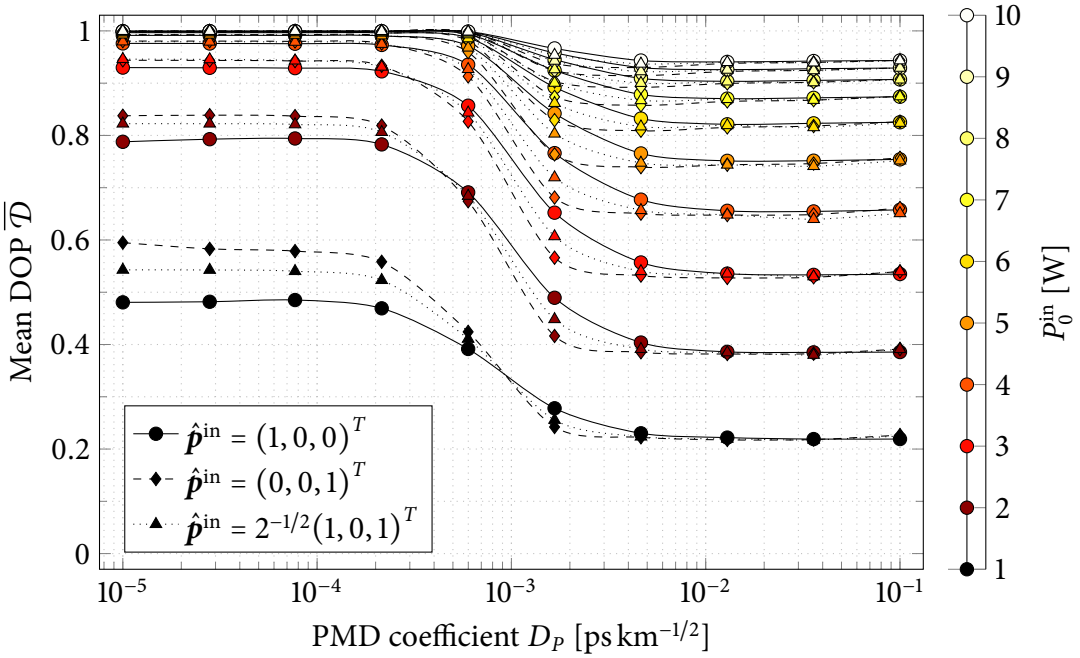

Figure 4.7: Mean signal output DOP $\overline{\mathcal{D}}$ as a function of the PMD coefficient D_P for three different pump input SOPs $\hat{\boldsymbol{p}}^{\text{in}}$. The signal input power is $S_0^{\text{in}} = 1\,\text{mW}$. Different colors encode different pump input power P_0^{in} in the range from 1 W to 10 W.

4.3.3 Performance and limits

In Fig. 4.7 it is shown the mean DOP of the output signal as a function of the PMDc D_P for a fiber long $L = 2\,\text{km}$. The signal input power is fixed at $S_0^{\text{in}} = 1\,\text{mW}$ whereas the pump input power P_0^{in} is varied from 1 W to 10 W. Circles, diamonds and triangles refer, respectively, to a linear ($\hat{\boldsymbol{p}}^{\text{in}} = (1,0,0)^T$), a right-handed circular ($\hat{\boldsymbol{p}}^{\text{in}} = (0,0,1)^T$) and an elliptical ($\hat{\boldsymbol{p}}^{\text{in}} = 2^{-1/2}(1,0,1)^T$) pump input SOP. The data for the linear case are the same presented above in Fig. 4.4. As it can be seen, for a fixed pump configuration the DOP is almost constant both for the very low and the moderately-high PMD regimes, as seen in Fig. 4.4.

Remarkably, in the moderately-high PMD regime the averaging effect of the random birefringence render the output DOP independent of the pump input SOP. Note that for the power levels considered here, the Kerr contributions $\boldsymbol{W}_p$ and $\boldsymbol{W}_s$ are negligible compared with fiber birefringence.

In the low PMD regime, instead, the repolarization efficiency depends on the pump SOP. In this regime $L_D > 47\,\text{km}$ and therefore the condition of Eq. (4.20) is not satisfied. In this case the signal is subjected to higher Raman gain. The difference for the different pump SOPs may be attributed to residual Kerr effect of $\boldsymbol{W}_p$ and $\boldsymbol{W}_s$ which, for this PMD regime, are not negligible with respect to the birefringence vector $\boldsymbol{b}$. However, it worth to note that such a low value of PMD is not realistic for standard SMFs.

Fig. 4.8 shows the mean of the angle $\overline{\theta}$ between the mean signal output SOP, $\langle \hat{\boldsymbol{s}}^{\text{out}} \rangle_{\text{sops}}$, and the pump input SOP, $\boldsymbol{M}\hat{\boldsymbol{p}}^{\text{in}}$, defined analogously to the definitions of $\overline{\mathcal{D}}$ and $\overline{G}$ given

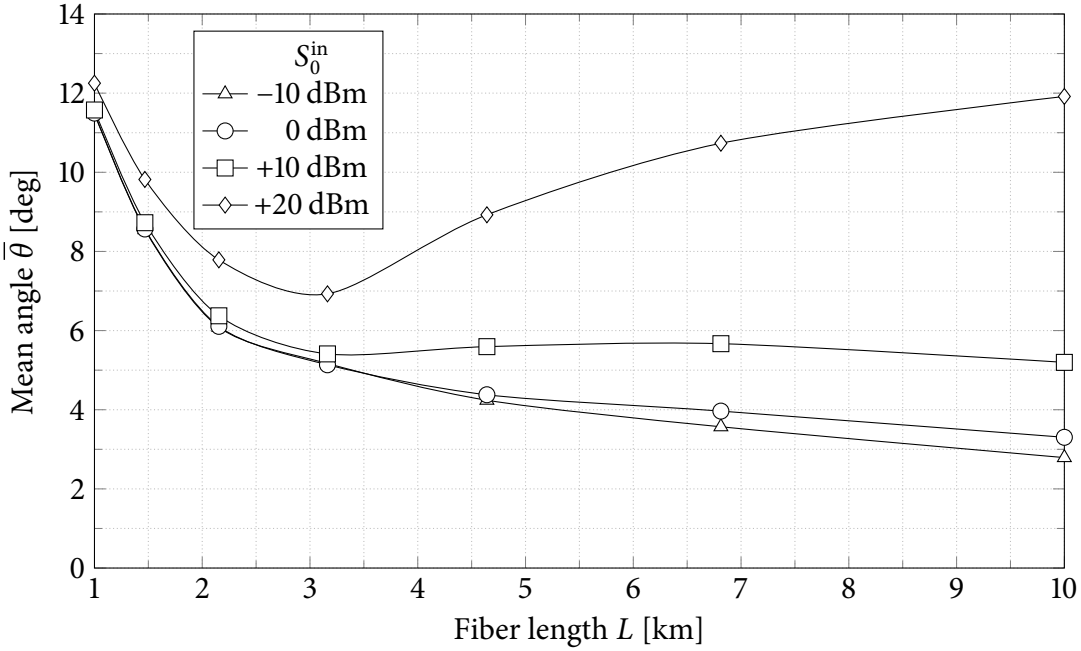

Figure 4.8: Mean signal-pump angle $\overline{\theta}$ as a function of the fiber length L, with a PMD coefficient $D_P = 0.05\,\text{ps}\,\text{km}^{-1/2}$. The pump input power is $P_0^{\text{in}} = 8\,\text{W}$ with SOP $\hat{\boldsymbol{p}}^{\text{in}} = (1,0,0)^T$. Triangles, circles, squares and diamonds refer to signal input power S_0^{in} of 0.1 mW, 1 mW, 10 mW and 100 mW, respectively. Reprinted from [P.3] © 2011 IEEE.

in Eqs. 4.14:

$$\theta = \arccos\left(\langle \hat{\boldsymbol{s}}^{\text{out}} \rangle_{\text{sops}} \cdot \boldsymbol{M} \hat{\boldsymbol{p}}^{\text{in}}\right), \tag{4.22a}$$

$$\overline{\theta} = \langle \theta \rangle_{\text{fibers}}. \tag{4.22b}$$

Actually, $\overline{\theta}$ indicates that effectively the signal, when attracted, is attracted toward the pump, thus overcoming the unpredictability of co-propagating schemes [22]. Results almost identical to those presented in Fig. 4.8 have been obtained also for circular ($\hat{\boldsymbol{p}}^{\text{in}} = (0,0,1)^T$) and elliptical ($\hat{\boldsymbol{p}}^{\text{in}} = 2^{-1/2}(1,0,1)^T$) pump input SOPs, confirming the independence on the pump input SOP.

Fig. 4.9 shows the signal output mean DOP $\overline{\mathcal{D}}$ as a function of the mean gain $\overline{G}$. The four curves with marks are the same presented in Fig. 4.5. Stars are obtained by varying the parameters in such a way to prevent gain compression: the fiber length L in the range from 1 km to 10 km, the pump input power P_0^{in} in the range from 1 W to 5 W and the signal input power S_0^{in} in the range from 0.01 mW to 1 mW. The pump input SOP is $\hat{\boldsymbol{p}}^{\text{in}} = (1,0,0)^T$.

The data have been empirically interpolated by the following function [P.3]:

$$\overline{\mathcal{D}} = 1 - \mathrm{e}^{-\overline{G}_{\text{dB}}/\Gamma}, \tag{4.23}$$

where $\overline{G}_{\text{dB}} = 10\log_{10}\overline{G}$ and $\Gamma \approx 10.2$ (solid curve in Fig. 4.9). Only recently, Kozlov *et al.* [29], [147] have analytically calculated the relationship between the DOP and the mean gain, G, in the case of standard or high PMD through a simplified theoretical model,

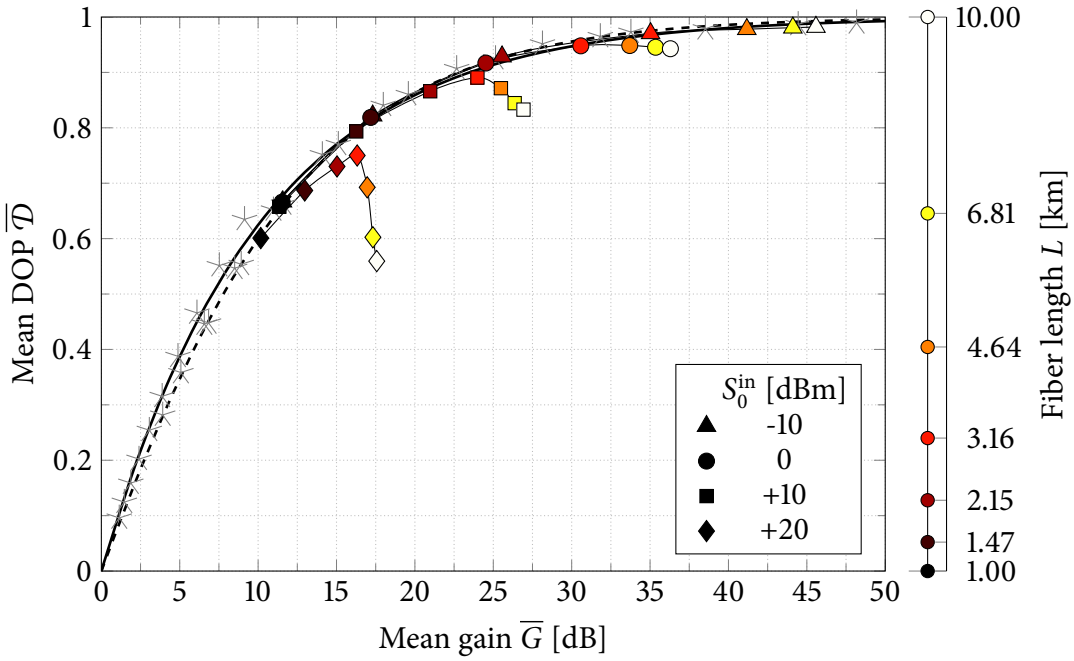

Figure 4.9: Mean signal DOP $\overline{\mathcal{D}}$ as a function of the gain $\overline{G}$, for a PMDc $D_P = 0.05\,\text{ps}\,\text{km}^{-1/2}$. The four curves with marks are the same of Fig. 4.5. Stars are obtained by varying fiber length L in the range from 1 km to 10 km and pump (signal) input power P_0^{in} (S_0^{in}) in the range from 1 W to 5 W (0.01 mW to 1 mW). Pump input SOP is $\hat{\boldsymbol{p}}^{\text{in}} = (1, 0, 0)^T$. The solid curve is given by Eq. (4.23), whereas the dashed curve is obtained using Eq. (4.24). Reprinted from [P.3] © 2011 IEEE.

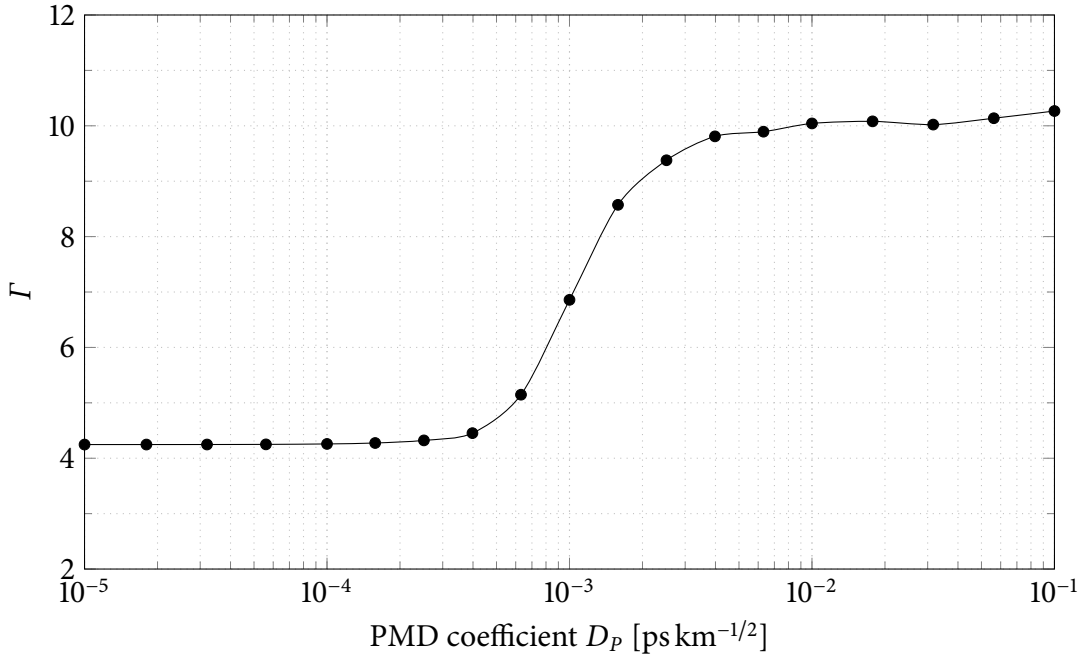

Figure 4.10: Coefficient Γ as a function of the PMDc D_P. The pump input power is $P_0^{\text{in}} = 3\,\text{W}$ with SOP $\hat{\boldsymbol{p}}^{\text{in}} = (1,0,0)^T$. The signal input power S_0^{in} is varied in the range from 0.01 mW to 1 mW, while fiber length L varies from 1 km to 8 km. Reprinted from [P.3] © 2011 IEEE.

according to which [29], [147]

$$\mathcal{D} = 1 - 4\left(1 + \sqrt{1 + 8G}\right)^{-1}. \tag{4.24}$$

This curve is also shown in Fig. 4.9 (dashed curve) together with Eq. (4.23) (solid curve). Clearly there is a good agreement between the two expressions.

Both functions provide a good estimate, except for those points corresponding to the almost compressed gain regime shown in Fig. 4.5 and discussed above. Actually, Eq. (4.23) and Eq. (4.24) provide an estimate of the expected output DOP for a given mean gain $\overline{G}$, or, conversely, they provide the required gain to reach a desired DOP. That specific gain can be obtained by appropriately choosing the fiber length, the signal and the pump input powers in such a way that the gain does not compress. For instance, in the case presented in Fig. 4.9, where the fibers have $D_P = 0.05\,\text{ps}\,\text{km}^{-1/2}$, which is a common value for standard fibers, in order to have a $\mathcal{D} > 0.9$, an uncompressed gain of about 25 dB is required at least.

It is however important to emphasize that Eq. (4.23) and Eq. (4.24) provide only an upper bound to the achievable DOP $\overline{\mathcal{D}}$ for a given gain $\overline{G}$. Actually, the attained DOP may be lower if the FRA is operated in a condition of gain compression, as previously seen.

Finally, Fig. 4.10 shows how the coefficient Γ of Eq. (4.23) varies with the PMDc D_P. Fig. 4.10 has been obtained by repeating the analysis of Fig. 4.9 for different values of fiber L, correlation L_C and beat L_B lengths, and pump P_0^{in} and signal S_0^{in} input powers, chosen in such a way to prevent gain compression.

Note in particular that Γ is almost constant in the very low and in the moderately-high PMD regimes, similarly to the DOP $\overline{\mathcal{D}}$ in Fig. 4.7. Moreover, the analysis of Kozlov *et*

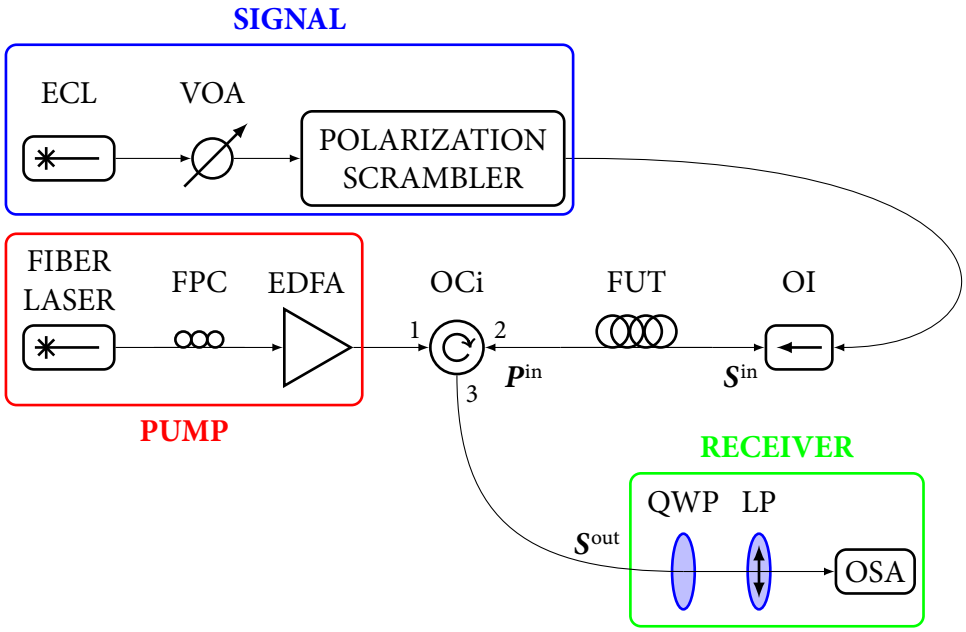

Figure 4.11: Experimental setup for the analysis of NPA in FRAs. ECL: external cavity laser; VOA: variable optical attenuator; OI: optical isolator; FPC: fiber polarization controller; EDFA: erbium-doped fiber amplifier; FUT: fiber under test; OCi: optical circulator; QWP: quarter-wave plate; LP: linear polarizer; OSA: optical spectrum analyzer.

al. [29] is in agreement with the values of Γ in the two PMD regimes. It is worthwhile to note that for PMDc values larger than about 0.005 ps km$^{-1/2}$, *i.e.* for all existing SMFs, Γ is practically a constant.

4.4 Experimental characterization

The first experiment related to NPA in FRAs is due to Martinelli *et al.* [18], where signal repolarization was observed in the case of a co-propagating FRA. Recently, Morin *et al.* [30] demonstrated simultaneous NPA and Raman amplification in a counter-propagating setup, but in their configuration the NPA was mostly driven by the Kerr effect.

This section presents the results, based on the publication [P.2], of the experimental characterization of purely Raman-based polarization attraction in SMFs aimed to verify the relationship between DOP and the gain given by Eq. (4.24). Ultimately, the difference between the Raman-assisted Kerr-based NPA and the purely Raman-based NPA lays in the power levels of the pump and of the signal, which are comparable in the former case [30] and very different in the latter [29], [P.3], [147].

4.4.1 Experimental setup

The experimental setup is shown in Fig. 4.11. The pump source is realized by a tunable fiber laser, a fiber polarization controller (FPC) and a variable-gain high-power erbium-doped fiber amplifier (EDFA). This pump source, described in detail in Section 3.1, is tunable in the C band providing Raman amplification for signals in the U band; it has a linewidth of about 0.1 nm and DOP $\mathcal{D} = 0.99$. Pumping in the C band permits to have wider flexibility

in the pump due to the higher availability of devices. The broad linewidth increases the threshold of SBS and therefore decreases the induced pump depletion [81].

The gain of the EDFA can be varied, enabling the selection of the pump power P_0^{in} injected into the fiber in the range between 20 dBm and 35 dBm. In order to increase the efficiency and to reduce the noise, the wavelength of the pump is set to $\lambda_p = 1541$ nm to operate at the maximum of the gain of the EDFA.

The signal is generated by an external cavity laser (ECL) and its power S_0^{in} can be varied through a variable optical attenuator (VOA) from −30 dBm to 0 dBm. For a Raman frequency shift of $f_{\text{R}} = 13.2$ THz the corresponding gain peak is at about $c\left(f_p - f_{\text{R}}\right)^{-1} \approx 1650$ nm ($f_p = c/\lambda_p$). However, due to limits in the operating range of the ECL, the signal is transmitted at $\lambda_s = 1640$ nm. Consequently the efficiency of SRS is slightly reduced from the maximum. The signal polarization scrambler, analyzed in detail in Appendix C, is a fast four-channel fiber-squeezer polarization controller driven by four statistically independent random signals. The resulting rate of the random scrambling of the signal SOP is about 20 kHz.

The SOP of the amplified signal $\boldsymbol{S}^{\text{out}}$, emerging from the FRA, is measured and analyzed by a rotating quarter-wave plate (QWP) polarimeter. The polarimeter, described in Appendix B, is composed by a rotating QWP followed by a fixed linear polarizer (LP) and an optical spectrum analyzer (OSA). An OSA-based setup permits the measurement of the average SOP over the time and over a suitable bandwidth centered at the signal wavelength λ_s. In this way the amplified spontaneous emission (ASE) induced by the Raman amplifier can be monitored and controlled. This is necessary because for some combinations of the signal and the pump input powers the ASE can become non-negligible. The SOP of the received signal $\boldsymbol{S}^{\text{out}}$ is determined by measuring the spectra transmitted by the linear polarizer for five different orientations of the QWP [167].

In previous experiments of NPA, the rate at which the output SOP is measured is faster than the rate at which the input SOP is scrambled [18]. In this way, the instantaneous SOP of the transmitted signal is measured, and the DOP is numerically evaluated by averaging the measured SOPs. Instead, the OSA-based approach permits to directly measure the mean SOP $\left\langle \boldsymbol{S}^{\text{out}} \right\rangle_{\text{sops}}$. The OSA acquisitions are slowed down to about 5 s per wavelength by increasing the averaging time. Recalling that the input SOP is scrambled at about 20 kHz, the above procedure is roughly equivalent to averaging the output SOP over some 10^5 random input SOPs. More details are given in Appendix C.

4.4.2 Results

The DOP and the mean gain G of the transmitted signal have been measured for different signal (S_0^{in}) and pump (P_0^{in}) input powers, over four links made of G.655 fiber bobbins, with different lengths L and different PMDc D_P. Results and link parameters are shown in Fig. 4.12, where the pump and the signal input powers are encoded in colors and markers, respectively, as detailed in the legend of the figure. The solid lines connect points corresponding to the same signal input power, whereas the dashed curves represent the theoretical result given by Eq. (4.24). The DOP of the input signal was about 0.05, as shown by the points corresponding to $P_0^{\text{in}} =$ ''off''.

Fig. 4.12(a), in particular, refers to the data measured on the 2.90 km fiber link. Clearly, as the pump power is increased, the gain increases and so does correspondingly the

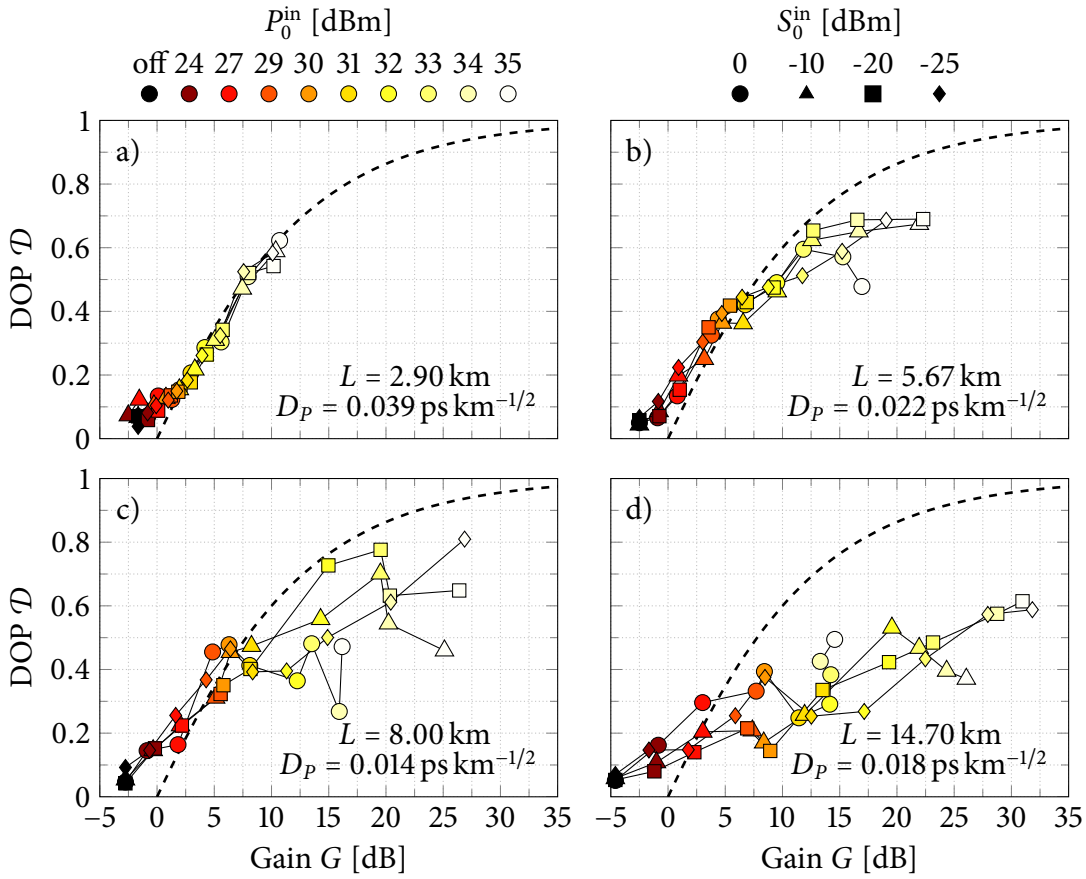

Figure 4.12: Measured DOP $\mathcal{D}$ as a function of the gain G for different pump (P_0^{in}) and signal (S_0^{in}) input powers, and for four different link lengths L: (a) L = 2.90 km (D_P = 0.039 ps km$^{-1/2}$), (b) L = 6.57 km (D_P = 0.022 ps km$^{-1/2}$), (c) L = 8.00 km (D_P = 0.014 ps km$^{-1/2}$), (d) L = 14.70 km (D_P = 0.018 ps km$^{-1/2}$). Dashed curves refer to Eq. (4.24). Reprinted from [P.2] © 2012 OSA.

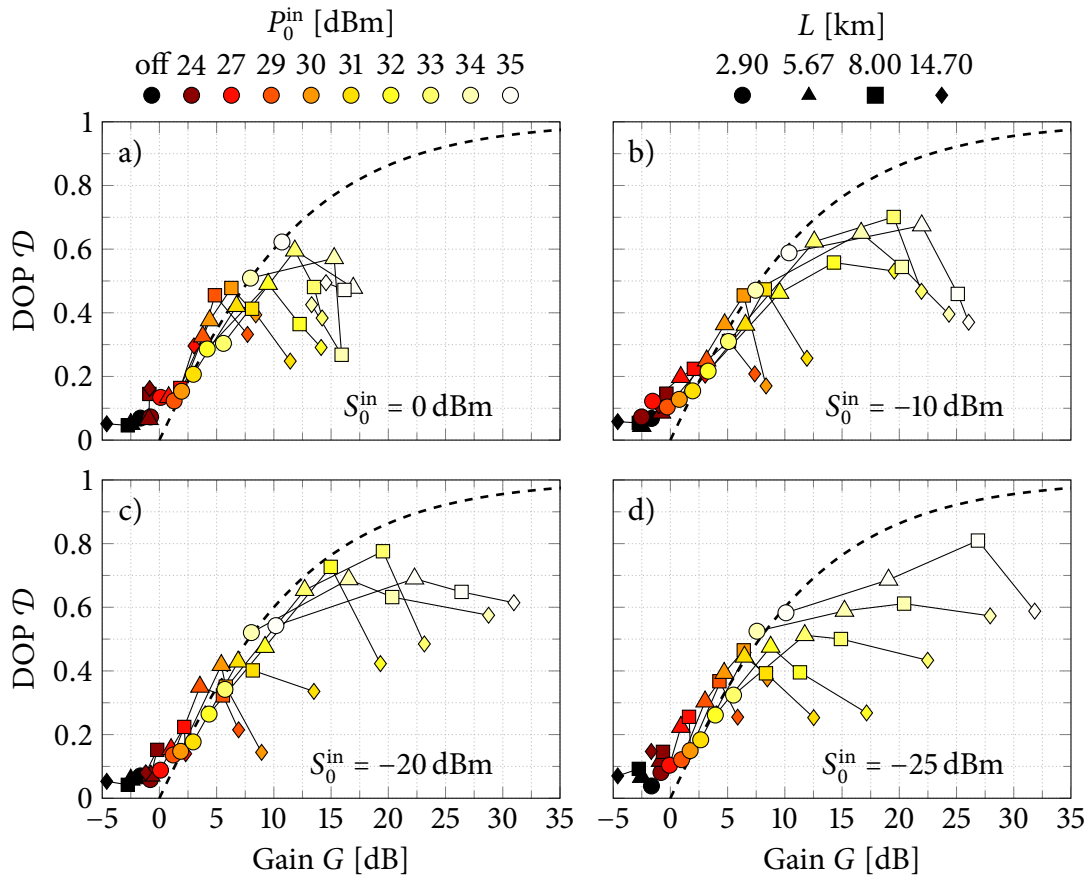

Figure 4.13: Measured DOP $\mathcal{D}$ as a function of the gain G for different pump input powers P_0^{in} and link lengths L, and for four different signal input powers S_0^{in}: (a) $S_0^{in} = 0$ dBm, (b) $S_0^{in} = -10$ dBm, (c) $S_0^{in} = -20$ dBm, (d) $S_0^{in} = -25$ dBm. Dashed curves refer to Eq. (4.24). Reprinted from [P.2] © 2012 OSA.

DOP. Noticeably, the relationship between $\mathcal{D}$ and G is in very good agreement with the theoretical result and almost independent of the signal input power. As the fiber length is increased, higher gain and DOP can be achieved, but the relationship between the two tends to deviate from the theoretical prediction. This is due to the effect of gain compression discussed in Section 4.3. For $G < 5$ dB the DOP is higher than the theoretical upper bound. This effect is due to fiber losses which can contrast Raman gain, but, being scalar in nature, have no direct effect on repolarization. As a result, even if the overall gain may be not large enough to overcome losses, there still is a local polarization attraction that contributes to an overall small repolarization. Note that the model in [29], [147] does not account for losses, and the analysis of Section 4.3 has not fully explored the case of low gain. Indeed, the upper bounds given by Eq. (4.23) and Eq. (4.24) should be considered valid only for high gain.

The same data shown in Fig. 4.12 are rearranged differently in Fig. 4.13. In this case each graph refers to a specific signal input power, markers encode fiber lengths, solid lines connect points for increasing fiber length and colors still encode pump input power as in Fig. 4.12. It is now clear that for a given signal input power and a given pump input power, as the fiber length is increased both gain and DOP increase in agreement with Eq. (4.24),

but if the length is further increased, the condition of gain compression may be achieved, worsening the performance of the polarization attraction. The experimental data confirms, however, that Eq. (4.24) (and Eq. (4.23)) represents an upper bound to the signal DOP that can be achieved by exploiting the Raman-based NPA, for a given Raman mean gain G.

4.5 Conclusions

In this chapter, the polarization evolution of signal and pump in counter-propagating randomly birefringent FRAs has been modeled and analyzed, including the effects of NPR, pump depletion and orthogonal Raman gain. It has been shown that even for a moderately-high birefringent fiber the counter-propagating scheme is effective in attracting the signal output SOP toward the input pump SOP, achieving a DOP whose maximum is a function of the signal gain. Moreover, it has been shown that for moderately-high PMD, pump depletion plays a key role in signal repolarization, to the extent that in this regime counter-propagation performs better than co-propagation. A simple empirical rule, namely Eq. (4.23), lately theoretically demonstrated by Kozlov *et al.* [29], [147] (see Eq. (4.24)), has been presented, which allows a straightforward sizing of the FRA in order to achieve the requested DOP.

Finally, a detailed experimental characterization of the analysis of purely Raman-based NPA given in Section 4.3, has been reported in Section 4.4. By measuring the DOP and the Raman mean gain G of the transmitted signal, for different combinations of the pump and the signal input powers, and for different fiber link lengths, the relations between the maximum DOP and the mean gain G, as given by Eq. (4.23) and Eq. (4.24), have been validated.

Concluding, in order to use FRAs as efficient Raman polarizers, short fiber lengths and high power pumps should be preferred to prevent gain compression and the consequent efficiency reduction.

Chapter 5

Conclusions

$$e^{i\pi} + 1 = 0$$

Leonhard Paul Euler
1707 – 1783

The focus of this thesis has been the all-optical signal generation and processing through nonlinear amplification phenomena in single-mode fibers. Part of the thesis has been devoted to nonlinear fiber optical oscillators and part has been dedicated to nonlinear polarization attraction in fiber Raman amplifiers.

In the first part, three different nonlinear fiber optical oscillators have been investigated and experimentally demonstrated. First, a continuous-wave pump for fiber Raman amplifiers has been presented and discussed. Developed with the goal of achieving high degree of polarization, tunability and suppression of stimulated Brillouin scattering, it has been used to obtain nonlinear polarization attraction in fiber Raman amplifiers. One of the main feature of this fiber laser is the higher effectiveness in increasing the threshold of stimulated Brillouin scattering with respect to other suppression methods reported in the literature. Then, a fast and widely tunable fiber optical oscillator based on stimulated Raman scattering and on broad- and narrow-band fiber optical parametric amplification, each one dominating in a different spectral region, has been demonstrated and characterized. The time-dispersion-tuning technique permitted to select among the three amplification regimes, and a tuning range of 160 nm has been achieved with a sensitivity of about 23 nm kHz^{-1} and an estimated sweep speed of about 0.4 nm μs^{-1}. Finally, through the same time-dispersion-tuning method, a fast tunable optical frequency comb, realized exploiting cascaded four-wave mixing in the broad-band fiber optical parametric amplification regime, has been obtained by using a single pump, avoiding the limitations in spectral purity and frequency and phase stability given by double pump systems.

In the other part, the control of the state of polarization and of the degree of polarization through nonlinear polarization attraction in counter-propagating fiber Raman amplifiers in standard, randomly birefringent, single-mode fibers has been studied, analyzed and characterized. The analysis included the effects of pump depletion, nonlinear polarization rotation and orthogonal Raman gain, and showed that counter-propagating fiber Raman amplifiers are effective in attracting the signal toward a predetermined state of polarization settled by the pump input state of polarization. Moreover, the key role of pump depletion in achieving signal repolarization in fibers with moderately-high polarization-mode dispersion have been discussed, showing that in this regime counter-propagation performs better

than co-propagation. The performances and the limits of repolarization efficiency have been determined, leading to a quantitative relationship between the degree of polarization and the gain of the fiber Raman amplifier. This relationship represents an upper-bound on the maximum achievable degree of polarization, and allows a straightforward design of a fiber Raman amplifier in order to achieve a requested degree of polarization. The characterization showed that in order to use fiber Raman amplifiers as efficient Raman polarizers, short fiber lengths and high power pumps should be preferred to prevent gain compression and the consequent efficiency reduction.

Issues and possible solutions have been presented and proposed.

5.1 Future research

The tunable continuous-wave pump, described in Section 3.1, has been developed with the goal of achieving stimulated Brillouin scattering suppression in fiber Raman amplifiers, and more specifically to realize nonlinear polarization attraction in the U band (from 1625 nm to 1675 nm). Polarization attraction could be achieved, in theory, in any spectral region where the stimulated Raman scattering effect can be efficiently obtained by modifying the wavelength of the pump. In this case it is necessary to find alternative methods to generate such type of pump. For instance, a pump in the U band could be generated through a similar setup but using thulium-doped fibers, and, more important, research efforts are being spent also to achieve efficient amplification in the E and S bands (from 1360 nm to 1460 nm and from 1460 nm to 1530 nm, respectively), which is necessary to obtain nonlinear polarization attraction in the ''standard'' C band (from 1530 nm to 1565 nm).

Regarding nonlinear polarization attraction in fiber Raman amplifiers, analyzed in Chapter 4, only continuous-wave waves have been considered. Even if they approximates the steady state behavior of high data-rate transmissions, more detailed analysis should be performed, in particular to evaluate the impact of noise and of the presence of multiple channels, like in wavelength-division-multiplexing systems.

For what concern the tunable nonlinear fiber optical oscillator, discussed in Section 3.3, the sweep rate could be improved by shortening the loop length, such as by using highly nonlinear fibers or by using a higher dispersive element. Moreover, as the stimulated Raman scattering effect scales with the pump wavelength, with proper dispersion properties it could be possible to achieve lasing in other bands or in unusual spectral regions such as in the near infrared. As such region are continuously being explored, especially for sensing applications, they are worth being investigated, and, as pointed out before, good amplification stages have to be developed to reach the required pump peak power. However, the required average power is lower than that required for nonlinear polarization attraction.

Finally, for what concern the fast tunable optical frequency comb, discussed in Section 3.4, few issues should be addressed, the main being its temporal characterization, that could not be performed. The cascaded four-wave mixing, realized through a single pump, guarantee the coherence of the comb. However, deriving sufficient temporal information from average spectra is not possible, therefore more detailed analysis should be done, for instance through the use of an autocorrelator. Moreover, the time stability and the spectral broadening of the comb lines, and their possible effects, should also be analyzed.

Concluding, nonlinear optics will undoubtedly play a major role in the development

of future photonic devices and networks, and the work that has been presented in this thesis is an original contribution to advance knowledge in the fields of all-optical signal generation and processing.

Appendix A

The Stokes representation of light

Polarization is a key degree of freedom of the electromagnetic field. This Appendix provides a basic overview of the Stokes formalism for representing the polarization of the electromagnetic field; more in-depth discussions can be found in books such as Damask [168] or Collett [169].

Consider a monochromatic wave at angular frequency ω, with time dependence $\mathrm{e}^{\mathrm{i}\,\omega t}$, and propagating along the z-axis with propagation constant k. The electric field[1] $\boldsymbol{E}$ can be expressed as

$$\boldsymbol{E}(x, y, z, t) = \boldsymbol{E}_0(x, y) \exp[\mathrm{i}(\omega t - kz)]\,. \tag{A.1}$$

The complex amplitude $\boldsymbol{E}_0$ can be decomposed in terms of its orthogonal components in the transverse (x, y)-plane as

$$\boldsymbol{E}_0 = \begin{pmatrix} E_x \\ E_y \end{pmatrix} = \begin{pmatrix} A_x\, \mathrm{e}^{\mathrm{i}\,\varphi_x} \\ A_y\, \mathrm{e}^{\mathrm{i}\,\varphi_y} \end{pmatrix}, \tag{A.2}$$

which is called the Jones vector [170], and where A_x, A_y, φ_x and φ_y are four real parameters. The Jones vector fully determines the state of polarization (SOP) of the wave through the behavior of the two orthogonal components E_x and E_y over one optical cycle. However, Jones vectors can not be easily measured directly as the measurement involves the knowledge of two amplitudes and two phases of the optical field. Moreover, the Jones formalism can describe only fully polarized waves, as it can not account for zero or partial polarization.

A more useful and practical way to deal with polarization of light is by resorting to the Stokes formalism [171], which, by dropping the information on the absolute optical phases φ_x and φ_y, can directly deal with full and partial polarized waves and even with completely depolarized ones. Moreover, it only involves the measurement of optical powers (or intensities).

The Stokes representation is given by a four-component real vector $\boldsymbol{S} = (S_0, S_1, S_2, S_3)^T$,

[1] Without loss of generality, the following discussion is restricted by only considering the electric field $\boldsymbol{E}$; the magnetic field $\boldsymbol{H}$ can be derived from $\boldsymbol{E}$ by using the Faraday's law.

whose components are given by:

$$S_0 = E_x^* E_x + E_y^* E_y = |E_x|^2 + \left|E_y\right|^2 , \tag{A.3a}$$

$$S_1 = E_x^* E_x - E_y^* E_y = |E_x|^2 - \left|E_y\right|^2 , \tag{A.3b}$$

$$S_2 = E_x^* E_y + E_y^* E_x = 2\,\mathrm{Re}\left[E_x^* E_y\right] , \tag{A.3c}$$

$$S_3 = \mathrm{i}\left(E_y^* E_x - E_x^* E_y\right) = 2\,\mathrm{Im}\left[E_x^* E_y\right] , \tag{A.3d}$$

where S_0 is the total power of the electric field given by the sum of the powers of the two orthogonal components E_x and E_y, whereas S_1 is the difference between those powers. The third component S_2 is given by the difference between the intensities of the two orthogonal components of the field aligned at $\pm\pi/4$ in the (x, y)-plane. Finally, S_3 is given by the difference between the right- and the left-hand circular components. Therefore, the knowledge of six powers is needed to fully characterize a Stokes vector.

The Stokes vector $\boldsymbol{S}$ can be formally related[2] to the Jones vector $|S\rangle$ by the relation [172]

$$\boldsymbol{S} = \langle S|\boldsymbol{\sigma}|S\rangle \ , \tag{A.4}$$

where $\boldsymbol{\sigma}$ is the following four-components vector of matrices:

$$\boldsymbol{\sigma} = \begin{pmatrix} \boldsymbol{\sigma}_0 \\ \boldsymbol{\sigma}_1 \\ \boldsymbol{\sigma}_2 \\ \boldsymbol{\sigma}_3 \end{pmatrix} . \tag{A.5}$$

The matrix $\boldsymbol{\sigma}_0$ is the identity matrix

$$\boldsymbol{\sigma}_0 = \begin{pmatrix} 1 & 0 \\ 0 & 1 \end{pmatrix} , \tag{A.6}$$

whereas $\boldsymbol{\sigma}_i$, $i \in \{1, 2, 3\}$ are the Pauli's spin matrices [173]:

$$\boldsymbol{\sigma}_1 = \begin{pmatrix} 1 & 0 \\ 0 & -1 \end{pmatrix} , \tag{A.7a}$$

$$\boldsymbol{\sigma}_2 = \begin{pmatrix} 0 & 1 \\ 1 & 0 \end{pmatrix} , \tag{A.7b}$$

$$\boldsymbol{\sigma}_3 = \begin{pmatrix} 0 & -\mathrm{i} \\ \mathrm{i} & 0 \end{pmatrix} . \tag{A.7c}$$

In this way the four Stokes components are given by

$$S_i = \langle S|\boldsymbol{\sigma}_i|S\rangle \quad \text{for} \quad i \in \{0, 1, 2, 3\} . \tag{A.8}$$

[2]Jones vectors are commonly denoted with the ''ket'' notation $|\cdot\rangle$.

A.1 The degree of polarization

The Stokes representation allows to deal not only with fully polarized waves, but also with partially polarized and completely depolarized beams. In general a Stokes vector can be decomposed as

$$\boldsymbol{S} = \boldsymbol{S}_{\text{pol}} + \boldsymbol{S}_{\text{unpol}} = \begin{pmatrix} \mathcal{D}S_0 \\ S_1 \\ S_2 \\ S_3 \end{pmatrix} + (1-\mathcal{D}) \begin{pmatrix} S_0 \\ 0 \\ 0 \\ 0 \end{pmatrix}, \tag{A.9}$$

where the coefficient $\mathcal{D}$ is the degree of polarization (DOP), which is calculated as

$$\mathcal{D} = \frac{\sqrt{S_1^2 + S_2^2 + S_3^2}}{S_0}. \tag{A.10}$$

It can be shown from Eqs. A.3 that $\mathcal{D}$ is constrained to the interval

$$0 \leq \mathcal{D} \leq 1. \tag{A.11}$$

Unpolarized waves have $\mathcal{D} = 0$, whereas fully polarized waves have $\mathcal{D} = 1$. Partial polarization is described by $0 < \mathcal{D} < 1$. In particular, monochromatic plane waves have $\mathcal{D} = 1$. However, from a practical point of view, Stokes vectors are calculated by averaging the measured powers, and therefore the parameters S_i, over time. Eq. (A.10) is thus rewritten as

$$\mathcal{D} = \frac{\sqrt{\langle S_1 \rangle^2 + \langle S_2 \rangle^2 + \langle S_3 \rangle^2}}{\langle S_0 \rangle}, \tag{A.12}$$

where the averages $\langle \cdot \rangle$ are taken over a time interval of duration T:

$$\langle \cdot \rangle = \int_0^T \cdot \, \mathrm{d}t. \tag{A.13}$$

In this case, a wave exhibiting time fluctuations of its SOP may yield $\mathcal{D} < 1$.

Appendix B

Measurement of the Stokes parameters

Stokes vectors, as described in Appendix A, are defined by combining six different measurements of the residual power of the field transmitted by six different polarizers: two linear polarizers aligned along the x-axis and the y-axis, two aligned at $\pm\pi/4$, and two circular polarizers for the right- and the left-handed circular polarizations. Therefore, even by assuming that the linear polarizer can be rotated, two more polarizers are needed for the two circular polarizations. Thus at least three different polarizers are required. Moreover, such different polarizers have to be exchanged during the measurement. This render the measurement slow and susceptible to errors in the alignment of the polarizers.

The rotating quarter-wave plate (QWP) polarimeter [167], [174]–[176] is an alternative method, yet simple, precise and versatile, to measure the four-components Stokes vector of a light beam.

Fig. B.1 shows a schematic illustration of a rotating QWP polarimeter. The incident radiation, with unknown state of polarization $\boldsymbol{S}$, propagates through a QWP whose fast axis is at an angle θ from the x-axis of the reference system.

A QWP with its fast axis oriented along the x-axis is described by the following Müeller matrix [177]:

$$\boldsymbol{M}_{\mathrm{QWP}} = \begin{pmatrix} 1 & 0 & 0 & 0 \\ 0 & 1 & 0 & 0 \\ 0 & 0 & 0 & 1 \\ 0 & 0 & -1 & 0 \end{pmatrix}. \tag{B.1}$$

The matrix of a QWP rotated by an angle θ can be calculated as [168], [177]

$$\boldsymbol{M}(\theta) = \boldsymbol{R}(-\theta)\boldsymbol{M}(0)\boldsymbol{R}(\theta)\,, \tag{B.2}$$

where $\boldsymbol{R}(\theta)$ is the following rotation matrix:

$$\boldsymbol{R}(\theta) = \begin{pmatrix} 1 & 0 & 0 & 0 \\ 0 & \cos 2\theta & \sin 2\theta & 0 \\ 0 & -\sin 2\theta & \cos 2\theta & 0 \\ 0 & 0 & 0 & 1 \end{pmatrix}. \tag{B.3}$$

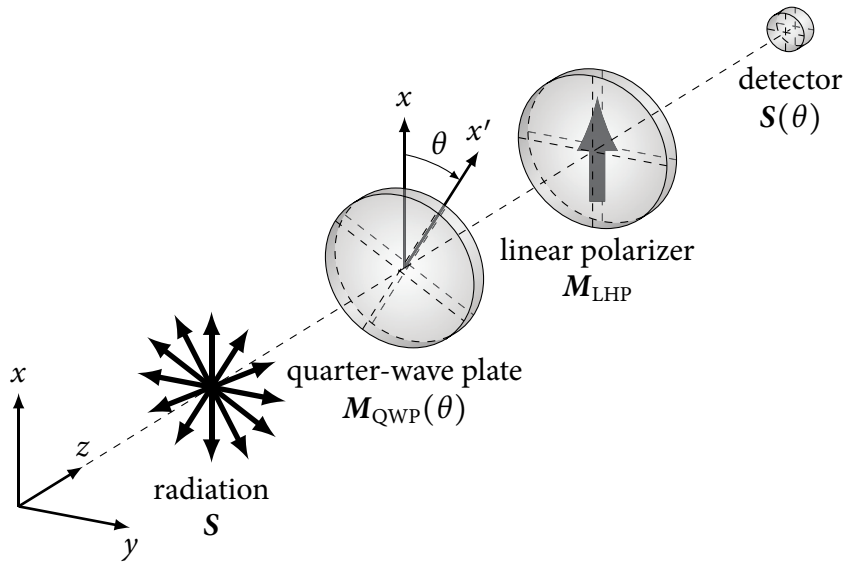

Figure B.1: Illustration of the rotating QWP polarimeter.

The resulting Müeller matrix of the rotated QWP is

$$\boldsymbol{M}_{\mathrm{QWP}}(\theta) = \begin{pmatrix} 1 & 0 & 0 & 0 \\ 0 & \cos^2 2\theta & \frac{1}{2}\sin 4\theta & -\sin 2\theta \\ 0 & \frac{1}{2}\sin 4\theta & \sin^2 2\theta & \cos 2\theta \\ 0 & \sin 2\theta & -\cos 2\theta & 0 \end{pmatrix}. \tag{B.4}$$

After passing through the rotated QWP, the beam arrives to an analyzer composed by a linear polarizer (LP) and a detector. The fast axis of the LP is oriented along the x-axis, and it can be described by the following matrix:

$$\boldsymbol{M}_{\mathrm{LHP}} = \begin{pmatrix} 1 & 1 & 0 & 0 \\ 1 & 1 & 0 & 0 \\ 0 & 0 & 0 & 0 \\ 0 & 0 & 0 & 0 \end{pmatrix}. \tag{B.5}$$

Finally, the Stokes vector $\boldsymbol{S}(\theta)$ of the signal transmitted by the LP and entering into the detector is given by

$$\boldsymbol{S}(\theta) = \boldsymbol{M}_{\mathrm{LHP}}\boldsymbol{M}_{\mathrm{QWP}}(\theta)\boldsymbol{S} = \begin{pmatrix} \frac{1}{2} & \frac{1}{4}(1+\cos 4\theta) & \frac{1}{4}\sin 4\theta & -\frac{1}{2}\sin 2\theta \\ \frac{1}{2} & \frac{1}{4}(1+\cos 4\theta) & \frac{1}{4}\sin 4\theta & -\frac{1}{2}\sin 2\theta \\ 0 & 0 & 0 & 0 \\ 0 & 0 & 0 & 0 \end{pmatrix} \boldsymbol{S}. \tag{B.6}$$

Therefore, the power $S_0(\theta)$ read by the detector is

$$S_0(\theta) = \frac{1}{2}S_0 + \frac{1}{4}S_1(1+\cos 4\theta) + \frac{1}{4}S_2 \sin 4\theta - \frac{1}{2}S_3 \sin 2\theta\,, \tag{B.7}$$

where $S_i, i \in \{0,1,2,3\}$ are the four components of the unknown input Stokes vector $\boldsymbol{S}$.

It can be noted that Eq. (B.7) represents a truncated Fourier series. By defining I_n as

$$I_n \overset{\text{def}}{=} S_0(\theta_n) = \frac{1}{2}S_0 + \frac{1}{4}S_1(1+\cos 4\theta_n) + \frac{1}{4}S_2 \sin 4\theta_n - \frac{1}{2}S_3 \sin 2\theta_n\,, \tag{B.8}$$

and by repeating its measurement for N different orientations θ_n of the QWP, the Stokes parameters S_i can be calculated as follows:

$$S_0 = \frac{2}{N}\sum_{n=1}^{N} I_n - \frac{4}{N}\sum_{n=1}^{N} I_n \cos 4\theta_n \,, \tag{B.9a}$$

$$S_1 = \frac{8}{N}\sum_{n=1}^{N} I_n \cos 4\theta_n \,, \tag{B.9b}$$

$$S_2 = \frac{8}{N}\sum_{n=1}^{N} I_n \sin 4\theta_n \,, \tag{B.9c}$$

$$S_3 = -\frac{4}{N}\sum_{n=1}^{N} I_n \sin 2\theta_n \,. \tag{B.9d}$$

Appendix C

Emulation of depolarized light

The degree of polarization (DOP) depends on the observation time-scale of the variation of the state of polarization (SOP), as seen in Appendix A.1. This means that measurements of DOP depends not only on the polarization properties of the light but also on the apparatus used to perform the measure. Hereinafter, fully depolarized light will means to have $\mathcal{D} = 0$ over a certain time interval, even if locally in time the light can have $\mathcal{D} = 1$.

Therefore, light depolarization can be attained in different ways, such as with broadband incoherent signals, with superposition of fully polarized signals or with signals whose SOP varies in time. In either case, $\mathcal{D} = 0$ is equivalent to have a uniform distribution of SOPs over the whole Poincaré sphere.

Polarization scramblers can be used, for example, for testing installed fiber optic links [178] or for evaluating the performance of coherent detection systems [179].

A uniform distribution of SOPs over the Poincaré sphere can be obtained by considering a Stokes vector

$$\boldsymbol{S} = \begin{pmatrix} S_1 \\ S_2 \\ S_3 \end{pmatrix} \tag{C.1}$$

whose components are independent and identically distributed Gaussian random variables. It can be shown [180]–[182] that the associated normalized vector

$$\hat{\boldsymbol{s}} = \begin{pmatrix} s_1 \\ s_2 \\ s_3 \end{pmatrix} = \frac{1}{\sqrt{S_1^2 + S_2^2 + S_3^2}} \begin{pmatrix} S_1 \\ S_2 \\ S_3 \end{pmatrix} \tag{C.2}$$

is uniformly distributed on the Poincaré sphere. In particular, this means that the components s_i are uniformly distributed random variables $\mathcal{U}(0, \sigma^2)$ between -1 and +1, with mean

$$\mathrm{E}[s_i] = 0 \qquad \text{for } i = 1, 2, 3\,, \tag{C.3}$$

and variance

$$\sigma_i^2 = \mathrm{E}[s_i^2] = \frac{1}{3} \qquad \text{for } i = 1, 2, 3\,. \tag{C.4}$$

However, the components s_i are not independent anymore, due to the way they are constructed (Eq. (C.2)). Under the above hypotheses, because $\hat{\boldsymbol{s}}$ has unitary modulus, the DOP is simply given by

$$\mathcal{D} = \sqrt{\langle s_1 \rangle^2 + \langle s_2 \rangle^2 + \langle s_3 \rangle^2}\,, \tag{C.5}$$

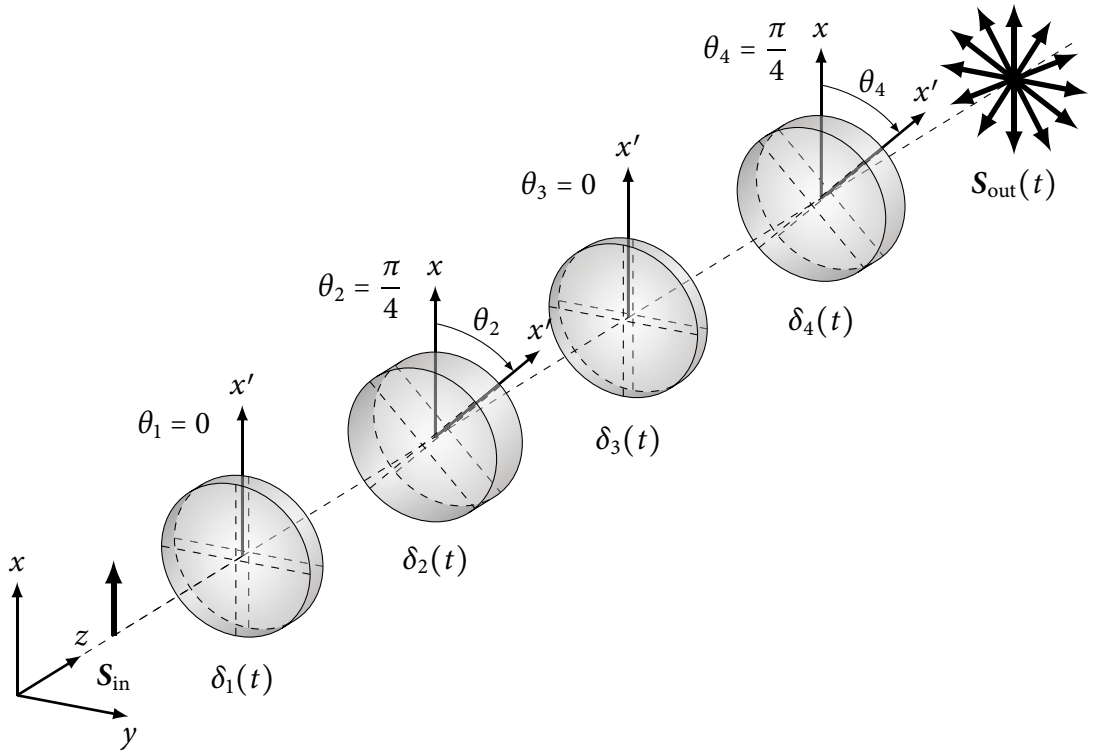

Figure C.1: Illustration of the polarization scrambler, based on four waveplates with variable delay δ and different axis orientations θ.

where

$$\langle \cdot \rangle = \int_0^T \cdot \, \mathrm{d}t \,. \tag{C.6}$$

Through Eq. (C.2), uniform SOPs distributions over the Poincaré sphere can be efficiently obtained numerically.

In Section 4.4, a polarization scrambler has been used to experimentally emulate depolarized light. The scrambler, depicted in Fig. C.1, is based on four fiber squeezers that can be modeled as waveplates with variable delay $\delta(t)$ [183]. Other scrambling techniques are based on electronic polarization controller [178], $LiNbO_3$ waveguides [144] or on a combination of $LiNbO_3$ waveguides and rotating waveplates [184].

Each waveplate, with variable delay $\delta = \delta(t)$ can be described by the following Müeller matrix:

$$\boldsymbol{M}_{\text{WP}}(\delta) = \begin{pmatrix} 1 & 0 & 0 & 0 \\ 0 & 1 & 0 & 0 \\ 0 & 0 & \cos\delta & \sin\delta \\ 0 & 0 & -\sin\delta & \cos\delta \end{pmatrix}. \tag{C.7}$$

As shown in Fig. C.1, two of the four waveplates have a rotation of $\theta = \pi/4$. The corresponding Müeller matrix can be obtained from Eq. (B.2), resulting in:

$$\boldsymbol{M}_{\text{WP}}(\delta, \theta) = \begin{pmatrix} 1 & 0 & 0 & 0 \\ 0 & \cos^2 2\theta + \cos\delta \sin^2 2\theta & \sin^2 \frac{\delta}{2} \sin 4\theta & -\sin\delta \sin 2\theta \\ 0 & \sin^2 \frac{\delta}{2} \sin 4\theta & \cos\delta \cos^2 2\theta + \sin^2 2\theta & \cos 2\theta \sin\delta \\ 0 & \sin\delta \sin 2\theta & -\cos 2\theta \sin\delta & \cos\delta \end{pmatrix}. \tag{C.8}$$

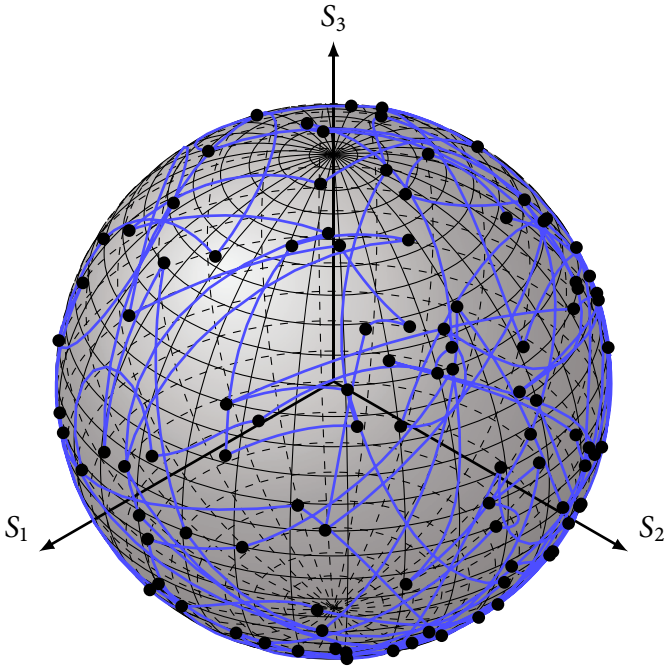

Figure C.2: Evolution of the SOP for $N = 100$ steps and for $\boldsymbol{S}_{\text{in}} = 3^{-1/2}(1,1,1)^T$.

The resulting SOP is therefore given by

$$\boldsymbol{S}_{\text{out}}(t) = \boldsymbol{M}_{\text{WP}}(\delta_4(t),\theta_4)\boldsymbol{M}_{\text{WP}}(\delta_3(t),\theta_3)\boldsymbol{M}_{\text{WP}}(\delta_2(t),\theta_2)\boldsymbol{M}_{\text{WP}}(\delta_1(t),\theta_1)\boldsymbol{S}_{\text{in}}\,. \qquad \text{(C.9)}$$

Actually, the four delays δ_i are driven by four statistically independent random signals, and the output SOP is randomly changed at a rate of $\Delta t^{-1} = 20\,\text{kHz}$. Fig. C.2 shows the evolution of the SOP for $N = 100$ random steps obtained by simulating the scrambler.

The DOP obtained by implementing the scrambler described above can be seen Fig. C.3, which shows repeated measurements of the DOP for different observation times T. The DOP is measured by using the rotating quarter-wave plate (QWP) polarimeter described in Appendix B and also used in Section 4.4, for $N_\theta = 5$ orientations of the QWP. As it can be seen, the value of the DOP depends on the observation time T. In particular, lower DOP is obtained by longer observation times. This is expected, and it can be explained by looking at Fig. C.4, which shows the mean and the variance of the components of the output Stokes vector as a function of the observation time T, obtained by simulating the system. As it can be seen, for long enough observation times the mean converge toward 0 and the variance toward 1/3, *i.e.* the sphere coverage is almost uniform, as explained before. For shorter observation times, instead, the statistics indicate that the sphere coverage is not uniform, and indeed the DOP is higher.

Finally, in Fig. C.5, the measured and the simulated average DOP $\langle \mathcal{D} \rangle$ are reported as a function of the normalized observation time $T' = T/N_\theta$, where N_θ is the number of orientations of the QWP in the polarimeter, *i.e.* the normalized observation time T' is the averaging time required by one QWP orientation. This makes sense since the rotating QWP estimates the DOP (and the SOP) by averaging over N_θ different time slots of duration $T' = T/N_\theta$.

The marks joined by the blue curve refer to the experimental data presented in Fig. C.3 with same marks. The black circles refer to the data presented in Fig. C.4. The same SOPs

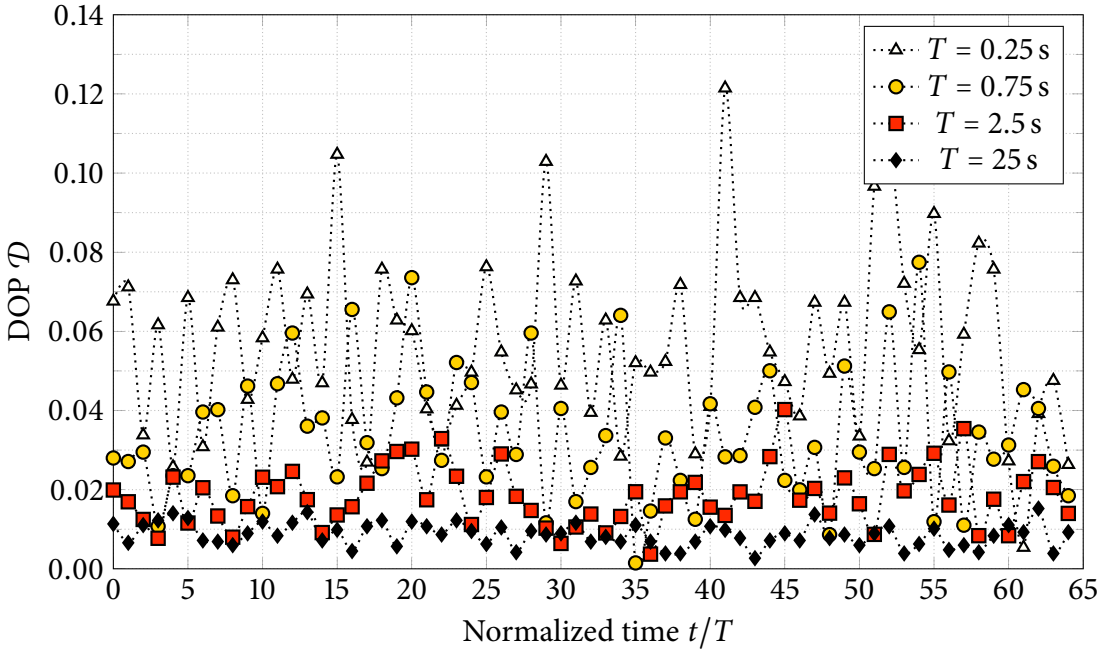

Figure C.3: Measured DOPs for various observation times T.

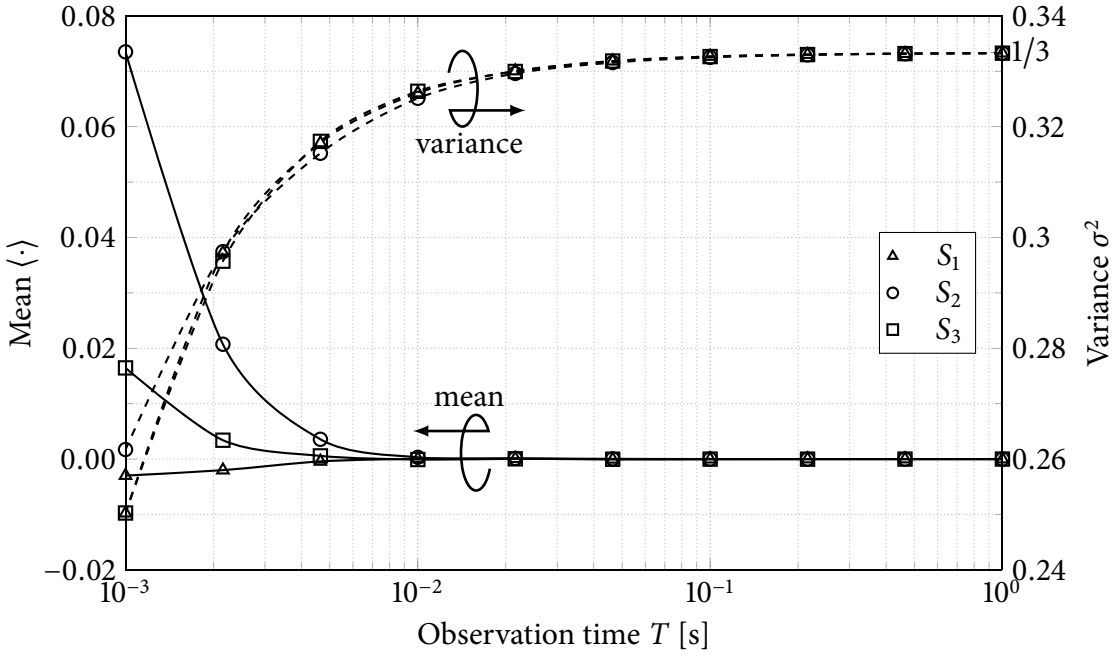

Figure C.4: Mean and variance of the Stokes components as a function of the observation time, calculated on $N = 1000$ realizations. The step duration is $\Delta t = 50\,\mu s$ and the input vector is $\boldsymbol{S}_{in} = 3^{-1/2}(1,1,1)^T$.

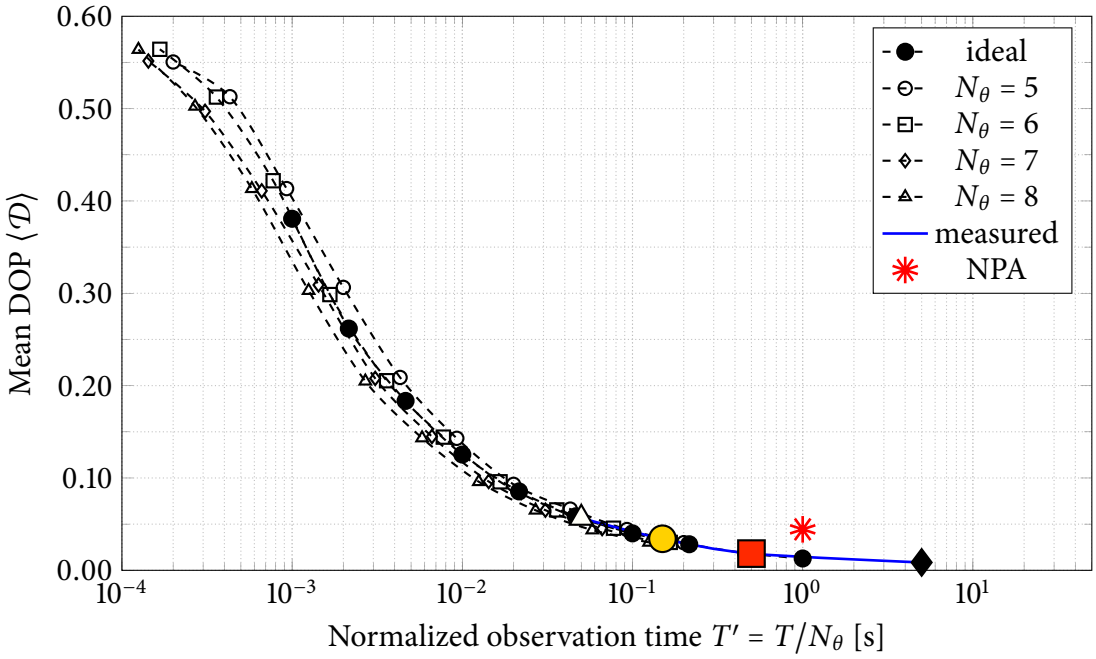

Figure C.5: Mean DOP $\langle \mathcal{D} \rangle$.

evolution is also used by simulating the rotating QWP polarimeter for different number of orientations N_θ, and the resulting mean DOP is shown with white marks joined by dashed curves. Also in this case, the observation time $T = T'/N_\theta$ of one QWP orientation has been considered. As it can be seen, the agreement between measured and simulated data is good. Therefore, to correctly emulate a low DOP by scrambling the SOP, the observation time T have to be carefully chosen. The red star is the mean DOP obtained from the data of the experiments on nonlinear polarization attraction (NPA) presented in Section 4.4. The difference with the data measured in Fig. C.3 might be attributed to some residual repolarization due to polarization-dependent losses (PDLs) [185] of the devices in the setup (see Fig. 4.11). However, for an observation time of $T' = 1\,\mathrm{s}$ a $\mathcal{D} < 5\%$ is achieved, which is usually considered the threshold for low polarization.

Appendix D

Polarization-mode dispersion

Polarization-mode dispersion (PMD) is one of the impairments limiting high bit-rate transmissions over long-haul fibers. The phenomenon origins from the random varying birefringence along the fiber.

An ideal isotropic single-mode fiber (SMF) has a structure with perfect cylindrical symmetry. In this condition there exists two orthogonal fundamental modes HE_{11}^{x} and HE_{11}^{y} [186] that are degenerate and that travel at the same group velocity. Therefore all state of polarizations (SOPs) propagate unaltered in the fiber.

However, real fibers exhibit geometrical imperfections and anisotropies due to the manufacturing process or induced by external stress, like bendings, twisting and pressure or temperature gradients. Apart from the case of spun fibers, where some control can be attained during the fabrication process, all these imperfections vary randomly both radially and along the propagation coordinate z. Even if these deformations are weak, their effect accumulates along the fiber and the net effect is to broke the degeneracy and to make the fiber birefringent. This means that a signal propagating into the fiber is projected onto two orthogonal SOPs that propagate with different group velocities. This determines the development of a phase shift between the two components and indeed a change in the SOP. Because of the stochastic nature of the birefringence variations, also the SOP of the signals vary randomly as they propagate.

From a practical point of view, PMD is responsible to for

1. a random evolution of the SOP of signals,

2. a delay between different SOPs, which travel at different speeds.

In the following Appendix D.1, a brief description of one of the models used to statistically describe the effects of PMD, called the random modulus model (RMM), is given. More in-depth treatises on PMD statistics and impacts on transmission links can be found, for instance, in Gordon and Kogelnik [172], Gordon [187] or Karlsson and Sunnerud [188].

D.1 The random modulus model

The random modulus model (RMM), proposed by Wai and Menyuk [160], is a model to describe the statistics of the random birefringence.

As depicted in Fig. D.1, the model divides the fiber into many short sections. Each section has a constant birefringence vector $\boldsymbol{\beta}$, which varies both in modulus and in direction

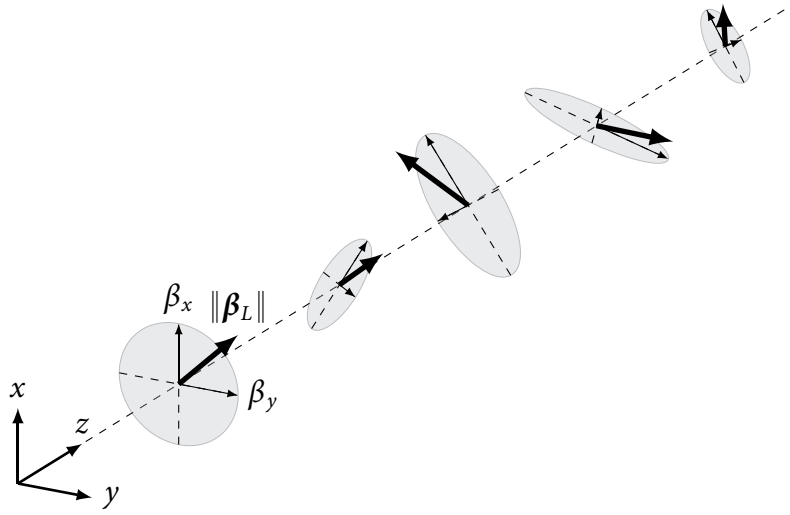

Figure D.1: Illustration of the RMM. The fiber is divided into many short sections, each having constant birefringence. The birefringence vector changes both in modulus and in direction when passing from one section to the next.

when passing from one section to the next. In the Stokes space, the birefringence vector $\boldsymbol{\beta}$ is described by

$$\boldsymbol{\beta} = \begin{pmatrix} \beta_1 \\ \beta_2 \\ 0 \end{pmatrix} \tag{D.1}$$

where $\beta_3 = 0$ has been assumed, *i.e.* no circular birefringence is present [157]–[161]. This assumption is justified because circular birefringence can be induced by twisting [157], [189], which is not the case of standard SMFs for telecommunications applications, or by exposition to very intense external magnetic fields [157].

The linear components $\beta_1(z)$ and $\beta_2(z)$ of the birefringence vector can be modeled as two independent Langevin processes [157], [160]:

$$\frac{\mathrm{d}\beta_i}{\mathrm{d}z} = -\rho\beta_i(z) + \sigma\eta_i(z) \qquad \text{for } i = 1, 2\,, \tag{D.2}$$

where $\eta_1(z)$ and $\eta_2(z)$ are statistically independent white Gaussian noises satisfying

$$\mathrm{E}[\eta_i(z)] = 0 \quad \text{and} \quad \mathrm{E}[\eta_i(u)\eta_i(z+u)] = \delta(z) \qquad \text{for } i = 1, 2\,. \tag{D.3}$$

It may also be shown that, under proper initial conditions, $\beta_1(z)$ and $\beta_2(z)$ are Gaussian distributed stationary processes [160] with zero mean

$$\mathrm{E}[\beta_i(z)] = 0 \tag{D.4}$$

and equal standard deviation σ_β given by

$$\mathrm{E}[\beta_i^2(z)] = \sigma_\beta^2 = \frac{\sigma^2}{2\rho}\,, \tag{D.5}$$

meaning that they have a bilateral exponential autocorrelation given by

$$r_\beta(z) = \mathrm{E}[\beta_i(u)\beta_i(z+u)] = \sigma_\beta^2\,\mathrm{e}^{-\rho|z|} \qquad \text{for } i = 1, 2\,. \tag{D.6}$$

Under these assumptions, the modulus of the linear birefringence

$$\beta_L = \|\boldsymbol{\beta}_L(z)\| = \left\|\left(\beta_1(z), \beta_2(z)\right)^T\right\| \tag{D.7}$$

is a Rayleigh random variable[1].

The parameters ρ and σ can be related to physical measurable quantities. They are related to the beat length L_B. In the Jones space, the birefringence can be described by considering the modulus Δn of the difference of the refractive indexes n_x and n_y of the two orthogonal modes, defined as [186]:

$$\Delta n = \left|n_x - n_y\right| = \frac{2\pi\left|\beta_x - \beta_y\right|}{\lambda}\,, \tag{D.9}$$

where β_x and β_y are the respective propagation constants and λ is the wavelength. The axis with the smallest group index has the highest group velocity and it is therefore called the fast axis, while the other is called the slow axis.

The beat length describes the distance required for the two modes to develop a phase shift of 2π, *i.e.* it defines the spatial periodicity of the evolution of the SOP, and is defined as [186]:

$$L_B = \frac{2\pi}{\left|\beta_x - \beta_y\right|} = \frac{\lambda}{\Delta n}\,. \tag{D.10}$$

The beat length is related to ρ and σ by the following relation:

$$L_B = \frac{2\pi}{\sqrt{\mathrm{E}[\beta_L^2]}} = 2\pi\frac{\sqrt{\rho}}{\sigma}\,, \tag{D.11}$$

i.e. the beat length is inversely proportional to the root mean square (RMS) of the modulus of the linear birefringence. Typical values of the beat length L_B are in the range from 10 m to 20 m for standard SMFs [158], [159].

The parameter ρ is also related to the correlation length [160], [191] by

$$L_C = \frac{1}{\rho}\,, \tag{D.12}$$

which is the distance over which Eq. (D.6) decays to e^{-1} of its maximum σ_β^2. Typical values of the correlation length L_C for standard SMFs are in the range from 5 m to 25 m [158], [159], [192].

Finally, L_B and L_C are related to the differential group delay (DGD) by [160]:

$$\langle\Delta\tau\rangle^2 = \frac{1}{3}\left(\frac{8\lambda L_C}{\pi c L_B}\right)^2\left(\mathrm{e}^{-L/L_c} + \frac{L}{L_c} - 1\right), \tag{D.13}$$

from which the PMD coefficient (PMDc) is estimated as:

$$D_P = \sqrt{\frac{\langle\Delta\tau\rangle^2}{L}}\,, \tag{D.14}$$

[1]The probability density function of the Rayleigh distribution with parameter σ is given by [190]:

$$p(x;\sigma) = \frac{x}{\sigma^2}\,\mathrm{e}^{-x^2/(2\sigma^2)} \quad , \quad x \geq 0\,. \tag{D.8}$$

where L is the fiber length.

However, the RMS of the group delay $\langle \Delta\tau^2 \rangle$ is often measured in practice, and the two are related by [187]:

$$\langle \Delta\tau \rangle^2 = \frac{8}{3\pi} \langle \Delta\tau^2 \rangle . \tag{D.15}$$

As it can be seen, the two definitions give approximately the same value.

Appendix E

Numerical integration of boundary value problems

This appendix delineates the numerical methods used to integrate the equations governing the evolution of the Stokes vectors of the pump $\boldsymbol{P}$ and of the signal $\boldsymbol{S}$ in a counter-propagating fiber Raman amplifier (FRA). In Section 4.2 the following equations have been presented:

$$\frac{\mathrm{d}\boldsymbol{S}}{\mathrm{d}z} = -\alpha_s \boldsymbol{S} + \frac{g_\mathrm{R}}{2}\Big[P_0\boldsymbol{S} + S_0\boldsymbol{P} + \mu\big(3P_0\boldsymbol{S} + S_0\boldsymbol{P} - 2S_0\boldsymbol{P}_3\big)\Big] + \big(\omega_s\boldsymbol{b} + \boldsymbol{W}_s\big)\times\boldsymbol{S}\,,$$

(Eq. (4.3a) revisited.)

$$\frac{\mathrm{d}\boldsymbol{P}}{\mathrm{d}z} = \alpha_p \boldsymbol{P} + \frac{\omega_p}{\omega_s}\frac{g_\mathrm{R}}{2}\Big[S_0\boldsymbol{P} + P_0\boldsymbol{S} + \mu\big(3S_0\boldsymbol{P} + P_0\boldsymbol{S} - 2P_0\boldsymbol{S}_3\big)\Big] - \big(\boldsymbol{M}\omega_p\boldsymbol{b} + \boldsymbol{W}_p\big)\times\boldsymbol{P}\,.$$

(Eq. (4.3b) revisited.)

This is a system of nonlinear first-order ordinary differential equations (ODEs). The initial value problem (IVP) associated with this system can not be solved in closed form, and a numerical approach is required. Moreover, the associated boundary conditions given by Eqs. 4.8:

$$\boldsymbol{S}(z=0) = \boldsymbol{S}^\mathrm{in}\,, \qquad \text{(Eq. (4.8a) revisited.)}$$

$$\boldsymbol{P}(z=L) = \boldsymbol{P}^\mathrm{in}\,, \qquad \text{(Eq. (4.8b) revisited.)}$$

render the system a boundary value problem (BVP). Generally, BVPs can be transformed into optimization problems and therefore they can be numerically solved by finding some root.

In the following Appendix E.1 the fourth-order Runge-Kutta (RK4) method is presented. The RK4 has been used in Chapter 4 to integrate the IVP associated with Eqs. 4.3. In Appendix E.2, instead, the shooting algorithm used to solve the BVP is described.

More in-depth and precise mathematical discussions can be found in the cited references.

E.1 The Runge-Kutta method

The general form of a first-order ODE system can be written as [193], [194]

$$\frac{\mathrm{d}\boldsymbol{y}}{\mathrm{d}x} = \boldsymbol{f}(x, \boldsymbol{y}(x))\,, \quad a \le x \le b\,, \tag{E.3}$$

where x is the independent variable, $\boldsymbol{y} = (y_1, y_2, \ldots, y_n)^T$ is the vector of unknowns and $\boldsymbol{f} = (f_1(x, \boldsymbol{y}(x)), f_2(x, \boldsymbol{y}(x)), \ldots, f_n(x, \boldsymbol{y}(x)))^T$ is a vector of functions. In the general case the functions in $\boldsymbol{f}$ are nonlinear.

The system of Eq. (E.3) together with the initial conditions

$$\boldsymbol{y}(a) = \boldsymbol{y}_0\,, \tag{E.4}$$

is an IVP.

The Runge-Kutta (RK) integration scheme is an algorithm to integrate IVPs that can be applied to a broad range of different problems, and it is usually known to be very accurate. The RK method divides the integration interval $[a, b]$ into N steps of size h. At each step an approximated value of the function is calculated.

In particular, the fourth-order Runge-Kutta (RK4) [162], [193]–[196] is based on four evaluations of the function being integrated for each integration step. The four evaluations, also called stages, are given by:

$$\boldsymbol{k}_1 = h\boldsymbol{f}\left(\boldsymbol{x}_n, \boldsymbol{y}_n\right) \tag{E.5a}$$

$$\boldsymbol{k}_2 = h\boldsymbol{f}\left(\boldsymbol{x}_n + \frac{1}{2}h, \boldsymbol{y}_n + \frac{1}{2}\boldsymbol{k}_1\right) \tag{E.5b}$$

$$\boldsymbol{k}_3 = h\boldsymbol{f}\left(\boldsymbol{x}_n + \frac{1}{2}h, \boldsymbol{y}_n + \frac{1}{2}\boldsymbol{k}_2\right) \tag{E.5c}$$

$$\boldsymbol{k}_4 = h\boldsymbol{f}\left(\boldsymbol{x}_n + h, \boldsymbol{y}_n + \boldsymbol{k}_3\right). \tag{E.5d}$$

The estimated value at step $n + 1$ is calculated as

$$\boldsymbol{y}_{n+1} = \boldsymbol{y}_n + \frac{1}{6}(\boldsymbol{k}_1 + 2\boldsymbol{k}_2 + 2\boldsymbol{k}_3 + \boldsymbol{k}_4) + O(h^5)\,, \tag{E.6}$$

where O is the Landau symbol. The value of $\boldsymbol{y}(x_{n+1})$ is given by the approximation $\boldsymbol{y}_{n+1}$, which is based on the previous step $\boldsymbol{y}_n$ and a weighted average of the intermediate values $\boldsymbol{k}_1, \boldsymbol{k}_2, \boldsymbol{k}_3, \boldsymbol{k}_4$. Each step introduces a truncation error of order $O(h^5)$. However, the overall error has order $O(h^4)$, from which the name "fourth-order".

E.2 Solution of boundary value problems

The shooting method [162], [193], [194], [196] reduces a BVP into an optimization problem involving only an IVP. This is accomplished by adding to the system of Eq. (E.3) the following equation

$$g(\boldsymbol{y}(a), \boldsymbol{y}(b)) = 0\,. \tag{E.7}$$

Intuitively, this method is equivalent to iterate on the fictitious initial conditions in a until the true initial conditions in b are satisfied.

The function g to be minimized can vary. For the analysis of Chapter 4, it has been chosen to minimize the following error

$$\varepsilon = \frac{\|\Delta \boldsymbol{S}\|}{S_0^{\text{in}}}\,, \tag{E.8}$$

where $S_0^{\text{in}} = \|\boldsymbol{S}^{\text{in}}\|$ and $\Delta\boldsymbol{S} = \boldsymbol{S}^{\text{out}} - \boldsymbol{S}^{\text{in}}$. The nonlinear minimization algorithm guaranteed

$$\varepsilon < 10^{-2} \tag{E.9}$$

while preserving the input degree of polarization (DOP) and the power.

List of publications

Peer-reviewed international journals

[P.1] **F. Chiarello**, L. Palmieri, A. Galtarossa, and M. Santagiustina, "Widely time-dispersion-tuned fiber optical oscillator and frequency comb based on multiple nonlinear processes", *Optics Letters*, vol. 38, no. 22, pp. 4621–4624, Nov. 2013. DOI: 10.1364/OL.38.004621.

[P.2] **F. Chiarello**, L. Palmieri, M. Santagiustina, R. Gamatham, and A. Galtarossa, "Experimental characterization of the counter-propagating Raman polarization attraction", *Optics Express*, vol. 20, no. 23, pp. 26 050–26 055, Nov. 2012. DOI: 10.1364/OE.20.026050.

[P.3] **F. Chiarello**, L. Ursini, L. Palmieri, and M. Santagiustina, "Polarization attraction in counterpropagating fiber Raman amplifiers", *Photonics Technology Letters*, vol. 23, no. 20, pp. 1457–1459, Oct. 15, 2011. DOI: 10.1109/LPT.2011.2163061.

[P.4] **F. Chiarello**, L. Ursini, and M. Santagiustina, "Securing wireless infrared communications through optical chaos", *Photonics Technology Letters*, vol. 23, no. 9, pp. 564–566, May 1, 2011. DOI: 10.1109/LPT.2011.2114334.

Conference proceedings

[C.1] **F. Chiarello**, L. Palmieri, A. Galtarossa, and M. Santagiustina, "Nonlinear multi-process fiber laser widely tunable through time-dispersion tuning (invited)", in *Fotonica 2013, 15° Convegno Nazionale delle Tecnologie Fotoniche*, (May 21–23, 2013), Milano, Italy, 2013, p. C4.1.

[C.2] **F. Chiarello**, L. Ursini, L. Palmieri, M. Santagiustina, A. W. R. Leitch, and M. Guglielmucci, "Polarization attraction in counter-propagating fiber Raman amplifiers", in *Fotonica 2011, 13° Convegno Nazionale delle Tecnologie Fotoniche*, (May 9–11, 2011), Genova, Italy, 2011, p. C4.3.

[C.3] M. Santagiustina, L. Ursini, A. Galtarossa, **F. Chiarello**, L. Palmieri, C. G. Someda, L. Thévenaz, and A. Leitch, "Microwave photonic notch filter based on dynamic Brillouin gratings generated by PRBS signals", in *Fotonica 2012, 14° Convegno Nazionale delle Tecnologie Fotoniche*, (May 15–17, 2012), Firenze, Italy, 2012, B3.4.

[C.4] L. Schenato, G. Marcato, A. Pasuto, L. Palmieri, **F. Chiarello**, A. Galtarossa, G. Gruca, T. van de Watering, and D. Iannuzzi, "Experimental analysis of fiber optic sensor for detection of precursory acoustic signals in rockfall events", in *Fotonica 2012, 14° Convegno Nazionale delle Tecnologie Fotoniche*, (May 15–17, 2012), Firenze, Italy, 2012, B6.5.

[C.5] M. Santagiustina, L. Ursini, L. Palmieri, **F. Chiarello**, and M. Bosiljevac, "Dynamic Brillouin gratings permanently induced by chaotic signals for sensing applications", in *Fotonica 2011, 13° Convegno Nazionale delle Tecnologie Fotoniche*, (May 9–11, 2011), Genova, Italy, 2011, B6.6.

[C.6] **F. Chiarello**, M. Santagiustina, and L. Ursini, "Securing free space optics communications through optical chaos", in *Access Networks and In-house Communications*, (Jun. 12–14, 2011), Toronto, Canada: OSA, 2011, ATuC5.

[C.7] L. Ursini, **F. Chiarello**, M. Santagiustina, and L. Schenato, "Comunicazioni sicure in spazio libero su portante ottica caotica", in *Fotonica 2010, 12° Convegno Nazionale delle Tecnologie Fotoniche*, (May 25–27, 2010), Pisa, Italy, 2010, P1.5.

References

[1] K. C. Kao and G. A. Hockham, "Dielectric-fibre surface waveguides for optical frequencies", *Proceedings of the Institution of Electrical Engineers*, vol. 113, no. 7, pp. 1151–1158, 1966. DOI: 10.1049/piee.1966.0189.

[2] F. P. Kapron, D. B. Keck, and R. D. Maurer, "Radiation losses in glass optical waveguides", *Applied Physics Letters*, vol. 17, no. 10, pp. 423–425, Nov. 1970. DOI: 10.1063/1.1653255.

[3] D. B. Keck, R. D. Maurer, and P. C. Schultz, "On the ultimate lower limit of attenuation in glass optical waveguides", *Applied Physics Letters*, vol. 22, no. 7, pp. 307–309, Apr. 1973. DOI: 10.1063/1.1654649.

[4] Y. Takubo and S. Yamashita, "In vivo OCT imaging using wavelength-swept fiber laser based on dispersion tuning", *Photonics Technology Letters*, vol. 24, no. 12, pp. 979–981, Jun. 2012. DOI: 10.1109/LPT.2012.2190503.

[5] S. H. Yun, D. J. Richardson, and B. Y. Kim, "Interrogation of fiber grating sensor arrays with a wavelength-swept fiber laser", *Optics Letters*, vol. 23, no. 11, pp. 843–845, Jun. 1998. DOI: 10.1364/OL.23.000843.

[6] V. Bertogalli, E. U. Wagemann, E. Miller, and E. Leckel, "Testing passive DWDM components: uncertainties in swept-wavelength measurement systems", in *Optical Fiber Communication Conference and Exhibit (OFC)*, (Mar. 17–22, 2001), vol. 4, Anaheim, CA, USA, Mar. 2001, ThB6.

[7] X. Yang, K. Xu, J. Yin, Y. Dai, F. Yin, J. Li, H. Lu, T. Liu, and Y. Ji, "Optical frequency comb based multi-band microwave frequency conversion for satellite applications", *Optics Express*, vol. 22, no. 1, pp. 869–877, Jan. 2014. DOI: 10.1364/OE.22.000869.

[8] M. Ziyadi, M. R. Chitgarha, S. Khaleghi, A. Mohajerin-Ariaei, A. Almaiman, J. Touch, M. Tur, C. Langrock, M. M. Fejer, and A. E. Willner, "Tunable optical correlator using an optical frequency comb and a nonlinear multiplexer", *Optics Express*, vol. 22, no. 1, pp. 84–89, Jan. 2014. DOI: 10.1364/OE.22.000084.

[9] S. T. Cundiff and J. Ye, "Colloquium: femtosecond optical frequency combs", *Reviews of Modern Physics*, vol. 75, no. 1, pp. 325–342, Mar. 2003. DOI: 10.1103/RevModPhys.75.325.

[10] N. R. Newbury, "Searching for applications with a fine-tooth comb", *Nature Photonics*, vol. 5, no. 4, pp. 186–188, Apr. 2011. DOI: 10.1038/nphoton.2011.38.

[11] Y. Silberberg, "Physical chemistry: combs for molecules", *Nature*, vol. 502, no. 7471, pp. 307–308, Oct. 2013. DOI: 10.1038/502307a.

[12] P. Del'Haye, T. Herr, E. Gavartin, M. L. Gorodetsky, R. Holzwarth, and T. J. Kippenberg, "Octave spanning tunable frequency comb from a microresonator", *Physical Review Letters*, vol. 107, no. 6, p. 063 901, Aug. 2011. DOI: 10.1103/PhysRevLett.107.063901.

[13] N. A. Cholan, M. H. Al-Mansoori, A. S. M. Noor, A. Ismail, and M. A. Mahdi, "Multi-wavelength generation by self-seeded four-wave mixing", *Optics Express*, vol. 21, no. 5, pp. 6131–6138, Mar. 2013. DOI: 10.1364/OE.21.006131.

[14] M. Tadakuma, O. Aso, and S. Namiki, "A 104 GHz 328 fs soliton pulse train generation through a comb-like dispersion profiled fiber using short high nonlinearity dispersion fibers", in *Optical Fiber Communication Conference (OFC)*, (Mar. 7–10, 2000), vol. 3, Baltimore, MD, USA, 2000, pp. 178–180. DOI: 10.1109/OFC.2000.868557.

[15] A. Cerqueira Sodre, J. M. Chavez Boggio, A. A. Rieznik, H. E. Hernandez-Figueroa, H. L. Fragnito, and J. C. Knight, "Highly efficient generation of broadband cascaded four-wave mixing products", *Optics Express*, vol. 16, no. 4, pp. 2816–2828, Feb. 2008. DOI: 10.1364/OE.16.002816.

[16] F. C. Cruz, "Optical frequency combs generated by four-wave mixing in optical fibers for astrophysical spectrometer calibration and metrology", *Optics Express*, vol. 16, no. 17, pp. 13 267–13 275, Aug. 2008. DOI: 10.1364/OE.16.013267.

[17] J. E. Heebner, R. S. Bennink, R. W. Boyd, and R. A. Fisher, "Conversion of unpolarized light to polarized light with greater than 50% efficiency by photorefractive two-beam coupling", *Optics Letters*, vol. 25, no. 4, pp. 257–259, Feb. 2000. DOI: 10.1364/OL.25.000257.

[18] M. Martinelli, M. Cirigliano, M. Ferrario, L. Marazzi, and P. Martelli, "Evidence of Raman-induced polarization pulling", *Optics Express*, vol. 17, no. 2, pp. 947–955, 2009. DOI: 10.1364/OE.17.000947.

[19] A. Galtarossa, L. Palmieri, M. Santagiustina, and L. Ursini, "Polarized backward Raman amplification in randomly birefringent fibers", *Journal of Lightwave Technology*, vol. 24, no. 11, pp. 4055–4063, Nov. 2006. DOI: 10.1109/JLT.2006.883640.

[20] M. Ferrario, V. Gilardone, P. Martelli, L. Marazzi, and M. Martinelli, "Effective all-optical polarization control induced by Raman nonlinear amplification", in *36th European Conference and Exhibition on Optical Communication (ECOC)*, (Sep. 19–23, 2010), Torino, Italy, 2010, P1.19. DOI: 10.1109/ECOC.2010.5621415.

[21] V. V. Kozlov, J. Nuño, J. D. Ania-Castañón, and S. Wabnitz, "Theory of fiber optic Raman polarizers", *Optics Letters*, vol. 35, no. 23, pp. 3970–3972, Dec. 2010. DOI: 10.1364/OL.35.003970.

[22] L. Ursini, M. Santagiustina, and L. Palmieri, "Raman nonlinear polarization pulling in the pump depleted regime in randomly birefringent fibers", *Photonics Technology Letters*, vol. 23, no. 4, pp. 254–256, Feb. 2011. DOI: 10.1109/LPT.2010.2098024.

[23] S. V. Sergeyev, "Activated polarization pulling and de-correlation of signal and pump states of polarization in a fiber Raman amplifier", *Optics Express*, vol. 19, no. 24, pp. 24 268–24 279, 2011. DOI: 10.1364/OE.19.024268.

[24] V. V. Kozlov, J. Nuño, J. D. Ania-Castañón, and S. Wabnitz, "Theoretical study of optical fiber Raman polarizers with counterpropagating beams", *Journal of Lightwave Technology*, vol. 29, no. 3, pp. 341–347, Feb. 2011. DOI: 10.1109/JLT.2010.2099644.

[25] N. J. Muga, M. F. S. Ferreira, and A. N. Pinto, "Broadband polarization pulling using Raman amplification", *Optics Express*, vol. 19, no. 19, pp. 18 707–18 712, Sep. 2011. DOI: 10.1364/OE.19.018707.

[26] V. V. Kozlov, J. Nuño, J. D. Ania-Castañón, and S. Wabnitz, "Multichannel Raman polarizer with suppressed relative intensity noise for wavelength division multiplexing transmission lines", *Optics Letters*, vol. 37, no. 11, pp. 2073–2075, 2012. DOI: 10.1364/OL.37.002073.

[27] V. V. Kozlov and S. Wabnitz, "Silicon Raman polarizer", *Optics Letters*, vol. 37, no. 4, pp. 737–739, 2012. DOI: 10.1364/OL.37.000737.

[28] S. Sergeyev and S. Popov, "Two-section fiber optic Raman polarizer", *Journal of Quantum Electronics*, vol. 48, no. 1, pp. 56–60, Jan. 2012. DOI: 10.1109/JQE.2011.2177073.

[29] V. V. Kozlov, J. Nuño, J. D. Ania-Castañón, and S. Wabnitz, "Trapping polarization of light in nonlinear optical fibers: an ideal Raman polarizer", in *Spontaneous Symmetry Breaking, Self-Trapping, and Josephson Oscillations*, ser. Progress in Optical Science and Photonics, B. A. Malomed, Ed., vol. 1, Springer Berlin Heidelberg, Jan. 2012, pp. 227–246. DOI: 10.1007/10091_2012_8.

[30] P. Morin, S. Pitois, and J. Fatome, "Simultaneous polarization attraction and Raman amplification of a light beam in optical fibers", *Journal of the Optical Society of America B*, vol. 29, no. 8, pp. 2046–2052, 2012. DOI: 10.1364/JOSAB.29.002046.

[31] A. Zadok, E. Zilka, A. Eyal, L. Thévenaz, and M. Tur, "Vector analysis of stimulated Brillouin scattering amplification in standard single-mode fibers", *Optics Express*, vol. 16, no. 26, pp. 21 692–21 707, Dec. 2008. DOI: 10.1364/OE.16.021692.

[32] J. Fatome, S. Pitois, and G. Millot, "Experimental evidence of Brillouin-induced polarization wheeling in highly birefringent optical fibers", *Optics Express*, vol. 17, no. 15, pp. 12 612–12 618, 2009. DOI: 10.1364/OE.17.012612.

[33] L. Ursini, M. Santagiustina, and L. Palmieri, "Polarization-dependent Brillouin gain in randomly birefringent fibers", *Photonics Technology Letters*, vol. 22, no. 10, pp. 712–714, May 2010. DOI: 10.1109/LPT.2010.2044655.

[34] Z. Shmilovitch, N. Primerov, A. Zadok, A. Eyal, S. Chin, L. Thévenaz, and M. Tur, "Dual-pump push-pull polarization control using stimulated Brillouin scattering", *Optics Express*, vol. 19, no. 27, pp. 25 873–25 880, Dec. 2011. DOI: 10.1364/OE.19.025873.

[35] S. Pitois, A. Sauter, and G. Millot, "Simultaneous achievement of polarization attraction and Raman amplification in isotropic optical fibers", *Optics Letters*, vol. 29, no. 6, pp. 599–601, 2004. DOI: 10.1364/OL.29.000599.

[36] S. Pitois, J. Fatome, and G. Millot, "Polarization attraction using counter-propagating waves in optical fiber at telecommunication wavelengths", *Optics Express*, vol. 16, no. 9, pp. 6646–6651, Apr. 2008. DOI: 10.1364/OE.16.006646.

[37] J. Fatome, S. Pitois, P. Morin, and G. Millot, "Observation of light-by-light polarization control and stabilization in optical fibre for telecommunication applications", *Optics Express*, vol. 18, no. 15, pp. 15 311–15 317, Jul. 2010. DOI: 10.1364/OE.18.015311.

[38] P. Morin, J. Fatome, C. Finot, S. Pitois, R. Claveau, and G. Millot, "All-optical nonlinear processing of both polarization state and intensity profile for 40 Gbit/s regeneration applications", *Optics Express*, vol. 19, no. 18, pp. 17 158–17 166, 2011. DOI: 10.1364/OE.19.017158.

[39] J. Fatome, P. Morin, S. Pitois, and G. Millot, "Light-by-light polarization control of 10-Gb/s RZ and NRZ telecommunication signals", *Journal of Selected Topics in Quantum Electronics*, vol. 18, no. 2, pp. 621–628, 2012. DOI: 10.1109/JSTQE.2011.2119467.

[40] E. Assémat, S. Lagrange, A. Picozzi, H. R. Jauslin, and D. Sugny, "Complete nonlinear polarization control in an optical fiber system", *Optics Letters*, vol. 35, no. 12, pp. 2025–2027, Jun. 2010. DOI: 10.1364/OL.35.002025.

[41] J. Fatome, S. Pitois, P. Morin, E. Assémat, D. Sugny, A. Picozzi, H. R. Jauslin, G. Millot, V. V. Kozlov, and S. Wabnitz, "A universal optical all-fiber omnipolarizer", *Scientific Reports*, vol. 2, Dec. 2012. DOI: 10.1038/srep00938.

[42] M. Guasoni, V. V. Kozlov, and S. Wabnitz, "Theory of polarization attraction in parametric amplifiers based on telecommunication fibers", *Journal of the Optical Society of America B*, vol. 29, no. 10, pp. 2710–2720, Oct. 2012. DOI: 10.1364/JOSAB.29.002710.

[43] V. V. Kozlov, K. Turitsyn, and S. Wabnitz, "Nonlinear repolarization in optical fibers: polarization attraction with copropagating beams", *Optics Letters*, vol. 36, no. 20, pp. 4050–4052, Oct. 2011. DOI: 10.1364/OL.36.004050.

[44] V. V. Kozlov, J. Nuño, and S. Wabnitz, "Theory of lossless polarization attraction in telecommunication fibers", *Journal of the Optical Society of America B*, vol. 28, no. 1, pp. 100–108, Jan. 2011. DOI: 10.1364/JOSAB.28.000100.

[45] V. V. Kozlov and S. Wabnitz, "Theoretical study of polarization attraction in high-birefringence and spun fibers", *Optics Letters*, vol. 35, no. 23, pp. 3949–3951, Dec. 2010. DOI: 10.1364/OL.35.003949.

[46] K. Rottwitt, J. Bromage, A. J. Stentz, L. Leng, M. E. Lines, and H. Smith, "Scaling of the Raman gain coefficient: applications to germanosilicate fibers", *Journal of Lightwave Technology*, vol. 21, no. 7, pp. 1652–1662, 2003. DOI: 10.1109/JLT.2003.814386.

[47] M. Buchanan, "Thesis: past the Schwinger limit", *Nature Physics*, vol. 2, no. 11, pp. 721–721, Nov. 2006. DOI: 10.1038/nphys448.

[48] E. G. Sauter, *Nonlinear Optics*, K. Chang, Ed., ser. Microwave and optical engineering. John Wiley & Sons, Sep. 1996.

[49] R. W. Boyd, *Nonlinear optics*. Academic Press, 2008.

[50] G. P. Agrawal, *Nonlinear Fiber Optics*, 4th ed., ser. Optics and Photonics. Elsevier Academic Press, Oct. 2007.

[51] M. E. Marhic, *Fiber Optical Parametric Amplifiers, Oscillators and Related Devices*. Cambridge University Press, 2008.

[52] C. Headley and G. Agrawal, Eds., *Raman Amplification in Fiber Optical Communication Systems*, 1st ed., ser. Optics and Photonics. Elsevier Academic Press, Dec. 2005.

[53] R. G. Smith, "Optical power handling capacity of low loss optical fibers as determined by stimulated Raman and Brillouin scattering", *Applied Optics*, vol. 11, no. 11, pp. 2489–2494, Nov. 1972. DOI: 10.1364/AO.11.002489.

[54] J. Toulouse, "Optical nonlinearities in fibers: review, recent examples, and systems applications", *Journal of Lightwave Technology*, vol. 23, no. 11, pp. 3625–3641, Nov. 2005. DOI: 10.1109/JLT.2005.855877.

[55] R. H. Stolen, C. Lee, and R. K. Jain, "Development of the stimulated Raman spectrum in single-mode silica fibers", *Journal of the Optical Society of America B*, vol. 1, no. 4, pp. 652–657, Aug. 1984. DOI: 10.1364/JOSAB.1.000652.

[56] M. N. Islam, "Raman amplifiers for telecommunications", *Journal of Selected Topics in Quantum Electronics*, vol. 8, no. 3, pp. 548–559, Jun. 2002. DOI: 10.1109/JSTQE.2002.1016358.

[57] C. Headley III and G. P. Agrawal, "Simultaneous amplification and compression of picosecond optical pulses during Raman amplification in optical fibers", *Journal of the Optical Society of America B*, vol. 10, no. 12, pp. 2383–2389, Dec. 1993. DOI: 10.1364/JOSAB.10.002383.

[58] J. P. Gordon, "Theory of the soliton self-frequency shift", *Optics Letters*, vol. 11, no. 10, pp. 662–664, Oct. 1986. DOI: 10.1364/OL.11.000662.

[59] C. Headley III and G. P. Agrawal, "Unified description of ultrafast stimulated Raman scattering in optical fibers", *Journal of the Optical Society of America B*, vol. 13, no. 10, pp. 2170–2177, Oct. 1996. DOI: 10.1364/JOSAB.13.002170.

[60] R. H. Stolen and J. E. Bjorkholm, "Parametric amplification and frequency conversion in optical fibers", *Journal of Quantum Electronics*, vol. 18, no. 7, pp. 1062–1072, 1982. DOI: 10.1109/JQE.1982.1071660.

[61] G. Cappellini and S. Trillo, "Third-order three-wave mixing in single-mode fibers: exact solutions and spatial instability effects", *Journal of the Optical Society of America B*, vol. 8, no. 4, pp. 824–838, Apr. 1991. DOI: 10.1364/JOSAB.8.000824.

[62] M. E. Marhic, K. K. Y. Wong, and L. G. Kazovsky, "Fiber optical parametric amplifiers with linearly or circularly polarized waves", *Journal of the Optical Society of America B*, vol. 20, no. 12, pp. 2425–2433, Dec. 2003. DOI: 10.1364/JOSAB.20.002425.

[63] C. J. McKinstrie and S. Radic, "Phase-sensitive amplification in a fiber", *Optics Express*, vol. 12, no. 20, pp. 4973–4979, Oct. 2004. DOI: 10.1364/OPEX.12.004973.

[64] M. E. Marhic, K. K.-Y. Wong, and L. G. Kazovsky, "Wide-band tuning of the gain spectra of one-pump fiber optical parametric amplifiers", *Journal of Selected Topics in Quantum Electronics*, vol. 10, no. 5, pp. 1133–1141, Oct. 2004. DOI: 10.1109/JSTQE.2004.835298.

[65] M. E. Marhic, N. Kagi, T.-K. Chiang, and L. G. Kazovsky, "Broadband fiber optical parametric amplifiers", *Optics Letters*, vol. 21, no. 8, pp. 573–575, 1996. DOI: 10.1364/OL.21.000573.

[66] S. Pitois and G. Millot, "Experimental observation of a new modulational instability spectral window induced by fourth-order dispersion in a normally dispersive single-mode optical fiber", *Optics Communications*, vol. 226, no. 1–6, pp. 415–422, Oct. 2003. DOI: 10.1016/j.optcom.2003.09.001.

[67] G. K. L. Wong, S. G. Murdoch, R. Leonhardt, J. D. Harvey, and V. Marie, "High-conversion-efficiency widely-tunable all-fiber optical parametric oscillator", *Optics Express*, vol. 15, no. 6, pp. 2947–2952, Mar. 2007. DOI: 10.1364/OE.15.002947.

[68] A. Gershikov, E. Shumakher, A. Willinger, and G. Eisenstein, "Fiber parametric oscillator for the 2 μm wavelength range based on narrowband optical parametric amplification", *Optics Letters*, vol. 35, no. 19, pp. 3198–3200, Oct. 2010. DOI: 10.1364/OL.35.003198.

[69] A. Gershikov, J. Lasri, Z. Sacks, and G. Eisenstein, "A tunable fiber parametric oscillator for the 2 μm wavelength range employing an intra-cavity thulium doped fiber active filter", *Optics Communications*, vol. 284, no. 21, pp. 5218–5220, Oct. 2011. DOI: 10.1016/j.optcom.2011.07.043.

[70] K. Inoue, "Four-wave mixing in an optical fiber in the zero-dispersion wavelength region", *Journal of Lightwave Technology*, vol. 10, no. 11, pp. 1553–1561, Nov. 1992. DOI: 10.1109/50.184893.

[71] Y. Emori, S.-I. Matsushita, and S. Namiki, "Cost-effective depolarized diode pump unit designed for C-band flat-gain Raman amplifiers to control EDFA gain profile", in *Optical Fiber Communication Conference (OFC)*, (Mar. 7–10, 2000), vol. 4, Baltimore, MD, USA, 2000, pp. 106–108. DOI: 10.1109/OFC.2000.869430.

[72] S. Namiki and Y. Emori, "Ultrabroad-band Raman amplifiers pumped and gain-equalized by wavelength-division-multiplexed high-power laser diodes", *Journal of Selected Topics in Quantum Electronics*, vol. 7, no. 1, pp. 3–16, 2001. DOI: 10.1109/2944.924003.

[73] H. H. Kee, C. R. S. Fludger, and V. Handerek, "Statistical properties of polarisation dependent gain in fibre Raman amplifiers", in *Optical Fiber Communication Conference and Exhibit (OFC)*, (Mar. 17–22, 2002), Anaheim, CA, USA, 2002, pp. 180–181. DOI: 10.1109/OFC.2002.1036289.

[74] T. Tokura, T. Kogure, T. Sugihara, K. Shimizu, T. Mizuochi, and K. Motoshima, "Pump light depolarization method for low PDG Raman amplification", in *Optical Fiber Communication Conference and Exhibit (OFC)*, (Mar. 17–22, 2002), Anaheim, CA, USA, 2002, pp. 645–646. DOI: 10.1109/OFC.2002.1036620.

[75] E. S. Son, J. H. Lee, and Y. C. Chung, "Exact analysis for statistics of gain in counter-pumped Raman amplifier", in *Optical Fiber Communication Conference (OFC)*, (Feb. 23–27, 2004), vol. 1, Los Angeles, CA, USA, 2004, WJ3.

[76] J. Bromage, "Raman amplification for fiber communications systems", *Journal of Lightwave Technology*, vol. 22, no. 1, pp. 79–93, Jan. 2004. DOI: 10.1109/JLT.2003.822828.

[77] E. S. Son, J. H. Lee, and Y. C. Chung, "Statistics of polarization-dependent gain in fiber Raman amplifiers", *Journal of Lightwave Technology*, vol. 23, no. 3, pp. 1219–1226, Mar. 2005. DOI: 10.1109/JLT.2005.843499.

[78] Z. Li, Z. Li, X. H. Lim, C. Lu, J. Chen, and Y. Wang, "Reduction of polarization-dependent gain due to signal-to-signal Raman interaction in fiber Raman amplifier", *Photonics Technology Letters*, vol. 17, no. 3, pp. 558–560, Mar. 2005. DOI: 10.1109/LPT.2004.842369.

[79] X. Zhou, P. Magill, and M. Birk, "Model for polarization-dependent gain due to pump depletion in a WDM system with forward-pumped Raman amplification", *Journal of Lightwave Technology*, vol. 23, no. 3, pp. 1056–1062, Mar. 2005. DOI: 10.1109/JLT.2004.839990.

[80] T. Tokura, T. Kogure, T. Sugihara, K. Shimizu, T. Mizuochi, and K. Motoshima, "Efficient pump depolarizer analysis for distributed Raman amplifier with low polarization dependence of gain", *Journal of Lightwave Technology*, vol. 24, no. 11, pp. 3889–3896, Nov. 2006. DOI: 10.1109/JLT.2006.883600.

[81] B. Foley, M. L. Dakss, R. W. Davies, and P. Melman, "Gain saturation in fiber Raman amplifiers due to stimulated Brillouin scattering", *Journal of Lightwave Technology*, vol. 7, no. 12, pp. 2024–2032, Dec. 1989. DOI: 10.1109/50.41624.

[82] E. Lichtman, R. G. Waarts, and A. A. Friesem, "Stimulated Brillouin scattering excited by a modulated pump wave in single-mode fibers", *Journal of Lightwave Technology*, vol. 7, no. 1, pp. 171–174, Jan. 1989. DOI: 10.1109/50.17750.

[83] A. R. Chraplyvy, "Limitations on lightwave communications imposed by optical-fiber nonlinearities", *Journal of Lightwave Technology*, vol. 8, no. 10, pp. 1548–1557, Oct. 1990. DOI: 10.1109/50.59195.

[84] A. Kobyakov, M. Sauer, and D. Chowdhury, "Stimulated Brillouin scattering in optical fibers", *Advances in Optics and Photonics*, vol. 2, no. 1, pp. 1–59, Mar. 2010. DOI: 10.1364/AOP.2.000001.

[85] M. O. van Deventer and A. J. Boot, "Polarization properties of stimulated Brillouin scattering in single-mode fibers", *Journal of Lightwave Technology*, vol. 12, no. 4, pp. 585–590, 1994. DOI: 10.1109/50.285349.

[86] C. A. S. de Oliveira, C. K. Jen, A. Shang, and C. Saravanos, "Stimulated brillouin scattering in cascaded fibers of different Brillouin frequency shifts", *Journal of the Optical Society of America B*, vol. 10, no. 6, pp. 969–972, Jun. 1993. DOI: 10.1364/JOSAB.10.000969.

[87] D. Cotter, "Suppression of stimulated Brillouin scattering during transmission of high-power narrowband laser light in monomode fibre", *Electronics Letters*, vol. 18, no. 15, pp. 638–640, Jul. 1982. DOI: 10.1049/el:19820435.

[88] M. Lorenzen, D. Noordegraaf, C. Vandel Nielsen, O. Odgaard, L. Gruner-Nielsen, and K. Rottwitt, "Brillouin suppression in a fiber optical parametric amplifier by combining temperature distribution and phase modulation", in *Conference on Optical Fiber communication/National Fiber Optic Engineers Conference (OFC/NFOEC)*, (Feb. 24–28, 2008), San Diego, CA, USA, 2008, pp. 1–3. DOI: 10.1109/OFC.2008.4528357.

[89] F. H. Tithi and M. S. Islam, "Suppression of stimulated Brillouin scattering effect using nonlinear phase modulation", in *International Conference on Electrical and Computer Engineering (ICECE)*, (Dec. 18–20, 2010), Dhaka, Dec. 2010, pp. 135–138. DOI: 10.1109/ICELCE.2010.5700645.

[90] F. W. Willems, W. Muys, and J. S. Leong, "Simultaneous suppression of stimulated Brillouin scattering and interferometric noise in externally modulated lightwave AM-SCM systems", *Photonics Technology Letters*, vol. 6, no. 12, pp. 1476–1478, Dec. 1994. DOI: 10.1109/68.392206.

[91] M. Nakazawa, "Rayleigh backscattering theory for single-mode optical fibers", *Journal of the Optical Society of America*, vol. 73, no. 9, pp. 1175–1180, Sep. 1983. DOI: 10.1364/JOSA.73.001175.

[92] O. Okusaga, J. P. Cahill, A. Docherty, C. R. Menyuk, and W. Zhou, "Spontaneous inelastic Rayleigh scattering in optical fibers", *Optics Letters*, vol. 38, no. 4, pp. 549–551, Feb. 2013. DOI: 10.1364/OL.38.000549.

[93] Y. Takushima and T. Okoshi, "Suppression of stimulated Brillouin scattering using optical isolators", *Electronics Letters*, vol. 28, no. 12, pp. 1155–1157, 1992. DOI: 10.1049/el:19920729.

[94] K. Shiraki, M. Ohashi, and M. Tateda, "SBS threshold of a fiber with a Brillouin frequency shift distribution", *Journal of Lightwave Technology*, vol. 14, no. 1, pp. 50–57, Jan. 1996. DOI: 10.1109/50.476136.

[95] F. Poletti, K. Furusawa, Z. Yusoff, N. G. R. Broderick, and D. J. Richardson, "Nonlinear tapered holey fibers with high stimulated Brillouin scattering threshold and controlled dispersion", *Journal of the Optical Society of America B*, vol. 24, no. 9, pp. 2185–2194, Sep. 2007. DOI: 10.1364/JOSAB.24.002185.

[96] K. Shiraki, M. Ohashi, and M. Tateda, "Suppression of stimulated Brillouin scattering in a fibre by changing the core radius", *Electronics Letters*, vol. 31, no. 8, pp. 668–669, Apr. 1995. DOI: 10.1049/el:19950418.

[97] A. Liu, "Suppressing stimulated Brillouin scattering infiber amplifiers using nonuniform fiber andtemperature gradient", *Optics Express*, vol. 15, no. 3, pp. 977–984, Feb. 2007. DOI: 10.1364/OE.15.000977.

[98] M. D. Mermelstein, "SBS threshold measurements and acoustic beam propagation modeling in guiding and anti-guiding single mode optical fibers", *Optics Express*, vol. 17, no. 18, pp. 16 225–16 237, Aug. 2009. DOI: 10.1364/OE.17.016225.

[99] M.-J. Li, X. Chen, J. Wang, S. Gray, A. Liu, J. A. Demeritt, A. B. Ruffin, A. M. Crowley, D. T. Walton, and L. A. Zenteno, "Al/Ge co-doped large mode area fiber with high SBS threshold", *Optics Express*, vol. 15, no. 13, pp. 8290–8299, Jun. 2007. DOI: 10.1364/OE.15.008290.

[100] L. Gruner-Nielsen, S. Dasgupta, M. D. Mermelstein, D. Jakobsen, S. Herstrøm, M. E. V. Pedersen, E. L. Lim, S. Alam, F. Parmigiani, D. Richardson, and B. Palsdottir, "A silica based highly nonlinear fibre with improved threshold for stimulated Bbrillouin scattering", in *36th European Conference and Exhibition on Optical Communication (ECOC)*, (Sep. 19–23, 2010), Torino, Italy, 2010, pp. 1–3. DOI: 10.1109/ECOC.2010.5621232.

[101] Y. Koyamada, S. Sato, S. Nakamura, H. Sotobayashi, and W. Chujo, "Simulating and designing Brillouin gain spectrum in single-mode fibers", *Journal of Lightwave Technology*, vol. 22, no. 2, pp. 631–639, Feb. 2004. DOI: 10.1109/JLT.2003.822007.

[102] Y. Imai and N. Shimada, "Dependence of stimulated Brillouin scattering on temperature distribution in polarization-maintaining fibers", *Photonics Technology Letters*, vol. 5, no. 11, pp. 1335–1337, Nov. 1993. DOI: 10.1109/68.250061.

[103] J. Hansryd, F. Dross, M. Westlund, P. A. Andrekson, and S. N. Knudsen, "Increase of the SBS threshold in a short highly nonlinear fiber by applying a temperature distribution", *Journal of Lightwave Technology*, vol. 19, no. 11, pp. 1691–1697, Nov. 2001. DOI: 10.1109/50.964069.

[104] L. Gruner-Nielsen, S. Herstrøm, S. Dasgupta, D. Richardson, D. Jakobsen, C. Lundström, P. A. Andrekson, M. E. V. Pedersen, and B. Palsdottir, "Silica-based highly nonlinear fibers with a high SBS threshold", in *IEEE Winter Topicals (WTM)*, (Jan. 10–12, 2011), Keystone, CO, USA, 2011, pp. 171–172. DOI: 10.1109/PHOTWTM.2011.5730102.

[105] T. Kurashima, T. Horiguchi, and M. Tateda, "Thermal effects of Brillouin gain spectra in single-mode fibers", *Photonics Technology Letters*, vol. 2, no. 10, pp. 718–720, Oct. 1990. DOI: 10.1109/68.60770.

[106] J. M. C. Boggio, J. D. Marconi, and H. L. Fragnito, "Experimental and numerical investigation of the SBS-threshold increase in an optical fiber by applying strain distributions", *Journal of Lightwave Technology*, vol. 23, no. 11, pp. 3808–3814, Nov. 2005. DOI: 10.1109/JLT.2005.856226.

[107] W. Zou, Z. He, A. D. Yablon, and K. Hotate, "Dependence of Brillouin frequency shift in optical fibers on draw-induced residual elastic and inelastic strains", *Photonics Technology Letters*, vol. 19, no. 18, pp. 1389–1391, Sep. 2007. DOI: 10.1109/LPT.2007.903341.

[108] R. H. Stolen, C. Lin, and R. K. Jain, "A time-dispersion-tuned fiber Raman oscillator", *Applied Physics Letters*, vol. 30, no. 7, pp. 340–342, Apr. 1977. DOI: 10.1063/1.89391.

[109] K. Tamura and M. Nakazawa, "Dispersion-tuned harmonically mode-locked fiber ring laser for self-synchronization to an external clock", *Optics Letters*, vol. 21, no. 24, pp. 1984–1986, Dec. 1996. DOI: 10.1364/OL.21.001984.

[110] S. Li and K. T. Chan, "Electrical wavelength tunable and multiwavelength actively mode-locked fiber ring laser", *Applied Physics Letters*, vol. 72, no. 16, pp. 1954–1956, Apr. 1998. DOI: 10.1063/1.121263.

[111] K. Chan and C. Shu, "Compensated dispersion tuning in harmonically mode-locked fiber laser", *Applied Physics Letters*, vol. 75, no. 7, pp. 891–893, Aug. 1999. DOI: 10.1063/1.124545.

[112] S. Yamashita and M. Asano, "Wide and fast wavelength-tunable mode-locked fiber laser based on dispersion tuning", *Optics Express*, vol. 14, no. 20, pp. 9299–9306, Oct. 2006. DOI: 10.1364/OE.14.009299.

[113] Y. Zhou, K. K. Y. Cheung, Q. Li, S. Yang, P. C. Chui, and K. K.-Y. Wong, "Fast and wide tuning wavelength-swept source based on dispersion-tuned fiber optical parametric oscillator", *Optics Letters*, vol. 35, no. 14, pp. 2427–2429, Jul. 2010. DOI: 10.1364/OL.35.002427.

[114] S. Yang, K. K. Y. Cheung, Y. Zhou, and K. K.-Y. Wong, "Dispersion-tuned harmonically mode-locked fiber-optical parametric oscillator", *Photonics Technology Letters*, vol. 22, no. 8, pp. 580–582, Apr. 2010. DOI: 10.1109/LPT.2010.2043091.

[115] H. Takesue and T. Horiguchi, "Chromatic dispersion measurement of optical components using lightwave synthesized frequency sweeper", *Journal of Lightwave Technology*, vol. 20, no. 4, pp. 625–633, Apr. 2002. DOI: 10.1109/50.996582.

[116] B. Desthieux, R. I. Laming, and D. N. Payne, "111 kW (0.5 mJ) pulse amplification at 1.5 μm using a gated cascade of three erbium-doped fiber amplifiers", *Applied Physics Letters*, vol. 63, no. 5, pp. 586–588, Aug. 1993. DOI: 10.1063/1.109957.

[117] J. Nilsson and B. Jaskorzynska, "Modeling and optimization of low-repetition-rate high-energy pulse amplification in cw-pumped erbium-doped fiber amplifiers", *Optics Letters*, vol. 18, no. 24, pp. 2099–2101, Dec. 1993. DOI: 10.1364/OL.18.002099.

[118] D. Dahan and G. Eisenstein, "Tunable all optical delay via slow and fast light propagation in a Raman assisted fiber optical parametric amplifier: a route to all optical buffering", *Optics Express*, vol. 13, no. 16, pp. 6234–6249, Aug. 2005. DOI: 10.1364/OPEX.13.006234.

[119] A. S. Y. Hsieh, G. K. L. Wong, S. G. Murdoch, S. Coen, F. Vanholsbeeck, R. Leonhardt, and J. D. Harvey, "Combined effect of Raman and parametric gain on single-pump parametric amplifiers", *Optics Express*, vol. 15, no. 13, pp. 8104–8114, Jun. 2007. DOI: 10.1364/OE.15.008104.

[120] A. Willinger, E. Shumakher, and G. Eisenstein, "On the roles of polarization and Raman-assisted phase matching in narrowband fiber parametric amplifiers", *Journal of Lightwave Technology*, vol. 26, no. 14, pp. 2260–2268, Jul. 2008. DOI: 10.1109/JLT.2008.923273.

[121] J. Ye and S. T. Cundiff, Eds., *Femtosecond Optical Frequency Comb: Principle, Operation and Applications*. Springer, 2005.

[122] S. A. Diddams, "The evolving optical frequency comb [invited]", *Journal of the Optical Society of America B*, vol. 27, no. 11, B51–B62, Nov. 2010. DOI: 10.1364/JOSAB.27.000B51.

[123] T. Udem, R. Holzwarth, and T. W. Hänsch, "Optical frequency metrology", *Nature*, vol. 416, no. 6877, pp. 233–237, Mar. 2002. DOI: 10.1038/416233a.

[124] M. Kuntz, G. Fiol, M. Lämmlin, D. Bimberg, M. G. Thompson, K. T. Tan, C. Marinelli, R. V. Penty, I. H. White, V. M. Ustinov, A. E. Zhukov, Y. M. Shernyakov, and A. R. Kovsh, "35 GHz mode-locking of 1.3 μm quantum dot lasers", *Applied Physics Letters*, vol. 85, no. 5, pp. 843–845, Aug. 2004. DOI: 10.1063/1.1776340.

[125] E. U. Rafailov, M. A. Cataluna, and W. Sibbett, "Mode-locked quantum-dot lasers", *Nature Photonics*, vol. 1, no. 7, pp. 395–401, Jul. 2007. DOI: 10.1038/nphoton.2007.120.

[126] A. A. Savchenkov, A. B. Matsko, W. Liang, V. S. Ilchenko, D. Seidel, and L. Maleki, "Kerr combs with selectable central frequency", *Nature Photonics*, vol. 5, no. 5, pp. 293–296, May 2011. DOI: 10.1038/nphoton.2011.50.

[127] T. J. Kippenberg, S. M. Spillane, and K. J. Vahala, "Kerr-nonlinearity optical parametric oscillation in an ultrahigh-Q toroid microcavity", *Physical Review Letters*, vol. 93, no. 8, p. 083 904, Aug. 2004. DOI: 10.1103/PhysRevLett.93.083904.

[128] P. Del'Haye, A. Schliesser, O. Arcizet, T. Wilken, R. Holzwarth, and T. J. Kippenberg, "Optical frequency comb generation from a monolithic microresonator", *Nature*, vol. 450, no. 7173, pp. 1214–1217, Dec. 2007. DOI: 10.1038/nature06401.

[129] I. H. Agha, Y. Okawachi, M. A. Foster, J. E. Sharping, and A. L. Gaeta, "Four-wave-mixing parametric oscillations in dispersion-compensated high-Q silica microspheres", *Physical Review A*, vol. 76, no. 4, p. 043 837, Oct. 2007. DOI: 10.1103/PhysRevA.76.043837.

[130] A. C. Turner, M. A. Foster, A. L. Gaeta, and M. Lipson, "Ultra-low power parametric frequency conversion in a silicon microring resonator", *Optics Express*, vol. 16, no. 7, pp. 4881–4887, Mar. 2008. DOI: 10.1364/OE.16.004881.

[131] J. S. Levy, A. Gondarenko, M. A. Foster, A. C. Turner-Foster, A. L. Gaeta, and M. Lipson, "CMOS-compatible multiple-wavelength oscillator for on-chip optical interconnects", *Nature Photonics*, vol. 4, no. 1, pp. 37–40, Jan. 2010. DOI: 10.1038/nphoton.2009.259.

[132] J. S. Levy, K. Saha, Y. Okawachi, M. A. Foster, A. L. Gaeta, and M. Lipson, "High-performance silicon-nitride-based multiple-wavelength source", *Photonics Technology Letters*, vol. 24, no. 16, pp. 1375–1377, 2012. DOI: 10.1109/LPT.2012.2204245.

[133] C. J. McKinstrie and M. G. Raymer, "Four-wave-mixing cascades near the zero-dispersion frequency", *Optics Express*, vol. 14, no. 21, pp. 9600–9610, Oct. 2006. DOI: 10.1364/OE.14.009600.

[134] A. Varanavičius, A. Dubietis, A. Beržanskis, R. Danielius, and A. Piskarskas, "Near-degenerate cascaded four-wave mixing in an optical parametric amplifier", *Optics Letters*, vol. 22, no. 21, pp. 1603–1605, Nov. 1997. DOI: 10.1364/OL.22.001603.

[135] R. Tang, J. Lasri, P. S. Devgan, V. Grigoryan, P. Kumar, and M. Vasilyev, "Gain characteristics of a frequency nondegenerate phase-sensitive fiber-optic parametric amplifier with phase self-stabilized input", *Optics Express*, vol. 13, no. 26, pp. 10 483–10 493, Dec. 2005. DOI: 10.1364/OPEX.13.010483.

[136] A. Gershikov and G. Eisenstein, "Narrowband phase sensitive fiber parametric amplifier", *Optics Letters*, vol. 37, no. 15, pp. 3204–3206, Aug. 2012. DOI: 10.1364/OL.37.003204.

[137] L.-S. Ma, P. Jungner, J. Ye, and J. L. Hall, "Delivering the same optical frequency at two places: accurate cancellation of phase noise introduced by an optical fiber or other time-varying path", *Optics Letters*, vol. 19, no. 21, pp. 1777–1779, Nov. 1994. DOI: 10.1364/OL.19.001777.

[138] D. Braje, L. Hollberg, and S. Diddams, "Brillouin-enhanced hyperparametric generation of an optical frequency comb in a monolithic highly nonlinear fiber cavity pumped by a CW laser", *Physical Review Letters*, vol. 102, no. 19, p. 193 902, May 2009. DOI: 10.1103/PhysRevLett.102.193902.

[139] J. Li, X. Xiao, L. Kong, and C. Yang, "Enhancement of cascaded four-wave mixing via optical feedback", *Optics Express*, vol. 20, no. 20, pp. 21 940–21 945, Sep. 2012. DOI: 10.1364/OE.20.021940.

[140] R. Noé, H. Heidrich, and D. Hoffmann, "Endless polarization control systems for coherent optics", *Journal of Lightwave Technology*, vol. 6, no. 7, pp. 1199–1208, 1988. DOI: 10.1109/50.4117.

[141] N. G. Walker and G. R. Walker, "Polarization control for coherent communications", *Journal of Lightwave Technology*, vol. 8, no. 3, pp. 438–458, 1990. DOI: 10.1109/50.50740.

[142] R. Noé, D. Sandel, and V. Mirvoda, "PMD in high-bit-rate transmission and means for its mitigation", *Journal of Selected Topics in Quantum Electronics*, vol. 10, no. 2, pp. 341–355, 2004. DOI: 10.1109/JSTQE.2004.827842.

[143] P. Oswald and C. K. Madsen, "Deterministic analysis of endless tuning of polarization controllers", *Journal of Lightwave Technology*, vol. 24, no. 7, pp. 2932–2939, Jul. 2006. DOI: 10.1109/JLT.2006.872688.

[144] A. Hidayat, B. Koch, H. Zhang, V. Mirvoda, M. Lichtinger, D. Sandel, and R. Noé, "High-speed endless optical polarization stabilization using calibrated waveplates and field-programmable gate array-based digital controller", *Optics Express*, vol. 16, no. 23, pp. 18 984–18 991, Nov. 2008. DOI: 10.1364/OE.16.018984.

[145] M. Martinelli, P. Martelli, and S. M. Pietralunga, "Polarization stabilization in optical communications systems", *Journal of Lightwave Technology*, vol. 24, no. 11, pp. 4172–4183, Nov. 2006. DOI: 10.1109/JLT.2006.884228.

[146] B. Koch, A. Hidayat, H. Zhang, V. Mirvoda, M. Lichtinger, D. Sandel, and R. Noe, "Optical endless polarization stabilization at 9 krad/s with FPGA-based controller", *Photonics Technology Letters*, vol. 20, no. 12, pp. 961–963, 2008. DOI: 10.1109/LPT.2008.922910.

[147] V. V. Kozlov, J. Nuño, J. D. Ania-Castañón, and S. Wabnitz, "Analytic theory of fiber-optic Raman polarizers", *Optics Express*, vol. 20, no. 24, pp. 27 242–27 247, Nov. 2012. DOI: 10.1364/OE.20.027242.

[148] C. R. S. Fludger, V. Handerek, and R. J. Mears, "Pump to signal RIN transfer in Raman fiber amplifiers", *Journal of Lightwave Technology*, vol. 19, no. 8, pp. 1140–1148, Aug. 2001. DOI: 10.1109/50.939794.

[149] Q. Lin and G. P. Agrawal, "Vector theory of stimulated Raman scattering and its application to fiber-based Raman amplifiers", *Journal of the Optical Society of America B*, vol. 20, no. 8, pp. 1616–1631, 2003. DOI: 10.1364/JOSAB.20.001616.

[150] R. Hellwarth, J. Cherlow, and T.-T. Yang, "Origin and frequency dependence of nonlinear optical susceptibilities of glasses", *Physical Review B*, vol. 11, no. 2, pp. 964–967, Jan. 1975. DOI: 10.1103/PhysRevB.11.964.

[151] I. Mandelbaum, M. Bolshtyansky, T. F. Heinz, and A. R. H. Walker, "Method for measuring the Raman gain tensor in optical fibers", *Journal of the Optical Society of America B*, vol. 23, no. 4, pp. 621–627, Apr. 2006. DOI: 10.1364/JOSAB.23.000621.

[152] S. Kumar, A. Selvarajan, and G. V. Anand, "Influence of Raman scattering on the cross phase modulation in optical fibers", *Optics Communications*, vol. 102, no. 3–4, pp. 329–335, Oct. 1993. DOI: 10.1016/0030-4018(93)90405-T.

[153] A. Höök, "Influence of stimulated Raman scattering on cross-phase modulation between waves in optical fibers", *Optics Letters*, vol. 17, no. 2, pp. 115–117, Jan. 1992. DOI: 10.1364/OL.17.000115.

[154] Q. Lin and G. P. Agrawal, "Polarization mode dispersion-induced fluctuations during Raman amplifications in optical fibers", *Optics Letters*, vol. 27, no. 24, pp. 2194–2196, Dec. 2002. DOI: 10.1364/OL.27.002194.

[155] ——, "Statistics of polarization-dependent gain in fiber-based Raman amplifiers", *Optics Letters*, vol. 28, no. 4, pp. 227–229, Feb. 2003. DOI: 10.1364/OL.28.000227.

[156] R. H. Stolen, J. P. Gordon, W. J. Tomlinson, and H. A. Haus, "Raman response function of silica-core fibers", *Journal of the Optical Society of America B*, vol. 6, no. 6, pp. 1159–1166, Jun. 1989. DOI: 10.1364/JOSAB.6.001159.

[157] A. Galtarossa and L. Palmieri, "Reflectometric measurements of polarization properties in optical-fiber links", *Journal of Optical and Fiber Communications Reports*, vol. 1, no. 2, pp. 150–179, Oct. 2004. DOI: 10.1007/s10297-004-0012-2.

[158] A. Galtarossa, L. Palmieri, M. Schiano, and T. Tambosso, "Measurement of birefringence correlation length in long, single-mode fibers", *Optics Letters*, vol. 26, no. 13, pp. 962–964, Jul. 2001. DOI: 10.1364/OL.26.000962.

[159] ——, "Statistical characterization of fiber random birefringence", *Optics Letters*, vol. 25, no. 18, pp. 1322–1324, Sep. 2000. DOI: 10.1364/OL.25.001322.

[160] P. K. A. Wai and C. R. Menyuk, "Polarization mode dispersion, decorrelation, and diffusion in optical fibers with randomly varying birefringence", *Journal of Lightwave Technology*, vol. 14, no. 2, pp. 148–157, Feb. 1996. DOI: 10.1109/50.482256.

[161] P. K. A. Wai, W. L. Kath, C. R. Menyuk, and J. W. Zhang, "Nonlinear polarization-mode dispersion in optical fibers with randomly varying birefringence", *Journal of the Optical Society of America B*, vol. 14, no. 11, pp. 2967–2979, Nov. 1997. DOI: 10.1364/JOSAB.14.002967.

[162] W. H. Press, S. A. Teukolsky, W. T. Vetterling, and B. P. Flannery, *Numerical Recipes 3rd Edition: The Art of Scientific Computing*, 3rd ed. Cambridge University Press, Sep. 2007.

[163] R. H. Stolen, "Polarization effects in fiber Raman and Brillouin lasers", *Journal of Quantum Electronics*, vol. 15, no. 10, pp. 1157–1160, 1979. DOI: 10.1109/JQE.1979.1069913.

[164] M. Santagiustina, "Exact integral solution of saturation and depletion in forward and backward optical fiber Raman amplifiers", *Optics Letters*, vol. 32, no. 20, pp. 3023–3025, Oct. 2007. DOI: 10.1364/OL.32.003023.

[165] S. R. Chinn, "Analysis of counter-pumped small-signal fibre Raman amplifiers", *Electronics Letters*, vol. 33, no. 7, pp. 607–608, Mar. 1997. DOI: 10.1049/el:19970428.

[166] J. AuYeung and A. Yariv, "Spontaneous and stimulated Raman scattering in long low loss fibers", *Journal of Quantum Electronics*, vol. 14, no. 5, pp. 347–352, 1978. DOI: 10.1109/JQE.1978.1069797.

[167] H. G. Berry, G. Gabrielse, and A. E. Livingston, "Measurement of the Stokes parameters of light", *Applied Optics*, vol. 16, no. 12, pp. 3200–3205, Dec. 1977. DOI: 10.1364/AO.16.003200.

[168] J. N. Damask, *Polarization Optics in Telecommunications*, W. T. Rhodes, Ed., ser. Springer Series in Optical Sciences. Springer, 2005, vol. 101. DOI: 10.1007/b137386.

[169] E. Collett, *Field Guide to Polarization*, J. E. Greivenkamp, Ed., ser. SPIE Field Guides. SPIE, 2005, vol. FG05. DOI: 10.1117/3.626141.

[170] R. C. Jones, "A new calculus for the treatment of optical systems I: description and discussion of the calculus", *Journal of the Optical Society of America*, vol. 31, no. 7, pp. 488–493, Jul. 1941. DOI: 10.1364/JOSA.31.000488.

[171] G. G. Stokes, "On the composition and resolution of streams of polarized light from different sources", *Transactions of the Cambridge Philosophical Society*, vol. 9, pp. 399–416, 1852.

[172] J. P. Gordon and H. Kogelnik, "PMD fundamentals: polarization mode dispersion in optical fibers", *Proceedings of the National Academy of Sciences of the United States of America*, vol. 97, no. 9, pp. 4541–4550, Apr. 2000. DOI: 10.1073/pnas.97.9.4541.

[173] J. W. E. M. von Pauli, "Zur Quantenmechanik des magnetischen Elektrons", *Zeitschrift für Physik*, vol. 43, no. 9–10, pp. 601–623, Sep. 1927. DOI: 10.1007/BF01397326.

[174] C. Flueraru, S. Latoui, J. Besse, and P. Legendre, "Error analysis of a rotating quarter-wave plate Stokes' polarimeter", *Transactions on Instrumentation and Measurement*, vol. 57, no. 4, pp. 731–735, Apr. 2008. DOI: 10.1109/TIM.2007.913752.

[175] B. Schaefer, E. Collett, R. Smyth, D. Barrett, and B. Fraher, "Measuring the Stokes polarization parameters", *American Journal of Physics*, vol. 75, no. 2, p. 163, 2007. DOI: 10.1119/1.2386162.

[176] L. Giudicotti and M. Brombin, "Data analysis for a rotating quarter-wave, far-infrared Stokes polarimeter", *Applied Optics*, vol. 46, no. 14, pp. 2638–2648, May 2007. DOI: 10.1364/AO.46.002638.

[177] M. J. Walker, "Matrix calculus and the Stokes parameters of polarized radiation", *American Journal of Physics*, vol. 22, no. 4, pp. 170–174, 1954. DOI: 10.1119/1.1933670.

[178] P. J. Leo, G. R. Gray, G. J. Simer, and K. B. Rochford, "State of polarization changes: classification and measurement", *Journal of Lightwave Technology*, vol. 21, no. 10, pp. 2189–2193, 2003. DOI: 10.1109/JLT.2003.816813.

[179] W. H. J. Aarts and G.-D. Khoe, "New endless polarization control method using three fiber squeezers", *Journal of Lightwave Technology*, vol. 7, no. 7, pp. 1033–1043, 1989. DOI: 10.1109/50.29630.

[180] G. Marsaglia, "Choosing a point from the surface of a sphere", *The Annals of Mathematical Statistics*, vol. 43, no. 2, pp. 645–646, Apr. 1972. DOI: 10.1214/aoms/1177692644.

[181] M. E. Muller, "A note on a method for generating points uniformly on n-dimensional spheres", *Communications of the ACM*, vol. 2, no. 4, pp. 19–20, Apr. 1959. DOI: 10.1145/377939.377946.

[182] ——, "Some continuous Monte Carlo methods for the Dirichlet problem", *The Annals of Mathematical Statistics*, vol. 27, no. 3, pp. 569–589, Sep. 1956. DOI: 10.1214/aoms/1177728169.

[183] L. Yao, H. Huang, J. Chen, E. Tan, and A. Willner, "A novel scheme for achieving quasi-uniform rate polarization scrambling at 752 krad/s", *Optics Express*, vol. 20, no. 2, pp. 1691–1699, Jan. 2012. DOI: 10.1364/OE.20.001691.

[184] B. Koch, R. Noé, V. Mirvoda, and D. Sandel, "100 krad/s endless polarisation tracking with miniaturised module card", *Electronics Letters*, vol. 47, no. 14, pp. 813–814, 2011. DOI: 10.1049/el.2011.1522.

[185] C. R. Menyuk, D. Wang, and A. N. Pilipetskii, "Repolarization of polarization-scrambled optical signals due to polarization dependent loss", *Photonics Technology Letters*, vol. 9, no. 9, pp. 1247–1249, 1997. DOI: 10.1109/68.618493.

[186] I. Kaminow, "Polarization in optical fibers", *Journal of Quantum Electronics*, vol. 17, no. 1, pp. 15–22, Jan. 1981. DOI: 10.1109/JQE.1981.1070626.

[187] J. P. Gordon, "Statistical properties of polarization mode dispersion", *Journal of Optical and Fiber Communications Reports*, vol. 1, no. 3, pp. 210–217, Nov. 2004. DOI: 10.1007/s10297-004-0003-3.

[188] M. Karlsson and H. Sunnerud, "PMD impact on optical systems: single- and multichannel effects", *Journal of Optical and Fiber Communications Reports*, vol. 1, no. 2, pp. 123–140, Oct. 2004. DOI: 10.1007/s10297-004-0013-1.

[189] R. Ulrich and A. Simon, "Polarization optics of twisted single-mode fibers", *Applied Optics*, vol. 18, no. 13, pp. 2241–2251, Jul. 1979. DOI: 10.1364/AO.18.002241.

[190] A. Papoulis and S. U. Pillai, *Probability, Random Variables, and Stochastic Processes*, 4th ed. McGraw-Hill, 2002.

[191] P. K. A. Wai and C. R. Menyuk, "Polarization decorrelation in optical fibers with randomly varying birefringence", *Optics Letters*, vol. 19, no. 19, pp. 1517–1519, Oct. 1994. DOI: 10.1364/OL.19.001517.

[192] A. Galtarossa, L. Palmieri, M. Schiano, and T. Tambosso, "Measurements of beat length and perturbation length in long single-mode fibers", *Optics Letters*, vol. 25, no. 6, pp. 384–386, Mar. 2000. DOI: 10.1364/OL.25.000384.

[193] J. Stoer and R. Bulirsch, *Introduction to Numerical Analysis*. Springer, 1992.

[194] U. M. Ascher, R. M. M. Mattheij, and R. D. Russell, *Numerical Solution of Boundary Value Problems for Ordinary Differential Equations*. SIAM, 1995.

[195] M. Abramowitz and I. A. Stegun, *Handbook of Mathematical Functions: With Formulas, Graphs, and Mathematical Tables*. Dover Publications, 1964.

[196] J. C. Butcher, *Numerical methods for ordinary differential equations*, 2nd ed. John Wiley & Sons, 2008.